

**High Resolution Fibre Fed Echelle Spectrograph:
Calibration and Characterisation For Precise Radial
Velocities And Chemical Abundances**

A Thesis

Submitted for the Degree of
Doctor of Philosophy (Technology)

Submitted by

Anantha Ch

Department of Applied Optics & Photonics

University College of Technology

University of Calcutta

August 2015

DECLARATION

I hereby declare that the work incorporated in the present thesis entitled “High Resolution Fibre Fed Echelle Spectrograph: Calibration and Characterisation For Precise Radial Velocities And Chemical Abundances” is my own work and is original. I further declare that this thesis has not been submitted for the award of any degree, diploma, associateship, fellowship etc. in any university or institute.

Date:

Anantha Ch

(Author)

Indian Institute of Astrophysics

2nd Block, Koramangala

Bangalore-560034

Abstract

Modern astronomical spectrographs have been in use for several hundred years now, contributing to the study of the physical, chemical and kinematical properties of stars and other celestial bodies. In the recent years, there has been new development in the design choices, calibration sources and detectors for spectrograph that led to large improvements in resolution, efficiency and stability, which have been a key to the discoveries of low mass exoplanets, cosmic dynamics and variability of physical constants. Even with these major improvements in the instrumentation, a little has changed in the way data is calibrated. The physics used in the designing and building of the instrument is seldom put to use for instrument calibrations.

In the current work, we have developed a computing scheme whereby an astronomical spectrograph can be modelled and controlled without recourse to a ray-tracing program. This is achieved by using paraxial ray tracing, exact corrections for certain surface types and the aberration coefficients of Buchdahl for more complex modules. We have shown that the resultant chain of paraxial ray trace matrices and correction matrices can predict the location of any spectral line on the detector under all normal operating conditions with a high degree of certainty. This kind of model will allow a semi-autonomous control via simple in-house, program modules. The theory and formulation in developing a model for HESP (Hanle Echelle Spectrograph), comparison with commercial ray tracing software and validation the model with calibration exposures taken in the lab are described in detail. We have demonstrated that the wavelength calibration using the dispersion solution from model performs superior to the empirical solution that is used in standard spectroscopic reduction software (e.g. IRAF), especially in the regime of sparse and low signal calibration lines. We also discuss the potential use of model in simultaneous calibration using double fiber in tracking the instrument drifts and issues related to positional and wavelength dependency of instrumental drift. We conclude by listing several science areas that would benefit using a model based calibration. Apart from calibration of science data, the model along with an optimization routine can be used in the instrument mainte-

nance pipeline to study the real time behaviour of the instrument, trending and long-term stability. We also present the work related to the development of autoguiding algorithm and fiber scrambling for HESP and implication to radial velocity shift.

Contents

List of Figures	vii
List of Tables	xvii
1 Introduction	1
1.1 Historic overview of spectrograph design	2
1.2 Historic perspective of precision radial velocities	3
1.3 Accurate chemical abundances	7
1.4 physical model based calibrations	9
2 Hanle Echelle Spectrograph	13
2.1 Introduction	13
2.2 Cassegrain Unit	19
2.3 Calibration Unit	22
2.4 Optical Fibers	23
2.5 Acquisition and Guiding Unit	24
2.6 Spectrograph Unit	24
2.6.1 Image Slicer	24
2.6.2 Spectrograph	26
3 Model Based Calibration	29
3.1 Introduction	29

3.2	Coordinate system and Ray coordinates	31
3.3	Class Definitions	32
3.3.1	Slit	32
3.3.2	Collimator	33
3.3.3	Grating	34
3.3.4	Prism	36
3.3.5	Camera	38
3.3.5.1	ABCD Matrices: Paraxial Coefficients of Lens systems	39
3.3.5.2	Aberration Polynomials	42
3.3.5.3	Calculating Aberration Coefficients of a rota- tionally symmetric system	47
3.3.5.4	HESP Camera Implementation:	51
3.3.5.5	Wavelength Dependency of Coefficients	54
3.3.6	Detector	55
3.4	Total System Description	55
4	Matching model with the Instrument	58
4.1	Introduction	58
4.2	Choice of model parameters for optimization	60
4.3	Wave length features Selection and centroid determination of features	62
4.4	Optimisation routine	68
4.5	Glass Refractive indices	71
5	Results	78
5.1	Accuracy of the analytical model	79
5.1.1	Preliminary data and Optimization of the model	79
5.1.2	Weighted RMS Merit Function	83
5.1.3	Dispersion Solutions	89
5.2	Noise precision of model predictions	90

5.3	Parameters	92
5.4	Double fiber	95
6	Autoguided, Atmospheric dispersion corrector and Optical fibers for HESP	98
6.1	Introduction	98
6.2	Autoguided for HESP	99
6.2.1	Aperture photometry	101
6.2.2	Simulations	105
6.2.2.1	Seeing - 1.1": Exp.Time - 5sec	108
6.2.2.2	Seeing- 1.5": Exp.Time- 2sec	110
6.3	Atmospheric Dispersion Correctors	112
6.4	Optical Fiber Scrambling	116
7	Conclusion and Future Work	120

List of Figures

1.1	A cartoon depiction of an observation procedure and perception of the Universe. (By Rosa M)	5
2.1	Optical layout of cassegrain unit. (Figure credit: Callaghan Innovation)	19
2.2	Operating Modes of Cassegrain Unit, (Figure Credit: Callaghan Innovation)	21
2.3	Calibration Unit top view (Image Credit: Callaghan Innovation)	22
2.4	Quartz lamp mount and optics, (Image Credit: Callaghan Innovation)	23
2.5	Slit optics and Spectrograph optical layout (Image credit: Callaghan Innovation)	25
2.6	Left: Image slicer rendering showing the working of the slicer. Right: Schematic of the fibre slicing. The full diameter of a 2.85” fibre is shown being sliced into two 1.2” slices. (Image Credit: Callaghan innovation)	26
2.7	Spectral format of the designed HESP, Image Credit: Callaghan innovation	27

2.8	Spot diagram of slit image for sliced and unsliced modes on CCD at the central wavelength for three different positions of slit mirror. Right: at the focus, Centre and left: slit mirror moved 1mm away from focus in the two directions respectively	28
2.9	Hanle Echelle Spectrograph aligned and tested at the Kiwistar Optics Facility (Image credit : Callaghan Innovation)	28
3.1	Class diagram of prism	32
3.2	Coordinate system Definition	32
3.3	Two dimensional depiction of the collimator mirror	34
3.4	Prism description. The ray coordinates on surface AB are the input to the prism transformation function. The output of the function are the ray coordinates on CD	37
3.5	Refraction at a spherical surface	40
3.6	Illustration of transfer equations between two surfaces	40
3.7	Paraxial representation of an axially symmetric Optical system	43
3.8	Aberration terms illustrated	44
3.9	Rotational Invariance of a rotationally symmetric optical system [20]	45
3.10	Camera configuration with object plane at the camera system's entrance pupil in the spectrograph (b) Camera configuration with object plane at infinity	52
3.11	Difference in aberration terms. Left: Vector plot of differences at different points on the spectrum for one of the sets of thickness and radii. Right: top panel is the difference in aberration terms' x-coordinate, while the bottom panel is the difference in aberration terms' y-coordinate in pixel units of the points in spectrum shown in left panel for different sets of thicknesses and radii.	53
3.12	Variation of the ABCD coefficients with wavelength	54

3.13	Spread sheet description of the instrument	57
4.1	Flowchart of the model based technique (Bristow 2008).	59
4.2	Shift in spectrum for different parameter values. Two different parameter subsets were changed a little from the nominal. The blue points show the scatter of selected wavelengths across the spectrum. Red arrows indicate the shift in these positions from the nominal when the parameter subsets are changed.	61
4.3	Left: Vector plot of difference of feature position from instrument and model predictions. Centre & Right: Vector plots of difference of feature positions from instrument and optimized model predictions (model optimized for two different subsets of parameters). The residual patterns are an indication of missing parameters used for optimization. The pattern itself is an indication of what parameters may be missing.	62
4.4	Numerical simulation results showing the shift in Centroid fitted for blends for different separations and intensity ratios	67
4.5	Difference in the refractive index for two optimizations described in text	75
4.6	Depiction of shift in spectrum from calculated positions due to mismatch in prism glass refractive indices data. Left: Vector plot showing the pattern in shift, Right: Shift in cross and high dispersion coordinates with respect to cross dispersion coordinate of the wavelengths positions on the CCD	76
4.7	Depiction of shift in spectrum from calculated positions due to mismatch in camera glasses refractive indices data. Left: Vector plot showing the pattern in shift, Right: Shift in cross and high dispersion coordinates with respect to cross dispersion coordinate of the wavelengths positions on the CCD for multiple cases	76

4.8	Residuals in the wave lengths positions on the CCD after optimization of the model for two cases. +: when the glass data of the model and instrument matched, o: glass data between model and instrument differ	77
5.1	Plots showing the difference between Zemax trace and model for various aberration terms included. First column is the difference in x-coordinate, second column is the difference in y-coordinates. Each row of plots is difference in coordinates when various orders of aberration terms added as indicated in the far left of each row. X-axis of the plots is wavelength in microns, y-axis is the difference in the coordinates in mm	79
5.2	Scatter on the left shows the selected features' positions on CCD across different orders of ThAr spectrum from the instrument that are used for optimization. The plots in the upper right panel and the lower right panel are the differences in high dispersion and cross dispersion coordinates of measured positions and optimized model predicted positions for all the features used for optimization	80
5.3	Left: Selected test features' positions across different orders used to test the accuracy of the optimized model. Right: Scatter of residuals for test features. The box represents one pixel	81
5.4	A new set of 300 lines selected for optimization to test the effect of number of features used for optimization on the accuracy of the optimized model	82
5.5	Scatter of test features' residuals in position for optimization using 92 features (left) and 300 features (right). Right panel shows a more symmetric scatter centred around (0,0)	83

5.6	Residuals of the high dispersion axis coordinates of 550 features used for optimization with weighted mean square as the merit function. Top panel: Difference between measured and optimized model predicted high dispersion axis coordinates versus High dispersion coordinate of the respective feature, Bottom Panel: Difference between measured and optimized model predicted high dispersion axis coordinates versus Cross dispersion coordinate of the respective feature	84
5.7	Residuals of the cross dispersion axis coordinates of 550 features used for optimization with weighted mean square as the merit function. Top panel: Difference between measured and optimized model predicted cross dispersion axis coordinates versus High dispersion coordinate of the respective feature, Bottom Panel: Difference between measured and optimized model predicted cross dispersion axis coordinates versus Cross dispersion coordinate of the respective feature	85
5.8	Histogram showing the number of features selected for optimization in different orders	85
5.9	Black scatter points are same as Fig 5.6 and Fig 5.7. These scatters are over plotted with the respective residuals of the 233 features (a subset of the 550 features) after the model was optimized using the 233 features	86
5.10	Scatter of 1000 test features' residuals in position for model optimized using 233 features and weighted mean square error as the merit function. Blue: Residuals before the polynomial fit to correct for the residual patterns seen in Fig.1.9, Green: Residuals after the 2D polynomial fit to correct the residual patterns seen in Fig.1.9	87

-
- 5.11 Difference in high dispersion coordinates of measured and optimized model predicted positions of the test features for different features used. The features in the left are in the red region and the blue region is to the right. The two black solid lines depicts the 0.1 and 0.05 limits 88
- 5.12 Residuals around the dispersion solutions in. Open circles are the residuals around a IRAF based polynomial, solid square points are residuals in the model based technique. 91
- 5.13 Top panel: Error in measured positions of selected features in pixel. Bottom panel: Uncertainties in the model predictions of the same features from the photon noise in the features selected for optimization. The patterns seen in the bottom panel are the result of the instrumental behaviour for changing parameters 91
- 5.14 Plots show the variation in parameters (X & Y-tilts of Echelle grating, X & Y tilts of the Camera1 and Field flattener interface) over number of optimization runs on the same set of features. The bold lines in each plot shows the bounds used for respective parameters in the optimization. The degeneracy in the parameter set causes the variations over different runs. It can be observed that the parameters vary about a mean value which will form the initial parameter set during operations after the alignment. 93
- 5.15 Spectrum shift predictions by model. Shift in the high dispersion direction for two different spectra with respect to a reference spectrum as predicted by the optimized model. . . . 94

5.16	Shift in spectrum in two different orders (along columns) with respect to a reference spectrum for two different images (top) and (bottom). Solid Squares are the model predicted shifts and the open circle are the measurements from the instrument exposures. This shows a different shift patterns in the spectrum shifts in different cases and the performance of the models predictions for the same.	95
5.17	Difference in high dispersion coordinates of centroids of the two fiber images in two orders in a spectrum (left and right subplots). Solid squares represent the model predictions and the open circles are the error bars for the measurements from the CCD exposures. Model optimized using one fiber spectrum is able to track the second fiber spectrum.	96
5.18	Error bars showing the difference in the spectrum shifts between the two fibres for two orders (left and right subplots). Solid squares represent model predictions and the open circles are the measurements from the CCD exposures.	96
6.1	Focal ratio degradation of typical fiber is compared to the throughput of a circular aperture of the same diameter as the core of the fiber (Ramsey 1988)	101
6.2	The radial profile of the image taken by $1k \times 1k$ system is shown. (top) A Gaussian profile fit is shown here. Clearly a single Gaussian profile does not fit the wings of the stellar profile (bottom) with a moffat profile fit	103
6.3	Growth curve for $1k \times 1k$ images. The x axis is the aperture radius and y axis is the difference in magnitude for the successive apertures. Different curves are for different seeing. Seeing values are between 1.38 to 1.98"	104

6.4	Zoomed version of Fig.1.2. Here we can clearly see that the error in the magnitudes becomes equal to aperture correction by around 11 pixels. The errors shown are 1σ values.	104
6.5	Errors in the instrumental magnitude and flux are plotted for one observation for a seeing of $1.38''$. The error is maximum close to the centre of the PSF and start to decrease as more flux from the star is added. However beyond 8 pixel radius the error again start to rise. The minimum value was	105
6.6	Simulated illuminations at the Apogee CCD plane of the guider system when a star is centred in the pinhole for different seeing values shown on the top of the panels. The colour indicates relative illumination in each panel	106
6.7	Simulated illuminations at the Apogee CCD plane of the guider system when a star is displaced in the pinhole for $1.5''$ seeing. The colour indicates relative illumination in each panel	107
6.8	CCD images simulated for seeing= $1.1''$ for star image left: centred in pinhole, right:displaced by $0.25''$	108
6.9	CCD images simulated for seeing= $1.1''$ for star image leftt:displaced by $0.46''$, right:displaced by $0.96''$	109
6.10	CCD images simulated for seeing= $1.1''$ for star image leftt:displaced by $1.12''$, right:displaced by $1.53''$	110
6.11	CCD images simulated for seeing= $1.5''$ for star image leftt:displaced by $0''$, right:displaced by $0.25''$	110
6.12	CCD images simulated for seeing= $1.5''$ for star image leftt:displaced by $0.46''$, right:displaced by $1.5''$	111
6.13	Zemax simulation of effect of atmospheric dispersion at the telescope focal plane at a zenith angle of 70 degrees for various wavelengths colour coded	113

-
- 6.14 Gyration in the image at the telescope focal plane from the ADC rotation for different zenith angles. The circle around indicates the pinhole 114
- 6.15 The expected residuals (left) in mm at the focal plane of the telescope for the extreme wavelengths after correcting for atmospheric dispersion using the manufactured ADCs. Right: The expected angle of rotation in degrees for the ADCs for different zenith angles 115
- 6.16 Ellipses traced from the beam deflections by rotating ADCs for two lasers (green and red). Black ellipses represent expected performance by the modelled ADCs described in text, while the coloured represents the measured deflections of the laser beam on a target at a distance 10.36m. Axes are the x and y distances in mm from the non-deflected beam position on the target obtained without ADCs in the path 116
- 6.17 Experimental Setup for testing the image scrambling by optical fiber in the Measurement Standards Lab, Callaghan innovation (top) Lab setup used to feed the optical fiber (bottom) Re-imaging optics used to image the output end of the fiber . . . 117
- 6.18 Left: Images showing the position of the slit image on the fiber input end for 14 different cases. First column shows the images when the slit image is traced in the x-direction, second column when the slit image is traced in the y-direction. Right: The shift in centroids with respect to the 4th image in each column of the images in left. First column are plots for centroid shift in x-direction and second column when the centroid shift in y-direction for two different sets of images taken. X-axis in each plot is the image number (left panel), y-axis is the relative shift measured in pixel. Red and black lines are explained in the image 118

- 6.19 Left: Images of output illumination for the respective 14 different cases shown in Fig 6.18. First column shows the images when the slit image is traced in the x-direction, second column when the slit image is traced in the y-direction. Right: The difference in FWHM of each image with respect to the 4th image in each column of the images to the left. First column are plots for difference in x-direction FWHM and second column are difference in y-direction FWHM for two sets of images taken. X-axis in each plot is the image number (left panel), y-axis is the relative FWHM difference in pixel. Red and black lines are explained in the image 119

List of Tables

5.1	Performance comparison for optimizations using 92 ad 300 features.	83
5.2	Mean and Standard deviation of test features' residuals	87
6.1	Expected and measured laser beam deviations.	114

Chapter 1

Introduction

In 1835, French philosopher Auguste Comte (1798-1857) wrote in his *Cours de Philosophie Positive*[14], with reference to stars: “*We understand the possibility of determining their shapes, their distances, their sizes and their movements; whereas we would never have any means to understand their chemical composition, or mineralogical structure, and, even more so, the nature of any organised beings that might live on their surface.*”

With the advancement in the field of spectroscopy, studying chemical composition of stars has become a routine process in stellar spectroscopy. Spectroscopy is used to study the nuclear processes that happen inside stars. This also has helped us to reconstruct the history of formation of our own solar system. Large spectroscopic surveys have now enabled us to study the large scale structure and formation of the universe in detail. Spectroscopy helps to study the physical conditions, chemical content and the kinematics of the spectral line emitting region. Spectroscopy is used for study the cosmic chemical evolution, galaxy formation and evolution and different types of supernovae. However the intriguing philosophical question of nature of intelligent outside earth is still an open problem. With the precision stable spectrographs and precise photometry, now it is possible to detect planets around stars and also study the nature of their atmospheres. We may soon

get a glimpse of a possible life outside our earth in the coming years!

1.1 Historic overview of spectrograph design

Early spectrographs employed dispersing elements consisting of prisms and/or gratings. However, the development of efficient slit and collimator spectrographs in the mid-nineteenth century finally led to the growth of stellar spectroscopy. Lord Rayleigh showed that diffraction gratings are better suited to high resolution spectroscopy than the prisms [41]. But the efficiencies were low as the light gets dispersed in to a number of orders. By 1912, blaze gratings were manufactured and are in use by 1924. The blaze grating based spectrographs were found to be useful and efficient. Even with all these advancements, flexure was still a problem till the introduction of the coude spectrographs. With the coude spectrographs, large gratings and photographic plates could be used along with long focal length cameras for high dispersion observations.

Echelle gratings were proposed by Harrison that operates at incidence angles greater than 45° , the direction of incidence being normal to the narrow side of the grooves [21]. These gratings can operate at very high orders, even more than 100th order.

In the recent years, there are considerable improvements in the designing and building of spectrographs, though the basic components of spectrographs remained the same during these years. White pupil configurations [3] have improved the system efficiencies. The disperser is re-imaged onto the camera and the monochromatic beams intersect forming a new pupil at the entrance pupil of the camera.

1.2 Historic perspective of precision radial velocities

High resolution spectrographs were thought to give precise radial velocities, to detect planets [50]. However, only few km/s were possible, it was limited due to accurate calibration. The light path and the illumination of the calibration light were different compared to the stars. Griffin & Griffin [19] used the telluric lines for wavelength calibration and was able to reach several tens of meters per second radial velocities. Telluric lines itself is variable due to wind and other environmental condition to 10-20m/s and hence not ideal as a precise standard. There were attempts using toxic HF cells as wavelength calibration, which improved the velocity precision to 15m/s [12]. This was later replaced by non-toxic iodine cell [31] and this has become one of the standard technique for achieve precise radial velocities. Mayor and team commissioned ELODIE spectrograph [32] on the 1.93-m telescope at OHP (Observatoire de Haute-Provence), France, which used a simultaneous ThAr technique. They use fibers to mitigate variable slit illumination in coudé spectrographs due to seeing, tracking errors causing the shift in the spectrum at the detector plane. Optical fibers with their high efficiencies, ability to scramble the image at the output side has given the advantage of placing the spectrograph far from the telescope in environmental stabilized chambers, with a uniform and constant illumination at the slit plane [39].

These along with precision thermal and pressure controlled environment for spectrographs, vacuum enclosures have led to high stable instruments leading to high precision spectroscopy. Also for high resolution spectrographs, image slicers [40] and anamorphic pupil slicers [48] improved the efficiencies for narrow slit widths.

The past decade has been about development of high precision spectrographs. The optical fibers and vacuum chambers along with the simultaneous

reference calibrations have provided the mechanical stability needed for these spectrographs achieving a 1m/s stabilities [39]. For science cases like dynamical measurement of accelerating expansion of universe, extra-solar earth twins, temporal variability of physical constants, the 1m/s stability need to be pushed further to sub-m/s. Following HARPS that reached a 1m/s stability, projects like ESPRESSO [33] and CODEX [38] are being developed to reach 10cm/s and 2 cm/s stabilities respectively. Currently the limits that need to be addressed to meet these precisions are: stable light injection, detector stability and wavelength calibrations.

The incomplete scrambling of the circular optical fibers retains the information regarding the position of the image on the input end of the fiber which is transferred into spectrum shifts. Both the near field and far field are affected due to the incomplete scrambling. While the near field shifts the centroid of the fiber illumination at the slit, the far field changes the pupil illumination in the instrument affecting the relative quantities of different aberration terms. As the simultaneous reference cannot see this effect, these shifts cannot be corrected by it. New fiber shapes (square and octagonal) other than circular are under testing, which so far have shown better scrambling properties than circular fibers [13]. Another technique being tried is a double scrambler [23], in which the near and far field are interchanged between two fibers. But the main setback of this technique is efficiency loss during the light coupling between two fibers.

Finally the long term stability of this approach relies on the accurate wavelength calibration of the reference spectrum. Hence, calibration is a crucial aspect in analyzing and deducing results.

As shown in Fig.1.1 shows a flow chart, how an observation finally lead to an understanding and final interpretation. An observation technique O (the spectrograph) is applied on a subset of the universe, \mathbf{u} and raw data \mathbf{d} is obtained. A calibration procedure C is then applied on \mathbf{d} to get back \mathbf{u} , which is our *perception* of the universe. A calibration procedure should

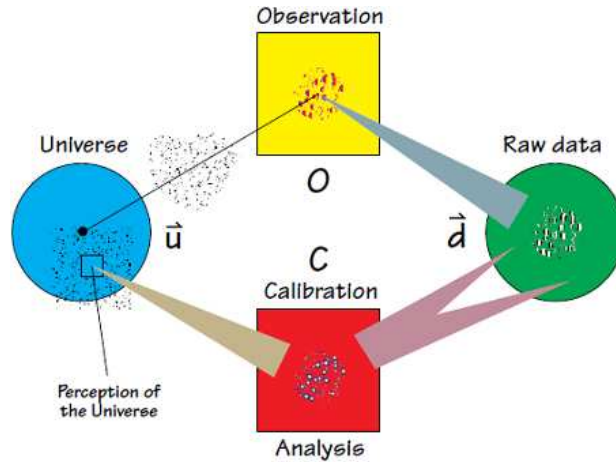


Figure 1.1: A cartoon depiction of an observation procedure and perception of the Universe. (By Rosa M)

remove all relevant signatures imprinted on the science light from its target to the detector readout. Therefore it is very important to describe, understand and minimize the statistical and systematic errors in the measuring process. In the context of astronomical spectrographs, an ideal calibration to provide accurate wavelength calibrations should have the following features, the lines from the calibration lamp should be sharp unresolved lines and allow accurate measurement of their central wavelength, wavelengths should be traceable to laboratory standards, wavelength remain constant under all operating conditions, evenly spaced lines with density appropriate to the resolution, all the lines at a constant intensity, minimal variation over the life time of the lamp, and the lamp spectrum should be reproducible from lamp to lamp [25].

Thorium Argon (ThAr) hollow cathode lamps (HCL) provide good number of lines in UV-visible-near IR region and have been in use for a very long time. Other advantages is thorium has only one stable isotope ^{232}Th , which is an even nuclei hence there are no additional features due to isotopic shift and hyperfine structure, which leads to narrow, highly symmetric line profiles. For all these reasons, Thorium Neon (then) and ThAr HCLs have become the standard for wavelength calibration of astronomical spectrographs [28]. But at moderate spectral resolutions, blends are a problem for high precision

wavelength calibrations even at $Rq \geq 150000$ and different lines have widely different intensities and the distribution of these lines is not uniform.

Radial velocities are obtained from the extracted star spectra by cross-correlation with a stellar template using the highly accurate wavelength calibration obtained at the beginning of each night. Then, the correction for the instrumental drift is performed [29]. The technique consists of feeding the spectrograph with two optical fibers, the so called object fiber and the reference fiber. These fibers are aligned in the cross dispersion direction at the spectrograph entrance to form two nearby but well separated spectra on the CCD. At the beginning of an observing night both fibers are fed by a spectral lamp — in this case a ThAr lamp — in order to determine the wavelength solution $\lambda(x, y)$ of the CCD ($x, y =$ pixel coordinates). This calibration procedure is performed for both "channels" separately.

Typically it is carried out before the beginning of the observations and the wavelength solution remains valid for the whole night. The observations are then performed by feeding the object fiber with the object light and the reference fiber by the ThAr lamp. The object spectrum is calibrated in wavelength using the wavelength solution of the object fiber determined at the beginning of the night. The radial velocity of the object is determined by cross correlating the measured spectrum with a numerical mask adapted to the spectral type of the star. The position of the correlation peak is a direct measure for the Doppler shift of the stellar absorption lines and hence for the radial velocity of the object. The ThAr spectrum simultaneously recorded on the same CCD frame serves "only" to track the instrumental drifts during the night. For this purpose the "velocity" of its spectral lines is computed by cross correlation of the ThAr spectrum with a numerical ThAr mask. This velocity, which is zero in case of no drifts, measures the instrumental drift between the moment of the calibration at the beginning of the night and the moment of the observation of the object. Finally, the measured RV of the object is corrected by subtraction of the ThAr velocity, eliminating thus the

effects of instrumental drifts.

In order to achieve a high accurate and stable wavelength solution, good estimate of the line centroids and highly accurate wave lengths of the lines should be known. As mentioned earlier, most of the ThAr spectra lines are blended, and given the polynomial fitting used in regular data reduction packages, the solutions lack the ability to give accurate stable results in the regions with no or less lines.

Radial velocity and transit efforts are now beginning to extend to M dwarfs, the most numerous stars, where the lower luminosity shifts the habitable zone much closer to the star. These emit most of their flux in the 1-1.8 μm region (NIR J and H bands). In the NIR J and H bands Th lines are few and relatively faint, making it difficult to find accurate dispersion solutions in the J and H bands without substantial integration time [30]. High contrast between Th and Ar lines in this region leads to scattered lines and increasing the integration time to get enough signal for the Th features saturates the Ar lines causing bleeding and contamination in adjacent orders.

With these limitations faced from the ThAr HCLs, the astronomy community is searching for new calibration lamps and techniques like the broad band laser frequency combs [52], Fabry-Pérot cavity illuminated by white light lamps [51] , various absorption cells [30] etc.

1.3 Accurate chemical abundances

Some of the main criteria for accurate stellar abundances are high spectral resolution, high signal to noise ratio and large wavelength coverage. High resolution is preferred so that the blended lines are resolved. Abundances of astrophysically important isotopes like ^6Li and ^7Li ratios have not been accurately determined even with very high signal to noise ratio spectra. The lithium line at 670nm is a doublet line, having contributions from two isotopes (^6Li & ^7Li). Hence, only a high sampled, high resolution and high signal to

noise ratio spectra can help in determining the accurate abundances. Most of the high resolution Echelle spectrographs have typical slit sampling of 2-pixels and they use slicers and have a long slit. While extracting the spectra the pixels along the slit length is added to get better S/N, which assumes all the pixels that are added have same wavelength. For accurate isotopic abundances, where a given line profile needs depends on the wavelength of the hyperfine lines, isotopic ratio and individual abundance, it is important to accurately know the wavelengths of the pixels that are added along the slit length direction. Similarly, other important isotopic abundances of Mg is important to study the origin of Magnesium, whether it is produced by a supernovae (SN) or an AGB (asymptotic giant branch) star. SN and AGB stars produce Mg isotopes in different ratios. The isotopic ratios of n-capture elements (Sr, Ba, Eu) are important to distinguish the contribution from slow and rapid n-capture process, which is produced in AGB stars or in a core-collapse SN. One of the open problem in astrophysics is the origin of rapid n-capture process. The current thinking is that they can be produced during a neutron star – neutron star (NS-NS) merging process or during a core collapse SN. Isotopic abundances of heavy elements and the abundances of heaviest possible n-capture elements help to constraint these scenarios. Detecting rare earth elements like Uranium and Thorium lines are necessary to understand the conditions of n-capture, this study warrant, high resolution, high S/N spectra.

Except for these isotopic ratios and heavy rare earth elements, accurate determination of chemical abundances is limited due to the accuracy of stellar parameters and the stellar atmospheric models itself. Recently, Kepler and COROT data has revolutionised the area of exoplanets and also the field of Astroseismology. Unlike stellar spectroscopy, Astroseismology can probe the interiors of a star through the acoustic waves. These acoustic oscillations can be detected as tiny variations in the flux or as tiny shifts in the spectral lines. Both these detection techniques are complementary to confirm the acoustic

modes. The inversion of these modes gives accurate stellar parameters of a star, which can be combined with spectroscopy in obtaining accurate abundances.

1.4 physical model based calibrations

It is to be observed that over all these decades of work on spectrographs and their calibrations, the instrument physics is seldom used in the calibration work. Once the instrument is installed the physics that went into the designing and building of the instrument is not used in its calibrations. Using the physics of observation procedure will give a predictive power to the calibrations reducing the necessity of having high number of data points covering the whole region of interest.

A physical model based calibrations for astronomical instruments was proposed by Rosa [43]. He proposes to work out C in Fig.1.1 by working out O. He proposed a two step procedure:

Step 1: Physical principles of the instrument into a code which can simulate observational data. This code will give a physical model of the instrument that will be able to generate calibration references that are noise free and it contains controllable engineering parameters.

Step 2: Optimizing the controllable parameters in the model to match the working of the built instrument through calibration frames taken from the instrument. The ESO group has successfully implemented a model based calibration approach to instruments such as FOS and STIS on HST, CRIRES and X-shooter on VLT [7, 8, 26, 44].

According to Bristow et al [8], the life cycle of an instrument can be described as following:

1. Science requirements
2. Optical Design

3. Engineering Expertise
4. Testing and commissioning
5. Operation and data flow
6. Calibration
7. Scientific data and archive

Once the instrument is installed and put to use, from experience it is known that the know-how and expertise that went into design and building the instrument is not put to use in calibration procedure. A case the ESO group has explored is the wave length calibrations of spectrographs. The conventional empirically derived dispersion solution is replaced with a physical model technique. The group has discussed the aspect if the physical description improves the final science product. In their words “the advantage is rather obvious since the relevant physics provides predictive power which is limited for a polynomial. It is shown that the accuracy of calibration can be significantly improved. The use of physics will usually be advantageous as long as the instrument remains stable during operations and as long as the physics can be well described. If these conditions are not met the effort associated with the physical modelling can become very large and its benefit may become questionable.” [24].

Taking this into confidence and their demonstration of the technique on some of the instruments; and with the well established physics of high resolution spectrographs and cameras, the physical model based technique’s applicability for Hanle Echelle Spectrograph (HESP) was taken up. We attempt to demonstrate the possibility of developing an accurate model of the instrument and demonstrate its performance. Unlike the ESO team whose modelling approach is on-axis limited with the all aberration corrections applied together as a polynomial at the detector plane [7], the scheme we present here, aims at providing the exact position of chief rays on the detector plane leaving only

the centroid corrections, which are of the order of sub-pixel as a correction at the detector plane. This reduces error propagation through the system, and the degeneracy states for the optimization routine to predict the instrument status. This is achieved using paraxial ray tracing and including exact corrections for certain surface types and Buchdahl aberration coefficients for complex modules such as camera systems.

Some of the uses we foresee for this technique in regard to the wave length calibration challenges faced by the high precision spectrographs are:

1. Using the predictive power of the model for better calibrations where there are no or very few lines of Th in the calibration frame. As discussed earlier, one of the limitations faced from the ThAr lamps is the non-uniformly distributed, high contrast intensity lines that cause unstable wave length calibrations. Just with few lines across the spectrum which are of enough intensity and high accuracy wave lengths and the predictive power of the model this limitation can be overcome.
2. A more accurate dispersion solution compared to the empirical fits
3. Better instrumental drift corrections in the simultaneous reference observations. When using spectrographs that cover a wide band width, the instrumental drifts across the spectrum need not be constant for the environmental change may have non-linear effect on the instrument behaviour. A model if able to predict these drifts accurately; more accurate instrumental drift corrections for RV measurements will be possible.
4. One of the assumptions for using the simultaneous reference observations is that the drift in object fiber is same as the reference fiber. But there will be higher order differences in these drifts between the two fibres. One of the tasks of the model is to predict these differences.
5. Order tracing and better 1D spectrum extraction: Model should predict

the curvature and tilt of the order. Also the field dependent and wave length dependent tilts in the feature shapes if can be predicted by the model, the extraction efficiencies can be improved. This in conjunction with the more accurate dispersion solution can help in better estimates of Li isotopes.

6. Tracking the instrument status: The technique will also provide details about the different physical parameters of the built instrument and can keep track of the long term trending of these. This gives a way to study the instrument's behaviour and performance over a period of time.

As the performance of this technique is highly dependent on the accuracy of the model developed no pre-calculations were attempted for any intended improvements in the calibrations. The layout of the thesis is as follows: Following this chapter 2 describes HESP, the instrument underdevelopment for which the physical model is developed. Chapter 3 presents the theoretical formulation of the physical model in detail. Chapter 4 describes the measures taken to match the model with the built instrument. Results of the model's performance in the laboratory alignment of the instrument are presented in Chapter 5. In chapter 6 some aspects in HESP that may cause a difference in illumination between object and calibration fiber are discussed followed by the final conclusion and prospects for future work.

Chapter 2

Hanle Echelle Spectrograph

2.1 Introduction

Hanle Echelle Spectrograph (HESP) is a high resolution fiber fed Echelle spectrograph developed jointly between Indian Institute of Astrophysics (IIA) and Kiwistar Optics, Callaghan Innovation (CI), New Zealand. This project is supported by DST (Department of Science and Technology, India) grant IR/S2/PF 02/2010 under IRHPA scheme. The instrument is built for the 2m Himalayan Chandra Telescope (HCT) at the Indian Astronomical Observatory (IAO), Hanle. The observatory is located at 4500m above sea level, with a nominal pressure of 0.58atm. Nominal humidity at the place is 30% but can vary from 5% to 90%. The seasonal temperature variation at the site goes from -30 °C to +20 °C and can have a 10 °C temperature change over night.

HCT is a 2.01m Ritchey-Chretien, alt-azimuth mount optical telescope. It has an instrument cube at the cassegrain focus with 5 ports that can be mounted simultaneously. The beam at the cassegrain focus is F/9 with an image scale of 11.5 arcsec per mm. The usable field of view of the telescope is 7 arcmin and 30 arcmin with the corrector. The telescope tracking tests

indicate that a tracking accuracy (open loop) of 0.5 arcsec over 10 minutes is met at a good fraction of telescope positions, except at higher elevations, where the tracking worsens, resulting in a mean (over all telescope positions) accuracy of 1.38 arcsec over 10 minutes. The telescope is also equipped with an auto guider system (AUGUS) developed at the Copenhagen University observatory, which uses an off axis object from a 97 sq. arcmin field of view away from the telescope field of view to guide the telescope.

The instrument cube of the telescope is currently equipped with TIFR Near Infrared Spectrometer and Imager (TIRSPEC), an optical CCD imager and Hanle Faint Object Spectrograph Camera (HFOSC). HESP will be the new edition to the instruments with the telescope. HCT instruments are operated remotely from IIA operational centre in Bangalore.

HESP is designed to operate at two spectral resolution modes, $R=30000$ and 60000 , covering a wavelength range of 350nm to 1000nm on a single $4k \times 4k$ detector in a single exposure. The spectrograph is fed through a 27 m optical fiber link from the cassegrain port at the telescope to the bench mounted spectrograph that is located inside a thermal enclosure in the ground floor of the observatory.

Following are some of the science objectives for the spectrograph.

Stellar Composition Studies: The chemical composition of stars, their abundances and isotopic abundance fractions are good indicators of the evolutionary status of the star occupying different regions of HR diagram. Abundances of heavy neutron capture elements are also very good diagnostics of various evolutionary processes occurring in stars of different mass range. To derive the chemical composition one requires the strengths of clean unblended spectral lines for each element of interest. Accurate line strength measurements of weak lines especially below 400nm require a spectral resolution of $R \geq 60000$ or better. The line components resulting from isotopes of an element are generally separated by a small fraction of an angstrom. The measurement of isotopic

abundance fraction requires very high resolution spectra.

Binaries and extra-solar planets: For different families of stars such as pre-main-sequence stars, Post-AGB stars etc the presence of companions play very important roles in defining their evolutionary status. Some of the chemical peculiarities exhibited by post-AGB and RV Tau stars can be better understood in the framework of circumbinary environments. The list of known post-AGB stars with binary companions is growing steadily (Van Winckel 2003). Binary companion for Pre-Main sequence star HD 34700 was detected by Arellano Ferro and Giridhar (2003). Hence the search of low mass companion is considered a very important area where both the long term and short term monitoring yields very interesting results.

Detection of planets of Jupiter-size around other solar-type stars extremely precise radial velocity measurements (of the orders of tens of m/s). A dedicated instrument giving a complete spectral coverage from 370nm to 900nm on a single CCD frame is necessary to meet the required precision. It can significantly increase the detections of such systems, It should be noted that instruments like HARPS (High Accuracy Radial Velocity Search; Queloz and Mayor 2001; Pepe, Mayor and Ruprecht 2002), SARG (Spettarografo Alta Risoluzone Galileo; Gratton et al. 2002) and FEROS (Fiber fed Extended Range Optical Spectrograph; kaufer and Pasquini 1998) mounted on 1.5 to 2-m class telescopes have made significant contributions to this field. CORALIE and ELODIE (Baranne 1997) have made significant contributions to the detection of large number of planets with short-period orbits (P < 20 days). Measurement of $^6\text{Li}/^7\text{Li}$ isotopic ratio in planet harbouring stars is an excellent tool to test different theories of giant formation.

Doppler Imaging of spotted stars: Doppler imaging technique (DPI) is an indirect elaborate computational technique to invert a series of high-

resolution spectral line profile into an image of stellar surface (Donati et al. 1997). The development and refinement of this indirect stellar imaging technique over two decades has made DPI one of the most reliable tools to estimate spatial distribution of the temperature and chemical abundances over the stellar surface. It requires high-resolution ($\lambda/\Delta\lambda \approx 60,000$) and high signal-to-noise ratio ($S/N \approx 200$) spectra with a good phase coverage. This method is being employed to reconstruct star-spot patterns on the stellar surface and monitor them over long periods of time. Stars like RS CVn binaries with their known surface activities could be used to explore the possibility of their surface features showing regularity similar to the sun-spot butterfly diagram (Vogt et al. 1999).

Astroseismology: To fully understand the evolution of stars, detailed information on the processes acting in the stellar interior is needed. Since the stellar interior is not directly accessible, asteroseismologists use the indirect information contained in stellar oscillations to probe the stellar interiors. There are two families of modes carrying information on different parts of the stellar interior: pressure modes (p-modes; mainly propagating in the envelope) and gravity modes (g modes; mainly propagating in the core). For a unique asteroseismic modelling, a large number of well-identified modes are needed. Asteroseismology also provides clues to test the internal structure and chemical composition of solar type stars like alpha CMi (Procyon A) by measuring frequencies and amplitudes of p-mode oscillations in these stars. In radial velocity, p-modes have been detected but there is no agreement on the actual frequencies due to insufficient high-quality observations. Additional data with high S/N in power spectra and increased temporal coverage with multi-site campaign are needed to determine the amplitude, the rotational splitting and the damping time of p-modes in Procyon A like

stars.

Post-AGB stars: PAGB stars are excellent probe for diagnostic properties in the study of dramatic morphological and chemical changes taking place at the latest stage of evolution of low and intermediate mass stars (approx mass range 0.8 to 8Mo). The extensive nucleosynthesis at AGB and mixing processes (dredge-ups) change the surface composition of the star over a short time (a few hundred to thousand years) and synthesized elements are ejected to interstellar medium (ISM) through strong mass-loss preceding the post-AGB phase. AGB stars are therefore major contributors of C,N,F,Al, Na and s-process elements to ISM and hence play crucial role in the chemical evolution of galaxies.

Classical post-AGB stars contain low metallicity stars of F-G spectral type and high galactic latitude distribution. Their Spectral Energy Distribution (SED) shows characteristic double-peak components. The optical peak arises due to the central star while IR peak is caused by the dust grain in the circumstellar envelope. The chemical composition studies show that they come in two flavours- Carbon-rich PAGBs showing s-process enhancement caused by sufficient number of thermal pulses and efficient dredge-up and the Oxygen-rich PAGB share the spectral type and SED shape except s-process enhancement.

Post-AGB stars masquerading as metal-poor stars spectra resemble those of metal-deficient stars due to systematic depletion of condensable elements observed initially for HR 4049, BD+39o 4926, HD 52961 and several others (see De Ruyter et al. 2006 for a full compilation). The abundance pattern shows strong dependence on the predicted condensation temperature TC for low pressure gas of solar composition. Hence, elements like Al, Ca, Ti and Sc with the higher TC (1500 to 1600K) are significantly depleted while the elements with low TC (like S, Zn) are not affected.

Above mentioned are some of the science objectives for the Hanle Echelle Spectrograph. Following lists the brief specifications worked out for the design of the spectrograph to meet the scientific requirements.

1. Wave length Range: 350 nm to 1000nm
2. Resolutions: 30000 and 60000
3. Spectrometer nominal throughput of 20%. It should be at least 12% at the extreme short and long wavelength range, but will be negotiated where limitations due to physics cannot be overruled.
4. White pupil configuration, Image slicer and graded anti-reflection coating on CCD for high resolution mode for increased efficiency
5. Provision for two science fibres and capable of the following sub modes:
 - Object only observation: The primary science fibre will be used for object only observation. This mode is useful for bright stars and short exposures below λ 600nm, where the counts from the sky contribution is very low and no crowded sky emission line bands.
 - Object + Sky observation: Two science fibres will be used simultaneously, the primary for the object observation and the secondary for sky observation. Long exposure and fainter objects require accurate sky subtraction to get accurate equivalent width for the spectral lines. Sky subtraction is also important for wavelengths greater than 600nm. Several key chemical elements Carbon, nitrogen, oxygen and sulphur have atomic transitions in the red wavelengths, which requires accurate sky subtraction.
 - Object + Reference observation: Two science fibres will be used simultaneously, one for the primary for the primary science target and the other for the wavelength calibration light input.

6. Non-referenced mechanical stability shall be better than 200 m/s absolute over the course of one observation night for a temperature stability of ± 0.5 °C.
7. Velocity precision of at least 20 m/s in Object-Reference observation mode

2.2 Cassegrain Unit

The cassegrain unit of the system comprises of optics that feed the light from telescope to the optical fibres that take the light to the spectrograph in the thermal enclosure on the observatory ground floor.

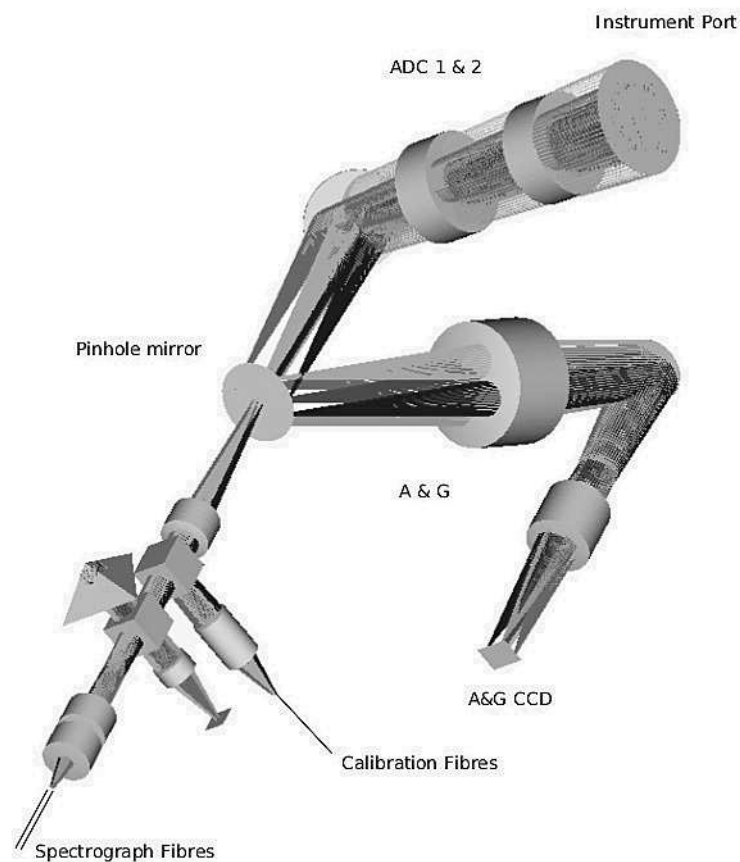


Figure 2.1: Optical layout of cassegrain unit. (Figure credit: Callaghan Innovation)

Figure 2.1 shows the optical layout of the cassegrain unit. Instrument port is the interface to the telescope through the instrument cube of the telescope. The telescope F/9 beam passes through the atmospheric dispersion correctors (ADC) and reflected off a fold mirror before coming to focus at the pinhole mirror of the cassegrain unit.

Atmospheric Dispersion Corrector (ADC) consists of two counter-rotating similar prisms. Each prism is a doublet made of glasses Ohara FPL51Y and Schott LLF1 which produces a good match for the atmospheric dispersion at this altitude. Both glasses transmit well at and below 350 nm and deliver polychromatic RMS imagery of less than $\frac{1}{4}$ arcsecond. The ADC corrects the atmospheric dispersion caused by the local atmosphere at zenith angles from 0 to 70 degrees.

A pinhole mirror tilted by 20 degrees is placed at the telescope focus. The mirror has two pinholes of 0.25mm diameter separated by 1.25mm. One pinhole collects the star light while the other collects the sky back ground. The mirror is tilted at 20 degrees to direct light to the acquisition and guiding system as shown in the Fig. 2.1.

Beyond the pinhole mirror is the relay optics to feed the optical fiber. The F/9.2 beam of the telescope is collimated using a single doublet with a beam size of 5mm. Following two identical doublets, the beam is converted F/3.6 and focussed onto the 100micron fiber tip.

The necessary calibration of the science data is facilitated using a calibration unit that is located in the spectrograph room in the ground floor of the observatory. As seen in the Fig. 2.1, calibration fibres from the calibration unit (housing the different calibration lamps) to the cassegrain unit feed the light into the collimated beam of the relay optics through a mirror or a beam splitter and will be imaged onto the science fibres. The translation mount in the collimated beam path provides three options- beam splitter, mirror and no obstruction. Fig. 2.2 depicts the different scenarios of operation for the same.

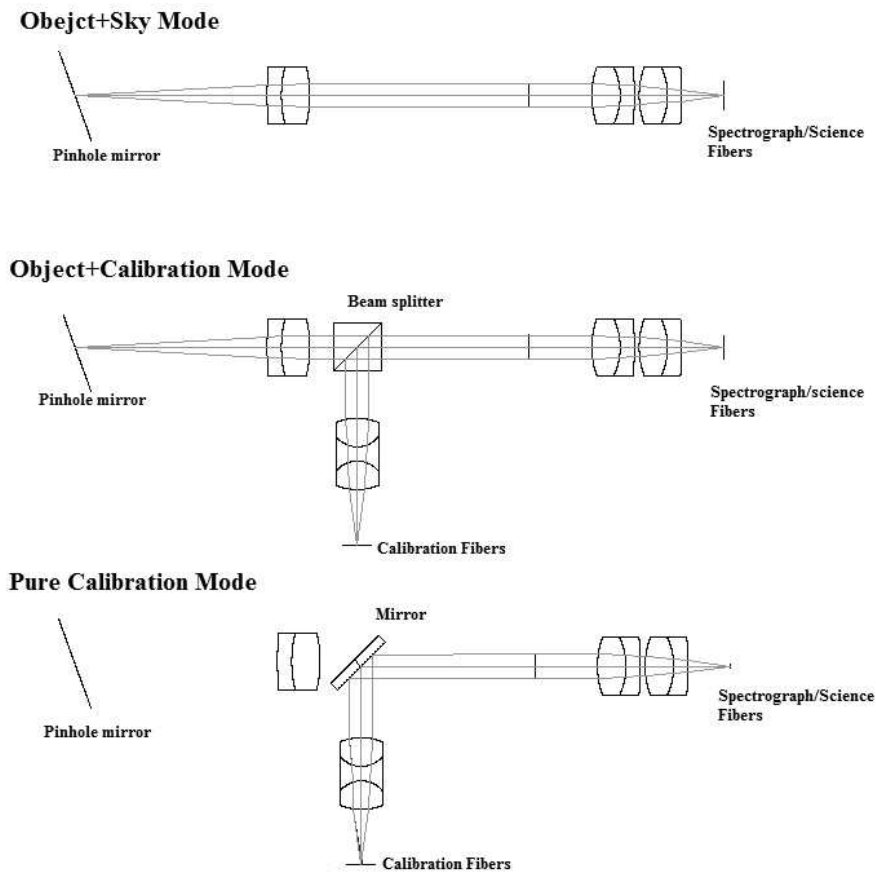


Figure 2.2: Operating Modes of Cassegrain Unit, (Figure Credit: Callaghan Innovation)

In the object-sky mode, where no calibration light will be used, the translation stage is positioned to no obstruction position. In the Object-calibration mode, where one of the science fiber is fed with object and the other fiber with calibration light for simultaneous calibration reference observations, the translation stage is positioned to place the beam splitter in the collimated beam path. The beam splitter allows 90% of the star and 10% of the calibration light. In the pure calibration mode where both the science fibres are fed with calibration light, mirror is placed in the collimated beam path, to feed both fibers with the calibration source.

2.3 Calibration Unit

Fig. 2.3 shows the calibration unit that houses the different calibration lamps for wave length and flats. A Thorium-Argon (ThAr) lamp and a Thorium-Argon-Neon (ThArNe) lamp are provided for wavelength calibrations. Quartz lamp assembly holds two quartz lamps and a beam splitter. Each quartz lamp is equipped with a coloured filter. Given the high counts in red and very small counts in the blue region of the spectral emission of a quartz lamp, the filters were chosen so that two separate flats taken with each filter and combined will yield good enough counts through out the spectrum.

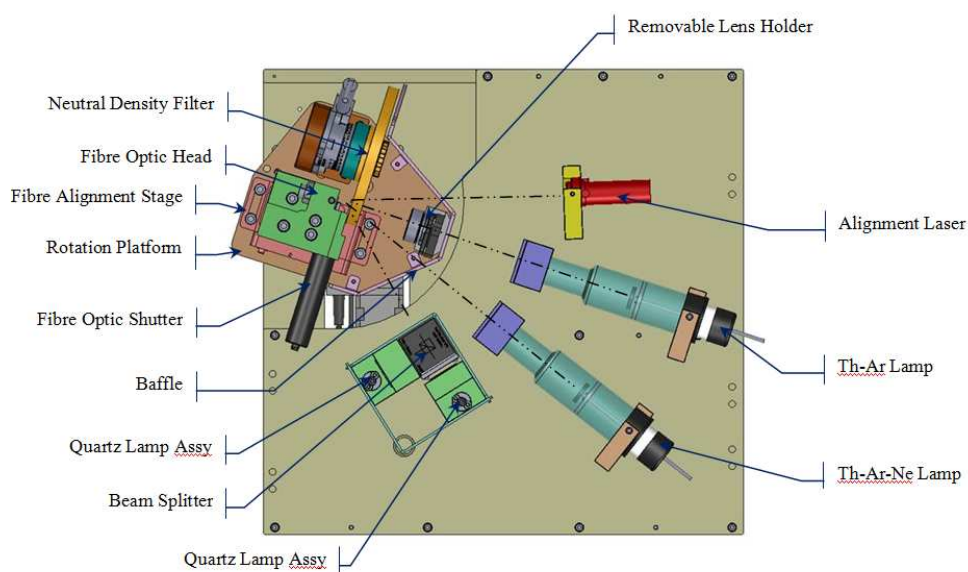


Figure 2.3: Calibration Unit top view (Image Credit: Callaghan Innovation)

The design is based on mounting the fibre optic receptacle on a rotation stage. Each lamp will be aligned and fixed in place. To select a particular lamp, the rotation stage will direct the fibre receptacle to the desired lamp. A common variable neutral density filter is positioned in front of the fibre head. A shutter is provided to select either of the two fibre feeds, or both could be shut down simultaneously. Each lamp is provided with a lens that collimates the light from the lamp as shown in Fig. 2.4 for the Quartz lamp mount. The rotation stage that holds the fiber is equipped with a lens that focuses

the light onto the calibration fiber input end. The calibration unit is placed in the thermal enclosure where the spectrograph is placed. The calibration fiber from the unit is routed to the cassegrain unit to feed the science fibres.

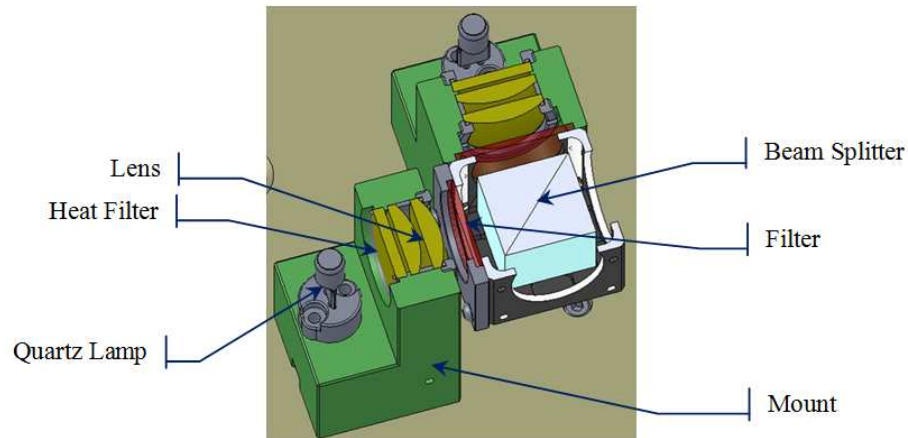


Figure 2.4: Quartz lamp mount and optics, (Image Credit: Callaghan Innovation)

2.4 Optical Fibers

Four optical fibres are used in total in the system. Two science fibres, that run from cassegrain unit to spectrograph and two calibration fibres running from the calibration unit to the cassegrain unit. All the optical fibres are similar with 100micron core diameter. The front end of the science fibres in the cassegrain unit has an optical window glued with anti-reflective coating to reduce the reflection losses. Analysis of other fibre instruments suggests that at $f/3.6$, use of an $f/3.6$ collimator will result in a loss of between 5 and 10% of the light exiting the fibre due to focal ratio degradation. A 12.5% FRD factor has been compensated for by the relay lenses that image the fibre onto the slicer.

2.5 Acquisition and Guiding Unit

Though the telescope is equipped with a guider system, the ADCs used for HESP in cassegrain unit causes a shift in the field by an amount dependent on the zenith angle. Due to this a separate acquisition and guiding unit (A&G) for HESP is required. The 20 degree tilted pinhole mirror at the telescope focus plane directs the off axis light to the A&G unit as shown in Fig. 2.1. A triplet lens collimates the 100 arcsecond telescope guiding field. An asymmetric triplet then images the guiding field onto an Apogee Alta u47 broadband CCD which is a 1024×1024 array of 13m square pixels. More about the guiding system will be dealt in the Chapter 6.

2.6 Spectrograph Unit

The spectrograph layout from the slit to the detector is shown in Fig. 2.5. Science fibres from the cassegrain unit terminate at the input of the slit optics. Three small lenses are assembled into a ferrule with each fibre. The first is cemented directly to the end of its corresponding fibre. It forms an accessible pupil for stray light control and passes the light to a second lens which produces a f/75 converging beam. The third (field) lens then forms a telecentric image. According to the resolution mode chosen, the F/75 beam either passes through the image slicer (R=60000) or the passes directly to the next optics (R=30000). The following optics convert the F/75 to F/10.45 beam for the spectrograph collimator.

2.6.1 Image Slicer

In the 60K resolution mode, where the slit size is half of the 30K mode, to improve the efficiency, an image slicer is used. The slicer produces two 1.2" slices of the 2.85" fiber. The slicer image is 6" long. Fig. 2.6 (right) shows the sliced image from an image slicer shown in Fig. 2.6 (left). The design

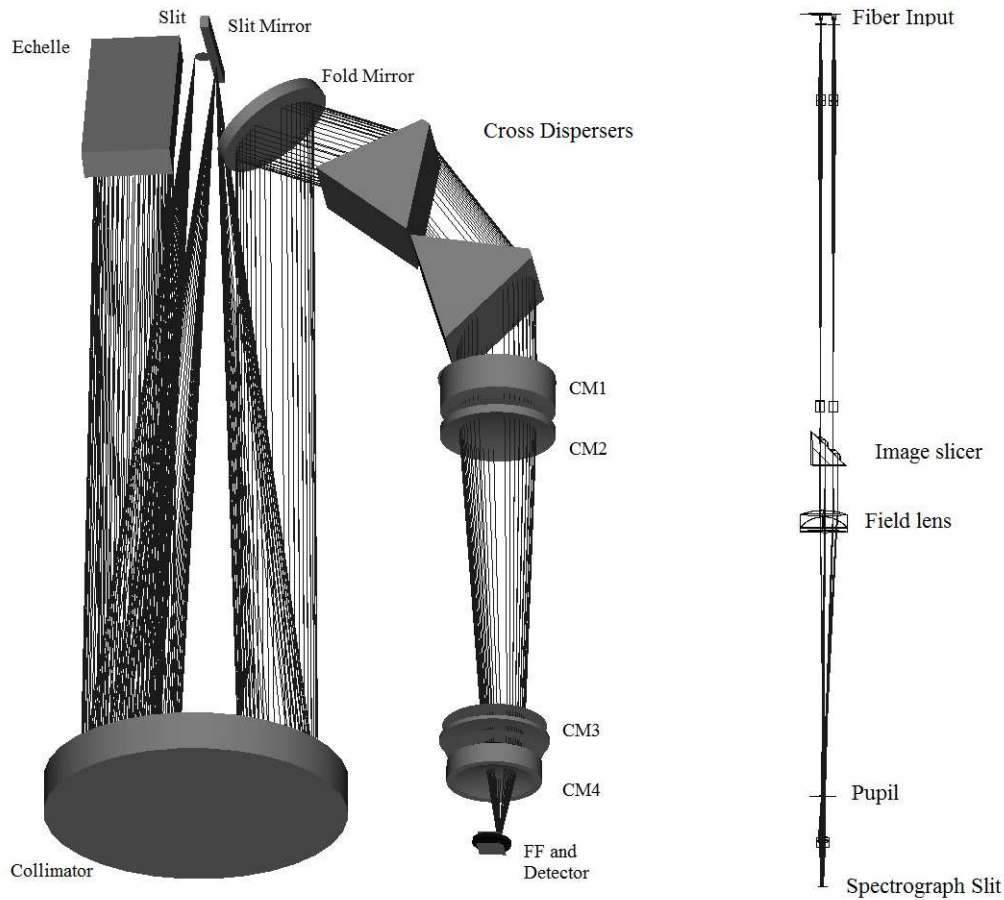


Figure 2.5: Slit optics and Spectrograph optical layout (Image credit: Callaghan Innovation)

is based on Richard Bingham's modification of the classic Bowen-Walraven image slicer. The slicer is mounted on a goniometer to align the slicer edge parallel to slit edge.

Folding prisms along with the slicing prism provide the angle required for total internal reflection at the interface of the two prisms. The beam falls at the slicing edge of the slicing prism. The part of the beam falling at the glass-air interface gets internally reflected while the part of the beam falling at the glass-glass interface passes through unobstructed. The internally reflected beam gets reflected at the ceiling of the folding prism and falls at the glass-glass interface and so passes through in the second encounter getting displaced vertically producing two slices of a fiber image displaced vertically as seen in Fig. 2.6.

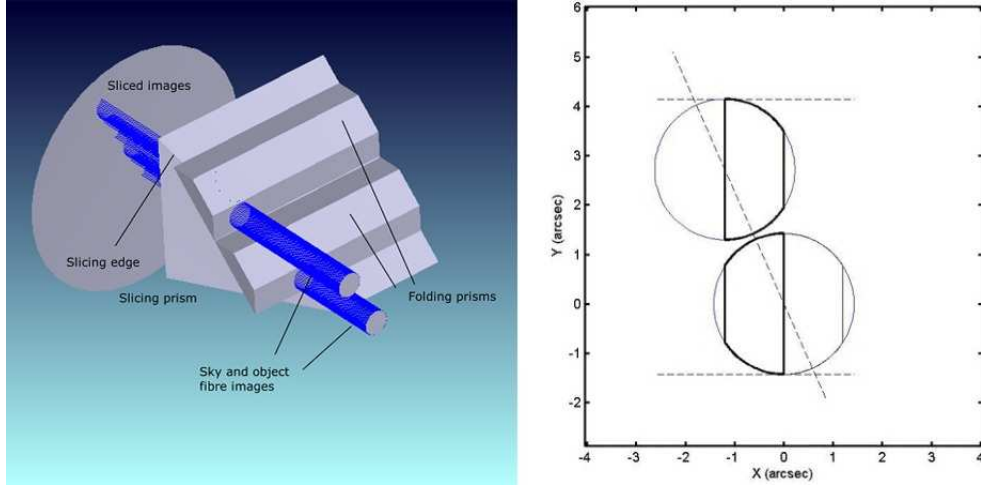


Figure 2.6: Left: Image slicer rendering showing the working of the slicer. Right: Schematic of the fibre slicing. The full diameter of a 2.85" fibre is shown being sliced into two 1.2" slices. (Image Credit: Callaghan innovation)

2.6.2 Spectrograph

A cross-dispersed near-Littrow Echelle spectrograph forms high-resolution ($R = 60000$) echellegrams of the sliced fibre inputs and lower resolution ($R = 30000$) echellegrams of the unsliced fibre inputs.

The paraboloid collimator mirror of focal length 1850 mm collimates the beam from the slit plane placed off-axis as seen in Fig. 2.5. The 177mm collimated beam from the off-axis region of the collimator then falls on the R2.15 Echelle with a 65 degrees blaze angle and 52.67 grooves per mm. The grating disperses the beam vertically with respect to the optical table and redirects it to the collimator which forms an intermediate image at the slit mirror. The beam returns to the paraboloid and gets collimated. The fold mirror placed for a compact spectrograph design on a single optical table, directs the beam to the cross-dispersers. Cross-disperser consisting of two thick prisms separating the many different orders from the echelle. The two prisms are made from Ohara BSL7Y and have apex angles of 55° . This produces the necessary order separation on the detector near the red end of the echellegram. An $f/2.7$ camera images the light from the cross-dispersed orders onto a detector to form an echellegram.

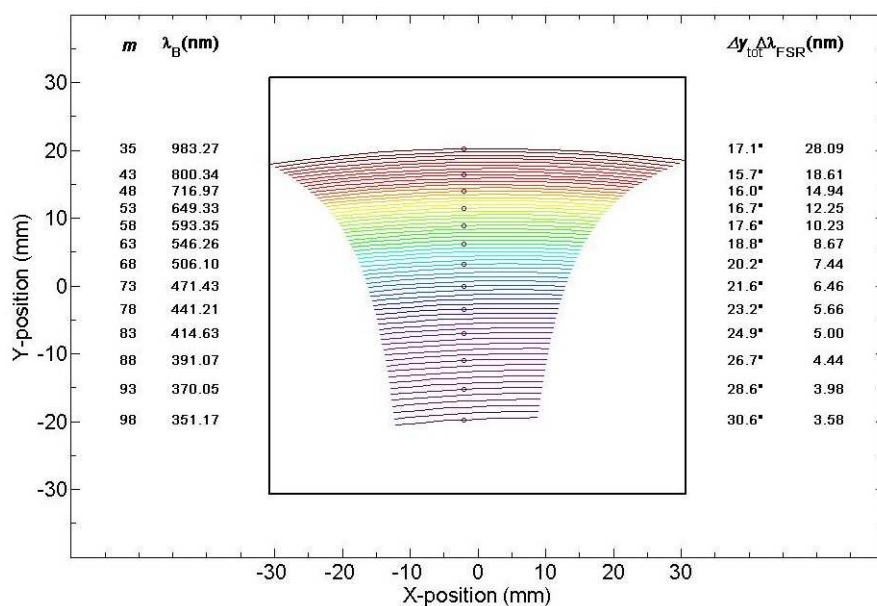


Figure 2.7: Spectral format of the designed HESP, Image Credit: Callaghan innovation

The camera is a generic Petzval configuration with a set of 4 positive groups followed by a thin negative field flattening lens close to the detector. The field flattener has a cylindrical surface on its rear surface to mitigate the cylindrical field curvature arising from the cross-dispersion. The camera focal length was chosen to give at least two pixel sampling of a 60k resolution element. Fig.2.7 shows the spectral format of the designed spectrograph. The last element of the camera, the field flattener, along with the detector is tilted by 4.9 degrees to reduce the ghost from the CCD surface.

The intermediate slit mirror is used for focusing the system. The Slit mirror is mounted on linear translation stage. Axial displacement of the slit mirror results in some blurring as well as motion of the spectral image on the detector in the cross-dispersion direction. Fig. 2.8 shows the nominal focus setting with sliced and un-sliced images of the fibre as seen by the detector for a central wavelength (491.6 nm) along with images in which the slit mirror has been moved by +1 and -1 mm. The combined image of the flat field exposures taken at these three slit-mirror position is used to obtain a broadened flat profile for flat field correction of the science exposure.

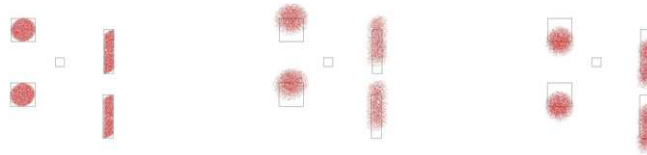


Figure 2.8: Spot diagram of slit image for sliced and unsliced modes on CCD at the central wavelength for three different positions of slit mirror. Right: at the focus, Centre and left: slit mirror moved 1mm away from focus in the two directions respectively



Figure 2.9: Hanle Echelle Spectrograph aligned and tested at the Kiwistar Optics Facility (Image credit : Callaghan Innovation)

The complete system is built and tested in the Kiwistar Optics facility. Fig.6.9 shows the image of the assembled system. Instrument will be installed at the observatory in the month of September, 2015.

Chapter 3

Model Based Calibration

3.1 Introduction

In this chapter, a brief description of the model based calibration technique and the theoretical formulation of the model is presented. The purpose of a model based calibration is to develop a physical model of an instrument that represents the actual working of the instrument during real observation/experiment. This model is later used for accurate calibrations of the data and also to understand the behaviour of the instrument. A physical model is built from the physics of the instrument design and built-up rather than an empirical fitting of the calibration data [6]. This method also gives a physically meaningful predictive power in regions where there are no calibration data available, rather than a simple extrapolation of an empirical fit. The construction of a model can be optimised to meet the science requirement of the data that is taken. In this work we start with the construction of a model that will give a precise and accurate wavelength calibration. For a given position on the slit, the model should predict the corresponding position on the CCD at a particular wavelength. Relevant components and subsystems will be modelled individually according to their physics. Chief Ray of a

given wavelength at a given position on the slit will be traced through each component to the position on the CCD.

An initial model uses the design parameters of the instrument, these are the distances and relative positions and tilts of the optical components. Most of these parameters may not match exactly with the built instrument causing a difference in the spectral positions between the predictions and the actual data. So, before using the model for calibrating the data, it is necessary to estimate an accurate value for these parameters. Calibration data along with an optimization routine will be used to derive these parameters, using an appropriate merit function, which is sensitive to the centroid locations of spectral features. Simulated annealing optimization routine is used to optimize the parameters in the model such that the merit function is minimized.

In this chapter, we discuss the process to construct a physical model. Optimizing the model and matching with the instrument will be discussed in Chapter 4. A model is expected to make accurate predictions and yet the modules need to be simple encompassing the physical parameters required to optimize and with careful attention to the degenerate states. The scheme presented here is simple to implement in a spread sheet or any simple scripting language. The computations are based on paraxial ray trace and exact corrections added for certain surface types and Buchdahl aberration coefficients for complex modules [10]. The resultant chain of paraxial ray traces and corrections for all relevant components is used to calculate the location of any spectral line on the detector under all normal operating conditions with a high degree of certainty. This will allow a semi-autonomous control using simple in-house, programming modules giving a freedom from the commercial ray trace softwares.

An Object oriented approach is used to model the system making it possible to adapt this implementation for other spectrographs with a few changes. Every relevant component of the system is described in a class, the parameters of the component as its attributes and the transformation functions as

the methods of the class. Ray tracing is done between these components. The final instrument model will be described later in detail. Fig. 3.1 shows an example of the class diagram of one of the components, the prism. Any transformation function will have as input the ray coordinates (described in section 3.2) of the incoming ray and output is the emergent ray coordinates from that particular component. HESP model formulation will be described in the following sections.

Different Modules relevant to HESP are:

- Slit
- Collimator
- Echelle Grating
- Prism
- Camera
- CCD Detector

3.2 Coordinate system and Ray coordinates

Fig. 3.2 shows the coordinate system used for the model. Looking from the positive axes, clockwise direction is defined positive. An optical component is placed with its optic axis along the Z-direction. Distances between the components are the z-distances. A paraxial plane of any optical component is in the XY plane. Positive tilts of the surfaces or group of surfaces are defined by rotation of the axes as shown in Fig. 3.2

A Ray (OP) is defined by its coordinates (x, y, z) at the point of its intersection on a surface, cosine of angles (α, β, γ) it makes with the x, y and z axes, (DCx, DCy, DCz) respectively and the wavelength of the ray, λ .

In the following section different HESP components' classes will be defined and the relevant formulation theory will also be presented.

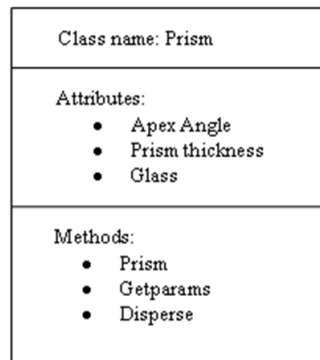


Figure 3.1: Class diagram of prism

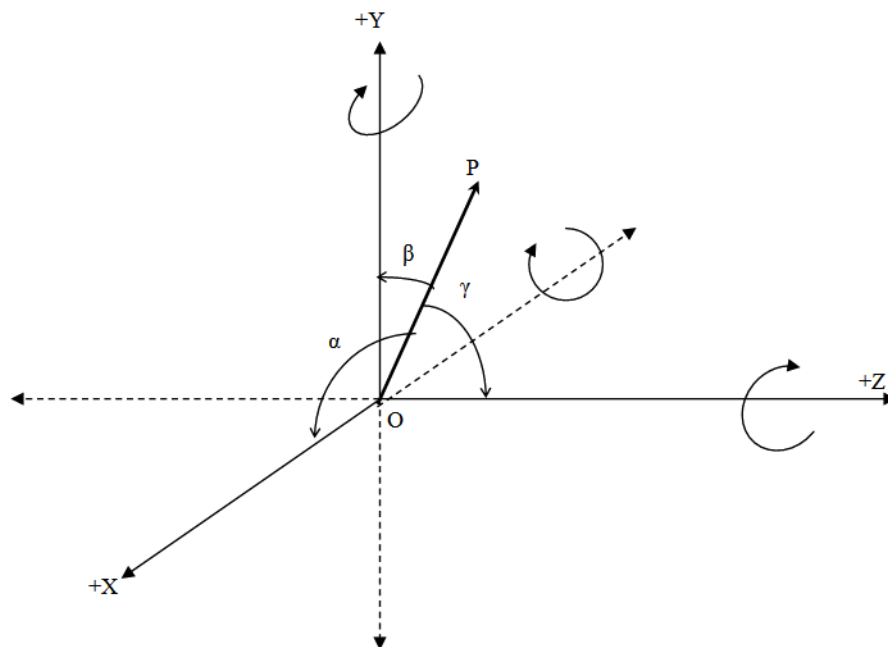


Figure 3.2: Coordinate system Definition

3.3 Class Definitions

3.3.1 Slit

Slit plane is the first component of the spectrograph placed in the XY plane. This is the plate that will be re-imaged onto the CCD after dispersion. The slit is described by its position (x, y) , slit width and height.

3.3.2 Collimator

HESP collimator which is used in triple pass is a parabolic mirror as described in Chapter 2. The mirror is defined by its curvature and the conic constant. The inputs to the transformation function are the ray coordinates at the paraxial plane of the collimator, OP (Fig. 3.3). The curvature (c) and conic constant (k) are used to establish the sag equation of the mirror surface. Sag dz is given by

$$dz = \frac{(c_x x^2 + c_y y^2)}{1 + \sqrt{1 - (1 + k_x)c_x^2 x^2 - (1 + k_y)c_y^2 y^2}} \quad (3.1)$$

(c_x, c_y) are the curvatures in x and y. (k_x, k_y) are the conic constants in x and y. A ray AP with direction cosines (DC_x, DC_y, DC_z) intersects the collimator mirror at A and the paraxial surface of the mirror at P. While the ray coordinates at P are the input to the transformation function, the output ray coordinates at A are to be computed. From the Fig. 3.3, the distance $d\eta$ for a parabolic mirror is derived as

$$d\eta = \frac{-(x_p dT_x + y_p dT_y) - \frac{r1}{2} - \left[\frac{r1}{|r1|} \sqrt{\left(\frac{r1}{2}\right)^2 - r1x_p dT_x - r1y_p dT_y - (y_p dT_x - x_p dT_y)^2} \right]}{dT_x^2 + dT_y^2} \quad (3.2)$$

Where, (X_p, Y_p) = ray intersect coordinates on the paraxial collimator plane (dT_x, dT_y) = Direction tangents of the ray $r1$ = twice the radius of curvature of sag $d\eta = z$ distance from the paraxial plane to A

The coordinates of the ray intersection A (x_{new}, y_{new}) on the mirror surface are given by

$$\begin{aligned} x_{new} &= x_p - d\eta \times dT_x, \\ y_{new} &= y_p - d\eta \times dT_y \end{aligned} \quad (3.3)$$

The direction cosines of the reflected ray at this point can be calculated from the reflection equation at a surface,

$$dc_{new} = dc_{old} - 2\cos\theta normal \quad (3.4)$$

Where, dC_{new} , dC_{old} are the direction cosines of the ray after and before reflection θ is the angle between the ray and normal at the point (X_{new}, Y_{new})

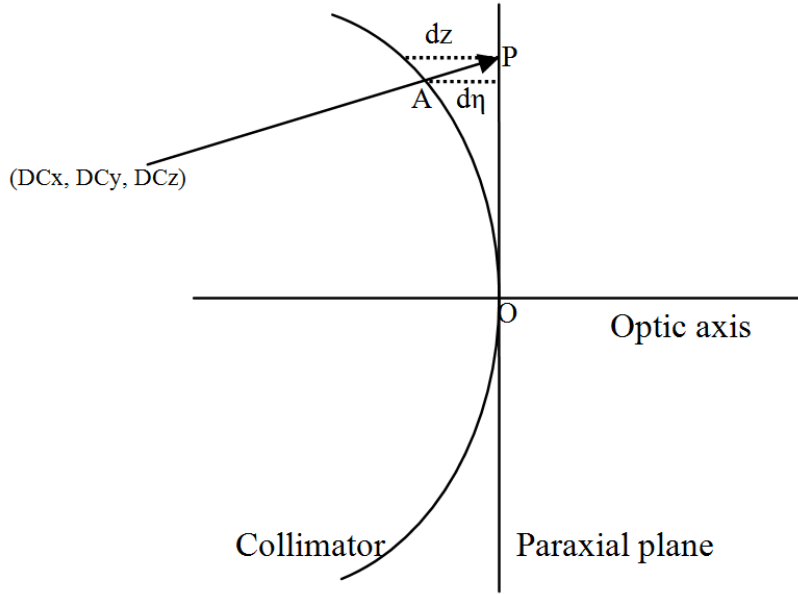


Figure 3.3: Two dimensional depiction of the collimator mirror

3.3.3 Grating

The high dispersion element in the spectrograph is an Echelle grating. For the grating the class attributes are, the grating constant and the direction of the grooves. The transformation function in calculating the direction of the diffracted ray vector uses the prescription by Mitchell [34]. For a plane grating an easier formulation by Schroeder 1987 will work, however we also describe the generalized ray tracing diffraction grating (Mitchell 1981) to use for any sort of gratings since we intend to develop a model that is generalised for any high resolution spectrograph.

For the first simpler formulation for a planar grating, we follow Schroeder

[46]. Considering the grating in the XY plane, if the angle the ray makes with the XZ plane be ξ , and the angle it makes with the Z-axis is ψ , then

$$\begin{aligned} DC_x &= \sin\psi\cos\xi \\ DC_y &= \sin\xi \\ DC_z &= \cos\psi\sin\xi \end{aligned} \quad (3.5)$$

General grating equation is given by

$$\begin{aligned} \frac{m\lambda}{d} &= n' \cos \xi' \sin \psi' - n \cos \xi \sin \psi \\ n \sin \xi &= n' \sin \xi' \end{aligned} \quad (3.6)$$

Where (ξ, ψ) are the direction coordinates of the incident ray (ξ', ψ') are the direction coordinates of the diffracted ray. For a reflection grating,

$$\begin{aligned} n &= n' \\ \xi &= -\xi' \end{aligned} \quad (3.7)$$

That is,

$$\frac{m\lambda}{d} = -n \cos \xi (\sin \psi' + \sin \psi) \quad (3.8)$$

Converting relation in terms of direction cosines, the relation between output and input direction cosines will be

$$\begin{aligned} n' DC'_x &= \frac{m\lambda}{d} + n DC_x \\ n' DC'_y &= n DC_y \\ DC'_z &= \sqrt{1 - DC_x'^2 - DC_y'^2} \end{aligned} \quad (3.9)$$

Where (DC_x, DC_y, DC_z) and $(DC_{x'}, DC_{y'}, DC_{z'})$ are the direction cosines of the incident and diffracted rays respectively.

Generalized ray tracing for diffraction grating: Mitchell 1981 has determined the direction vector of a diffracted ray. Four surfaces S_0, S_1, S_2 and S_3

are defined,

S_0 = Surface of the grating

S_1 = Incident wavefront

S_2 = Diffracted wavefront

S_3 = One of the families of surfaces which determine the geometrical characteristics of grating.

For regular planar grating, this is a family equally spaced of parallel surfaces

If \mathbf{n}_0 , \mathbf{n}_1 and \mathbf{n}_3 are the unit vectors normal to the surface S_0 , S_1 , and S_3 respectively, n and n' are the refractive indices of the media in the incident and emergent sides of the grating and d is the local value of normal separation of the surfaces of which S_3 is a member (when these surfaces meet the surface S_0 normally as is the case with the plane gratings, d is the grating period), then the normal to S_2 , \mathbf{n}_2 is to be calculated. We can express \mathbf{n}_2 as linear combination of other vectors.

$$\mathbf{n}_2 = A\mathbf{n}_0 + B\mathbf{n}_1 + C\mathbf{n}_3 \quad (3.10)$$

where,

$$A = -B\mathbf{n}_0 \cdot \mathbf{n}_1 - C\mathbf{n}_3 \cdot \mathbf{n}_0 \\ \pm \sqrt{B^2[(\mathbf{n}_0 \cdot \mathbf{n}_1)^2 - 1] + C^2[(\mathbf{n}_3 \cdot \mathbf{n}_0)^2 - 1] + 2BC[(\mathbf{n}_0 \cdot \mathbf{n}_1)(\mathbf{n}_3 \cdot \mathbf{n}_0) - (\mathbf{n}_1 \cdot \mathbf{n}_3)] + 1}$$

$$B = \frac{n}{n'} \\ C = -\frac{m\lambda}{n'd} \quad (3.11)$$

3.3.4 Prism

In HESP, two prisms are used together for cross-dispersing the orders. So, prism is defined as, one of the component classes. The attributes for prism are apex angle, dispersion function of the glass $n(\lambda, T)$ and its base thickness.

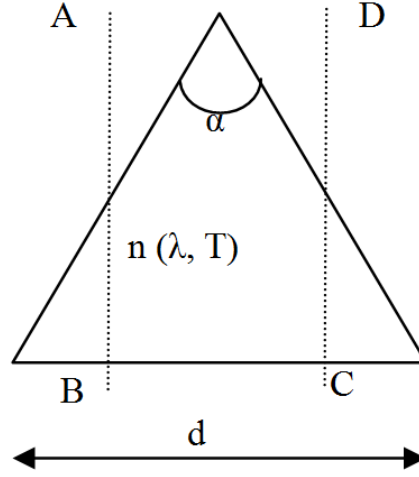


Figure 3.4: Prism description. The ray coordinates on surface AB are the input to the prism transformation function. The output of the function are the ray coordinates on CD

The transformation function is the 3D refraction at the surfaces and ray trace within the prism. Inputs to the prism transformation function are the coordinates of the ray intercept on the plane AB shown in Fig. 3.4 and the wavelength of the ray. The output of the transformation function is the coordinates of the ray on CD in Fig. 3.4. From the ray coordinates on AB, and the apex angle of the prism, the ray coordinates on the first surface of the prism can be calculated. At the surface 3D refraction equation will give the coordinates of the refracted ray in the prism. The 3D refraction at a surface is given by

$$dc_{new} = \frac{n_1}{n_2} dc_{old} + \left(\cos r - \frac{n_1}{n_2} \cos i \right) normal \quad (3.12)$$

Where,

dc_{new}, dc_{old} = direction vector of the ray after and before refraction

n_1, n_2 = refractive indices of medium before and after the refractive surface
 $(n(\lambda, T))$

i, r = Angle made by incident ray and refracted ray with normal to the surface at the point of intersection of ray with the surface

The refracted ray will be traced from the first surface to the second surface

of the prism, again using the 3D refraction, which will give the ray coordinates of the output ray. Using the coordinates of the ray on the surface and the apex angle of the prism, ray coordinates on CD can be calculated. The ray trace equations will be discussed in the 3.3.5 subsection.

3.3.5 Camera

Camera, in general a multi-element system, is designed to correct the various aberrations introduced by the spectrograph optics. HESP camera is a five element system, CM1 to FF in Fig.2.5. The first four elements are rotationally symmetric whereas the fifth element is a field flattener, with one cylindrical face and placed at an angle with respect to the first four elements to eliminate the ghost imaging from the CCD. A regular ray trace from surface to surface in a camera system will need a number of square roots and trigonometric calculations. Besides the surface to surface ray propagation, at each surface following calculations need to be done:

1. Exact point where the ray intersect the surface
2. Normal to the surface at the intersection point
3. Refractive index of the new medium
4. Refraction equation solution to calculate the refracted ray coordinates

This will also increase the number of parameters in the model In order to achieve an accurate camera model with reasonable number of parameters defining the camera system, following methodology is adapted. The first four elements are modelled as a single unit. The unit is described by its ABCD matrix and aberration polynomial coefficients. The output from this unit is traced through the single element field flattener for the best accuracy at the detector plane.

In the following subsection a quick overview of ABCD coefficients formalism is presented, followed by the corrections for the aberrations. Given the

wide coverage of the wavelengths from 350 to 1000 nm of the spectrograph, it is also very important to include the chromatic corrections. We will also show how this aspect is being addressed in the current work.

3.3.5.1 ABCD Matrices: Paraxial Coefficients of Lens systems

We describe here the prescription by Cruickshank et al. [15], in obtaining the paraxial coefficients. Fig.3.6 shows refraction of a ray QP at a spherical surface. A ray QP inclined at an angle U with respect to the optic axis AC, that intersects the spherical surface at point P. The spherical surface separates the two media of refractive indices N and N' , it has a curvature c , with vertex at A and optic axis AC. The ray QP has an angle I with respect to the normal of the surface at P, which is a line joining P and the centre of curvature, C. The refracted ray PB' makes an angle I' with the normal to the surface at P and an angle U' with the optic axis, AC. The incident and refracted rays can be defined by their height at the surface, Y and their inclination U and U' respectively. U and U' are defined positive or negative according to the direction of rotation from axis to the ray being clockwise or anticlockwise respectively. Radius, r of the surface is defined positive or negative according to the curvature of surface is to right or left to A. Similarly angles I and I' are considered positive or negative according as clockwise or anticlockwise rotation of ray QP, PB' takes them to the normal at the point on the surface.

Given these, considering the geometry and the Snell's law it can be shown that,

$$\begin{aligned} Y &= r \sin(U + I) \\ N \sin I &= N' \sin I' \\ U + I &= U' + I' \end{aligned} \tag{3.13}$$

If the ray proceeds to next surface as shown in Fig.3.6, where D'_1 is the

distance along the ray from P_1 to P_2 . Then it can be shown that,

$$\begin{aligned} U_2 &= U_1' \\ Y_2 &= Y_1 - D_1' \sin U_1' \end{aligned} \tag{3.14}$$

Above are the transfer equations which will be used throughout the model to trace ray from component to component or surface to surface.

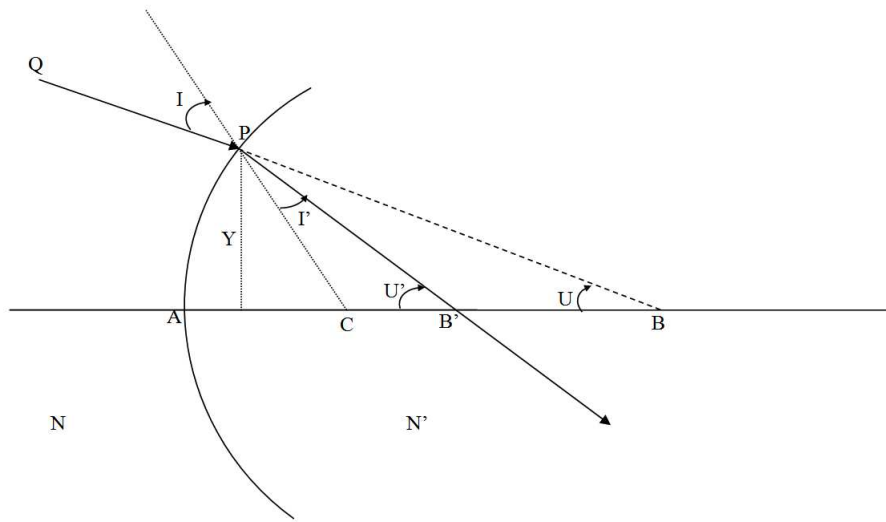


Figure 3.5: Refraction at a spherical surface

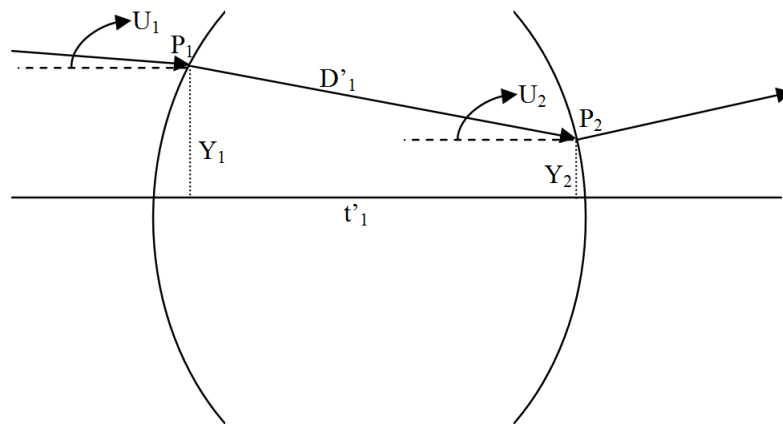


Figure 3.6: Illustration of transfer equations between two surfaces

For small angles $\sin \alpha \approx \alpha$, and Equations 3.2.5.1 and 3.2.5.2 becomes,

$$\begin{aligned}
y &= r(v + i) \\
i' &= ki; k = N/N' \\
v + i &= v' + i' \\
v_2 &= v'_1 \\
y_2 &= y_1 - t'_1 v'_1
\end{aligned} \tag{3.15}$$

where v, v' are the paraxial equivalents of U and U' respectively. From the equation 3.15, following can be deduced, which forms the paraxial refraction equation at the spherical surface,

$$\begin{aligned}
v' &= kv + \Phi y \\
\Phi &= (1 - k)c \\
c &= 1/r
\end{aligned} \tag{3.16}$$

When tracing rays through a system of spherical surfaces, a set of paraxial coefficients can be derived to represent the complete system. If we can write the paraxial equation for surface 1 (Fig.3.7) as

$$\begin{aligned}
v'_1 &= k_1 v_1 + \Phi_1 y_1 \\
v'_2 &= k_2 v_2 + \Phi_2 y_2; \text{ for surface 2.}
\end{aligned} \tag{3.17}$$

We know $v_2 = v'_1$ and $y_2 = y_1 - t'_1 v'_1$, which can be simplified and written as

$$\begin{aligned}
y_2 &= A_2 y_1 + B_2 v_1 \\
v'_1 &= C_2 y_1 + D_2 v_1
\end{aligned} \tag{3.18}$$

This can be continuous over all the surface of the system as,

$$\begin{aligned}
y_k &= A_k y_1 + B_k v_1 \\
v'_k &= C_k y_1 + D_k v_1
\end{aligned} \tag{3.19}$$

That is paraxial ray coordinates on any surface of the system can be

written in terms of the coordinates on the first surface. A_k, B_k, C_k and D_k are called the paraxial coefficients of the system. It can also be shown that the coefficients at any surface can be calculated recursively from the following relations.

$$\begin{aligned}
 A_{j+1} &= A_j - t'_j C_j \\
 B_{j+1} &= B_j - t'_j D_j \\
 C_{j+1} &= k_{j+1} C_j + \Phi_{j+1} A_{j+1} \\
 D_{j+1} &= k_{j+1} D_j + \Phi_{j+1} B_{j+1} \\
 A_1 &= 1, \quad B_1 = 0, \quad C_1 = \Phi, \quad D_1 = k_1
 \end{aligned} \tag{3.20}$$

Once the object plane, pupil plane and the system description are available, tracing a marginal ray from an on-axis object point and chief ray from an off axis point, the Gaussian image plane and exit pupil positions can be determined. So the paraxial coordinates of a ray at the Gaussian image plane for a system can be calculated just by the incident ray coordinates and coefficients are calculated from the radii, thickness and refractive indices of the system without the intermediate calculations every time.

3.3.5.2 Aberration Polynomials

Using ABCD matrices the Gaussian image position can be calculated. But a real optical system doesn't perform ideal imaging. In real situation all rays emerging from a single point source do not converge to single image. The difference between the ideal image position and the real ray intersection point on the Gaussian image plane is called the transverse aberrations, that needs to be established for the camera system to know the ray output coordinates to a high accuracy. Theory of aberration is covered in many works (Born et al 1999, Cruickshank et al. 1960). So instead of presenting the elaborate theory, we present in brief the aspects that is relevant in this work.

Fig. 3.7 is a paraxial representation of an axially symmetric optical sys-

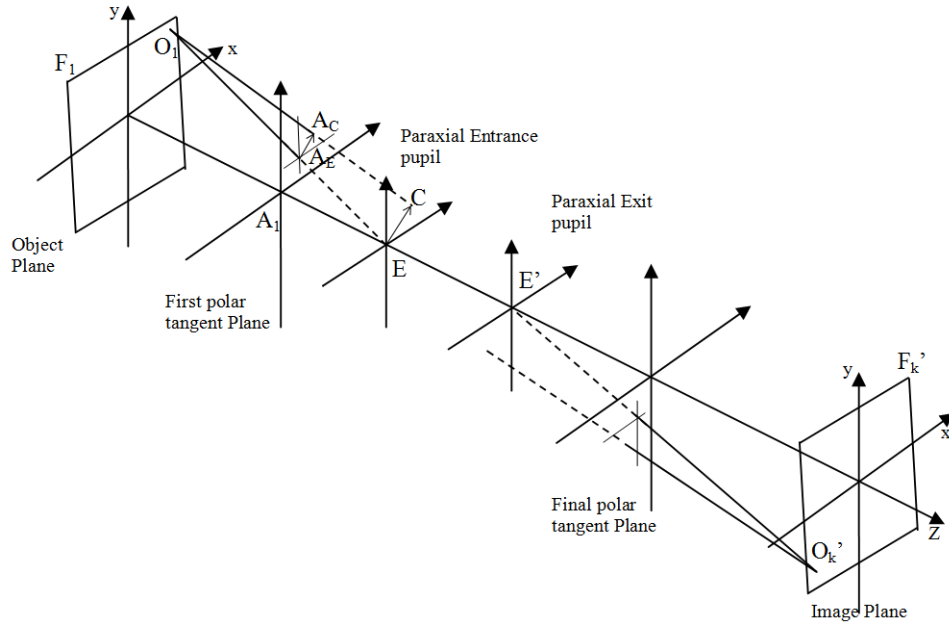


Figure 3.7: Paraxial representation of an axially symmetric Optical system

tem. F_1 is an object plane normal to the optic axis, also the axis of symmetry of the system which is the z -axis. Object plane is at a distance l_{o1} from the first surface of the system whose vertex is at A_1 . If A_k is the pole of the last surface of the system, the conjugate paraxial image plane F'_k parallel to F_1 is at a distance l'_{ok} from A_k . The axes are defined to be left handed coordinate system, with Y -axis lying in the tangential plane. Prime indicates conjugate plane points and quantities. If x and y coordinates of a point O_1 in the object plane are $-H_{x1}$ and $-H_{y1}$ respectively, all the rays from O_1 will intersect F'_k , the paraxial image plane, at a single point O_k with coordinates relative to A_k of $(-h'_{xk}, -h'_{yk}, l'_{ok})$ such that

$$\begin{aligned} h'_{xk} &= m'_k H_{x1} \\ h'_{yk} &= m'_k H_{y1} \end{aligned} \quad (3.21)$$

Where m_k is the paraxial magnification for this pair of conjugate planes and J is the ideal image point of O_1 . But in real imaging, a finite ray from O_1 will intersect F_k at O'_k with coordinates, $(-H_{xk}', -H_{yk}', l_{ok}')$. Then the

transverse aberration of the ray, ξ_k' are given by, (Fig. 3.8)

$$\begin{aligned}\epsilon'_{xk} &= H'_{xk} - h'_{xk} \\ \epsilon'_{yk} &= H'_{yk} - h'_{yk}\end{aligned}\tag{3.22}$$

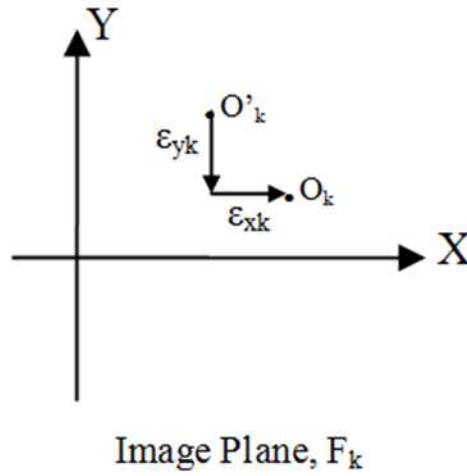


Figure 3.8: Aberration terms illustrated

The paraxial entrance and exit pupil planes are also shown in the Fig.3.7. Optic axis goes through these planes at E and E' respectively. A principal ray is defined as a ray from O_1 directed at E. A ray O_1A_cC is one of the infinite numbers of rays from O_1 that defines a cone of rays such that the point C traces a circle of radius RE on the entrance pupil plane.

It can be seen that this circle also traces another circle on the first polar tangent plane with radius, say, R and

$$R = \frac{R_E}{1 - \frac{p}{l_{01}}}\tag{3.23}$$

p is the distance between the first polar tangent plane and entrance pupil. Points on these planes can be described in the polar coordinates, (R, θ) . Therefore any ray from the object plane of a can be described by the point

of origin on object plane and point where it strike the pupil plane in polar coordinates. Given the rotational symmetry of the system, the coordinates can be rewritten in rotationally invariant variables- radial height of the object point and polar coordinates in the pupil plane with θ ($\theta_{O1}-\theta_E$) being the angle between two radial vectors of the ray's striking points in object and pupil plane as shown in Fig. 3.9.

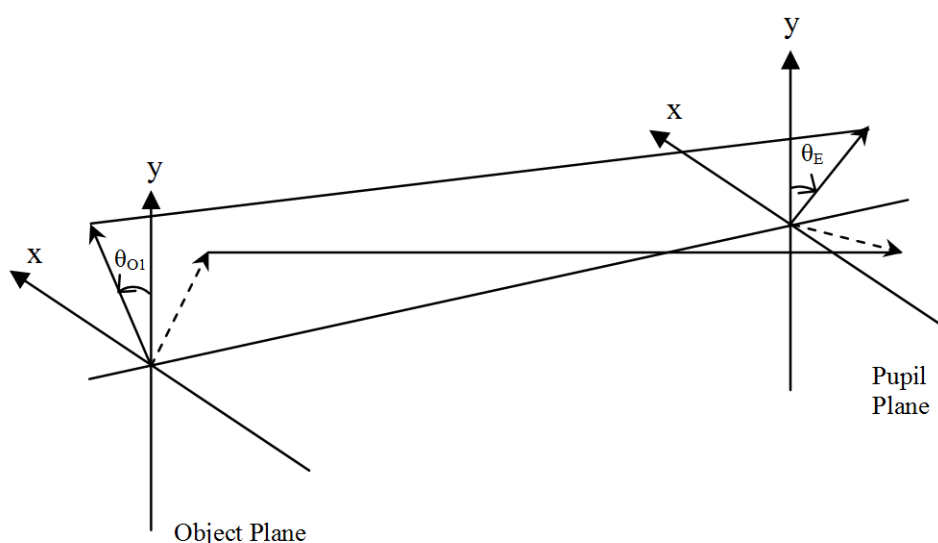


Figure 3.9: Rotational Invariance of a rotationally symmetric optical system [20]

Without loss of generality, we can choose object point on the Y-axis [4, 20]. But when the object is at infinity special case occurs. In order to overcome this tangent of angle of inclination of the principle ray is considered instead of the object point,

$$H_b = \frac{H_{yl}}{l_{01}} \quad (3.24)$$

Buchdahl, has shown that aberration the aberration term ξ_k of a monochromatic light ray can be expanded in series of ascending powers of these ray coordinates [9]. The terms of the series consists of homogeneous polynomials of degree 3, 5, 7, 9... (2n+1). The coefficients to these terms are referred to as 3rd order, 5th order, 7th order etc aberration coefficients of the optical

system. That is

$$\epsilon'_k = \epsilon_k^{(3)} + \epsilon_k^{(5)} + \epsilon_k^{(7)} + \epsilon_k^{(9)} + \dots \quad (3.25)$$

In terms of the coordinates R , θ and H_b , the third order polynomial can be written as,

$$\epsilon_{xk}^{(3)} = \sigma_1 R^3 \sin \theta + \sigma_2 R^2 H_b \sin 2\theta + (\sigma_3 + \sigma_4) R H_b^2 \sin \theta \quad (3.26)$$

$$\epsilon_{yk}^{(3)} = \sigma_1 R^3 \cos \theta + \sigma_2 R^2 H_b (2 + \cos 2\theta) + (3\sigma_3 + \sigma_4) R H_b^2 \cos \theta + \sigma_5 H_b^3 \quad (3.27)$$

σ_1 to σ_5 are the third order coefficients of spherical aberration, circular coma, astigmatism, field curvature, and distortion respectively and are often referred to as Siedel aberrations. Similarly the 5th terms can be written as

$$\begin{aligned} \epsilon_{xk}^{(5)} = & \mu_1 R^5 \sin \theta + \mu_3 R^4 H_b \sin 2\theta + (\mu_5 + \mu_6 \cos^2 \theta) R^3 H_b^2 \sin \theta \dots \\ & \dots + \mu_9 R^2 H_b^3 \sin 2\theta + \mu_{11} R H_b^4 \sin \theta \end{aligned} \quad (3.28)$$

$$\begin{aligned} \epsilon_{yk}^{(5)} = & \mu_1 R^5 \cos \theta + (\mu_2 + \mu_3 \cos 2\theta) R^4 H_b + (\mu_4 + \mu_6 \cos^2 \theta) R^3 H_b^2 \cos \theta \dots \\ & \dots + (\mu_7 + \mu_8 \cos 2\theta) R^2 H_b^3 + \mu_{10} R H_b^4 \cos \theta + \mu_{12} R H_b^5 \end{aligned} \quad (3.29)$$

where μ_1 to μ_{12} are the 5th order aberration coefficients.

7th order terms are,

$$\begin{aligned}
\epsilon'_{xk}{}^{(7)} = & \tau_1 R^7 \sin \theta + \tau_3 R^6 H_b \sin 2\theta + (\tau_5 + \tau_6 \cos^2 \theta) R^5 H_b^2 \sin \theta \dots \\
& \dots + (\tau_9 \sin 2\theta + \tau_{10} \sin 4\theta) R^4 H_b^3 + (\tau_{13} + \tau_{14} \cos^2 \theta) R^3 H_b^4 \dots \quad (3.30) \\
& \dots + \tau_{17} R^2 H_b^5 \sin 2\theta + \tau_{19} R H_b^6 \sin \theta
\end{aligned}$$

$$\begin{aligned}
\epsilon'_{yk}{}^{(7)} = & \tau_1 R^7 \cos \theta + (\tau_2 + \tau_3 \cos 2\theta) R^6 H_b + (\tau_4 + \tau_6 \cos^2 \theta) R^5 H_b^2 \cos \theta \dots \\
& \dots + (\tau_7 + \tau_8 \cos 2\theta + \tau_{10} \cos 4\theta) R^4 H_b^3 + (\tau_{11} + \tau_{12} \cos^2 \theta) R^3 H_b^4 \cos \theta \dots \\
& \dots + (\tau_{15} + \tau_{16} \cos 2\theta) R^2 H_b^5 + \tau_{18} R H_b^6 + \tau_{20} H_b^7 \quad (3.31)
\end{aligned}$$

where τ_1 to τ_{20} are the 7th order aberration coefficients. The advantage of using these coefficients is these can be calculated from the system physical parameters- surface dimensions, thicknesses, and glasses' refractive indices.

3.3.5.3 Calculating Aberration Coefficients of a rotationally symmetric system

Buchdahl has shown that the coefficients of any order can be calculated by paraxial ray trace of two rays,

- a. ray- marginal ray of on-axis object point and
- b. ray- chief ray from the maximum radial field point.

He also showed that successive order coefficients can be derived from the previous order coefficients in an iterative method [9]. The same methodology is used to calculate the coefficients given the rotationally symmetric camera optics description. This subsection presents briefly the computations.

Buchdahl has taken five chapters in his book Optical Aberration Coefficients, 1958 to present the formalism. It is not possible to concise it all into a subsection. We suggest the reader go through the book for the formalism. The system's optic axis is along x-axis in Buchdahl's work where as in our

work the optic axis is along the Z-axis and the system is left-handed in both cases.

The computations are carried out for system scaled to unit power. For systems in air this gives an advantage by reducing some factors to unity like $N'v'_{ok}$ [15]. The basic elements of the computations are

- a-ray: A ray traced from the axial object point O0 (0, 0, l_{O1}) with paraxial coordinates at the object plane $y_a = 1, v_a = 1/l_{O1}$.
- b-ray: Paraxial principle ray from the object plane such that $H_b = 1$, i.e. from the point O(0, $-l_{O1}, l_{O1}$) in the object plane aimed at axial point E on the entrance pupil.

The paraxial coordinates of the ray at the object plane are $y_b = \frac{p}{\left(1 - \frac{p}{l_{O1}}\right)}$ and $v_b = \frac{1}{\left(1 - \frac{p}{l_{O1}}\right)}$. Where p is the distance of the entrance pupil from the first polar tangent surface of the system. The computations start with these rays' trace through the system. Different terms are defined at each surface of the system named $t_1, t_2, t_3, t_4, \dots$.

Following are the initial few steps of the calculations, a-ray's coordinates at i_{th} surface is given by,

$$\begin{aligned}
 y_a(i) &= y_a(i-1) - t(i) \times v_a(i) \\
 I_a(i) &= c(i) \times y_a - v_a(i) \\
 I_{pa}(i) &= k(i) \times I_a(i) \\
 v_a(i+1) &= c(i) \times y_a - I_{pa}(i)
 \end{aligned} \tag{3.32}$$

Where $y_a(0) = 1, v_a(0) = 1/l_{O1}$. and coordinates of the b-ray at i_{th} surface are given by,

$$\begin{aligned}
y_b(i) &= y_b(i-1) - t(i) \times v_b(i) \\
I_b(i) &= c(i) \times y_b - v_b(i) \\
I_{pb}(i) &= k(i) \times I_b(i) \\
v_b(i+1) &= c(i) \times y_b - I_{pb}(i)
\end{aligned} \tag{3.33}$$

where,

$$y_b(0) = p / \left[1 - \frac{p}{l_{01}} \right], \quad \text{and} \quad v_b(0) = 1 / \left[1 - \frac{p}{l_{01}} \right] \tag{3.34}$$

c – Surface curvature of the system scaled to unit power, N – Refractive index, $k(i) = N(i)/N(i+1)$, $t(i)$ – thickness between i^{th} and $(i+1)^{th}$ surfaces. Some of the terms defined at the i^{th} surface are:

$$\begin{aligned}
Q(i) &= \frac{I_b(i)}{I_a(i)} \\
T_1(i) &= y_a(i) \\
T_2(i) &= v_a(i) \\
T_3(i) &= I_a(i) \\
T_4(i) &= y_b(i) \\
T_5(i) &= v_b(i) \\
T_6(i) &= Q(i) \\
T_7(i) &= -T_2(i) \times T_6(i) + T_5(i) \\
T_8(i) &= (k(i) - 1)c(i)/N(i) \\
T_9(i) &= T_2^2(i) \\
T_{10}(i) &= 0.5(v_a(i+1) - T_3)N(i) \times T_1(i) \times T_3^2(i) \times T_8(i)/T_7(i) \\
T_{11}(i) &= T_6(i) \times T_{10}(i) \\
T_{12}(i) &= 2T_6(i) \times T_{11}(i) \\
T_{13}(i) &= 0.5(T_{12}(i) - T_8(i)) \\
T_{14}(i) &= T_6(i) \times T_{13}(i)
\end{aligned} \tag{3.35}$$

The tertiary aberration coefficient contribution from the i_{th} surface is

$$\begin{aligned}
\sigma_{1i} &= T_{10}(i) \\
\sigma_{2i} &= T_{11}(i) \\
\sigma_{3i} &= T_{12}(i)/2 \\
\sigma_{4i} &= -T_8(i)/2 \\
\sigma_{5i} &= T_{14}(i)
\end{aligned} \tag{3.36}$$

The related terms and the coefficients of 5th and 7th order aberrations are detailed in reference [11]. The aberration coefficients of the complete system of k-surfaces is given by

$$\sigma_j = \sum_{i=1}^k \sigma_{ji} \quad (3.37)$$

where, $j = 1, 2, 3, 4$ or 5 .

$$\mu_j = \sum_{i=1}^k \mu_{ji} \quad (3.38)$$

where, j represents any of the 1 to 12 of the 5th order aberration terms.

$$\tau_j = \sum_{i=1}^k \tau_{ji} \quad (3.39)$$

where, j represents any of the 1 to 20 of the 7th order aberration terms.

3.3.5.4 HESP Camera Implementation:

The HESP camera is a five element system, with first four rotationally symmetric elements and the final field flattener with a cylindrical surface. The first four elements are modelled as a single unit described in the above section (from now on this will be referred to as camera-1). The output from the camera-1 is traced through the field flattener to the detector plane. In order to trace rays through the field flattener, the complete ray coordinates with the direction components are required. Above subsections describe the methodology to determine the rays' intersection points on the Gaussian image plane of a system.

In order to determine the complete ray coordinates out of camera-1, we model the camera-1 in two configurations. Fig. 3.10 shows the two configurations. The idea behind this implementation is determining the ray's intersection points on two different planes at the output side of Camera1, from which the direction cosines of the ray can be calculated. In Fig. 3.10(a), the camera is viewed as an imaging system with object plane at the entrance pupil of the camera optics in the complete spectrograph, which is also the pupil plane of the spectrograph. The entrance pupil of this system is at the

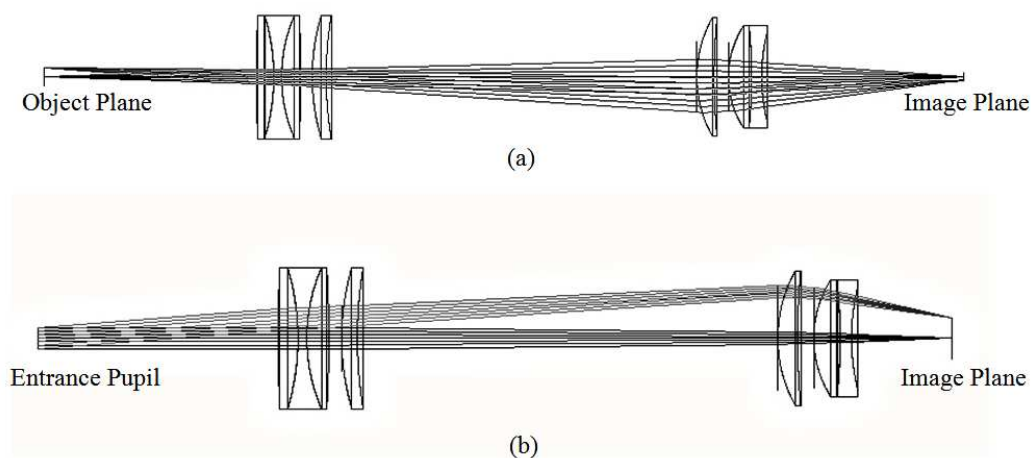


Figure 3.10: Camera configuration with object plane at the camera system's entrance pupil in the spectrograph (b) Camera configuration with object plane at infinity

first surface of the first element of Camera1. In Fig. 3.10(b), the camera is viewed as an imaging system for an object plane at infinity and entrance pupil at the spectrograph's pupil plane. Surfaces shown as Image plane in both Fig. 3.10(a) and (b) are the Gaussian planes of the respective systems.

The objective of the model is to trace the chief rays, so aperture size enough to accommodate the chief rays of the wavelengths of interest are selected rather than the physical size of the optics. This also reduces the number of aberration terms required to get accurate coordinates. Camera1 will be defined by its ABCD coefficients, the 3rd, 5th and 7th order aberration coefficients for the two configurations.

Besides reducing the number of computations in each iteration during optimization of the model to match it with the instrument, the main aim is to derive a set of parameters that describe the camera to optimize. Camera is assembled into its mount using a coordinate measuring machine (CMM), hence the spacing between the elements is highly accurate at few microns. The optics' radii of curvature and thickness are also measured to good accuracy of about 5 μm and 10 μm respectively. These may vary to a considerable amount when the system is assembled in a particular temperature but is used in a different temperature. But once the instrument becomes operational

it is maintained at constant temperature with ± 0.5 °C. Model is using the measured thicknesses and radii. Any discrepancies in these numbers will lead to a difference in ABCD and aberration coefficients. Of these, ABCD coefficients carry the most information. So the ABCD coefficients of the system are chosen as the open parameters for the system.

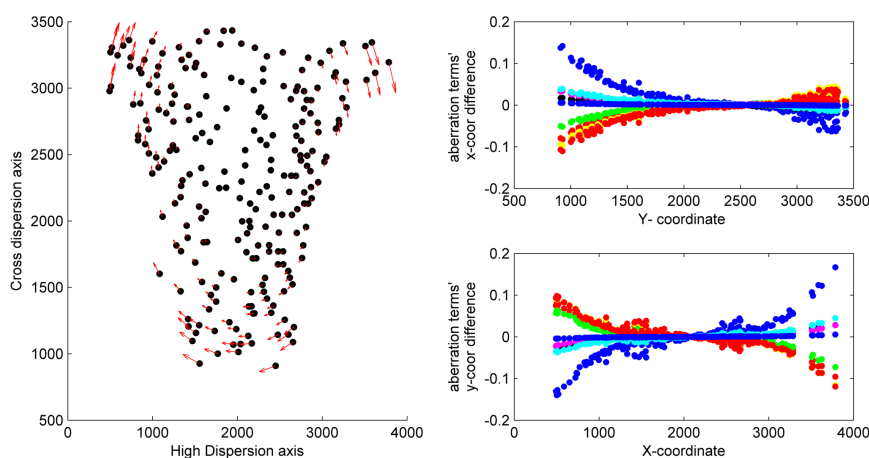


Figure 3.11: Difference in aberration terms. Left: Vector plot of differences at different points on the spectrum for one of the sets of thickness and radii. Right: top panel is the difference in aberration terms' x-coordinate, while the bottom panel is the difference in aberration terms' y-coordinate in pixel units of the points in spectrum shown in left panel for different sets of thicknesses and radii.

In order to understand the effect of change in thickness and radii on the aberration terms, few simulations were done for different radii and thicknesses in possible range of changes estimated from the thermal expansion coefficients of the materials of the camera system and a very basic FEA analysis of lenses in their mechanical cells to estimate possible variations in radius of curvatures. The difference in the aberration terms was plotted in Fig. 3.11. It can be seen that the differences follow a pattern, which can be corrected for using a polynomial in the end during the model optimization with the instrument data.

3.3.5.5 Wavelength Dependency of Coefficients

HESP covers wavelengths from 350 nm to 1000nm. The wavelength dependency of refractive index of the optics is manifested in the wavelength dependency of the different coefficients. In principle though we can calculate the different coefficients for various wavelengths, we cannot afford to have the ABCD coefficients of all the wave lengths as open parameters. The coefficients were calculated for various wavelengths and plotted, seen in Fig. 3.12.

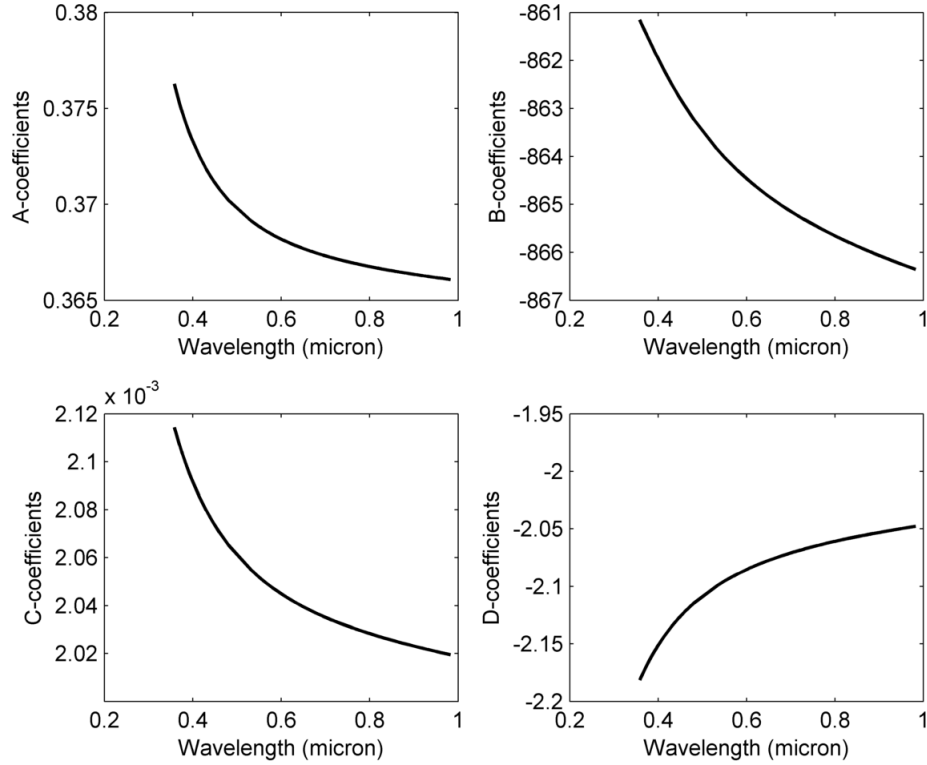


Figure 3.12: Variation of the ABCD coefficients with wavelength

The functional form,

$$\Lambda(\lambda) = \Lambda(\lambda_m) + \left(a\lambda + \frac{b}{\lambda^2} + \frac{c}{\lambda} + d \right) \quad (3.40)$$

fits the relation between the coefficients and wavelengths to a coefficient of determination, R-square of 0.9999. Here, Λ can be any of A, B, C or D. λ is wave length, λ_m is a particular selected wavelength (in general mid wave-

length of the band) a, b, c and d are coefficients of the polynomial to fit. This leaves just four parameters, $(A(\lambda_m), B(\lambda_m), C(\lambda_m) \text{ and } D(\lambda_m))$, to include in the open parameters set for final optimization of the model to match the instrument.

The output from Camera1 is the ray coordinates at the last surface of the Camera1. From this surface the ray will be traced through Field flattener lens. The lens is a singlet with a flat surface and a cylindrical surface. 3D refraction at the surface interface and ray trace within the lens is used to trace the ray through the lens similar to prism (Equations 3.12 and 3.14). Cylindrical surface radius of curvature and thickness of the lens are the inputs to this module.

Finally, the attributes to the camera class are the ABCD coefficients, the aberration coefficients and the field flattener surface radii and its thickness. The class construct function includes the calculation of the ABCD and aberration coefficients when required. The transformation function's input are the ray coordinates on the first surface of the camera and the output is the ray coordinates on the last surface of the filed flattener.

3.3.6 Detector

Detector is defined by its pixel size and the total detector dimensions. The transformation function converts the position on the image plane from distance units (mm) to pixel units.

3.4 Total System Description

The complete spectrograph is described by the components in proper order and the tilts and decentres associated with them. The chief ray trace starts with the ray description at the first component, the slit. The position on the slit, the direction cosines of the ray and the wavelength are the required starters. As we are tracing just the chief rays, the ray's direction vector is $(0,$

0, 1).

An excel sheet describing the components and the distances between them (Fig. 3.13) will be read and the ray will be traced from one component to the next using the trace equation 3.14. The different columns in the Fig. 3.13 are as follow:

1. Component Name: This defines the component
2. The distance from present component to next
3. 3rd to 5th columns: Tilts in x, y and z axis to be applied at the input surface of the component
4. 6th to 8th columns: Tilts in x, y and z axis to be applied at the output surface of the component
5. 9th to 10th columns: Decentres in x and y axis at the input surface of the component
6. 11th to 12th columns: Decentres in x and y axis at the output surface of the component
7. 13th to 14th columns: These define the order of decentring and tilts to be applied at the input and output surfaces of the component respectively

The ray coordinates are transformed for the tilts associated by multiplying with the coordinate transform matrix

$$R = R_{\mu/x}R_{\nu/y}R_{\tau/z} \quad (3.41)$$

where,

$$R_{\mu/x} = \begin{pmatrix} 0 & 0 & 1 \\ \cos \mu & \sin \mu & 0 \\ -\sin \mu & \cos \mu & 0 \end{pmatrix} \quad (3.42)$$

Component	Distance to next Component	X-tilt Before	Y-tilt Before	Z-tilt Before	X-tilt After	Y-tilt After	Z-tilt After	X-dec Before	Y-Dec Before	X-dec After	Y-Dec After	Order1	Order2
Slit	Param4	Param1	Param2	Param3	None	None	None	None	None	Param36	Param37	0	0
Collimator	Param5	Param6	param7	None	Param6-	Param7-	None	None	None	None	None	0	0
Echelle	Param5-	Param8	Param9	Param10	Param8-	Param9-	Param10-	None	None	None	None	0	0
Collimator	Param11	Param6	param7	None	Param6-	Param7-	None	None	None	None	None	0	0
SlitMirror	Param12	Param13	Param14	None	Param13-	Param14-	None	None	None	None	None	0	0
Collimator	Param13	Param6	param7	None	Param6-	Param7-	None	None	None	None	None	0	0
FoldMirror	Param14	Param15	Param16	None	Param17	Param18	None	None	None	Param38	Param39	0	0
Prism1	Param19	Param20	Param21	None	Param22	Param23	None	None	None	None	Param40	0	1
Prism2	Param23	Param24	Param25	None	Param26	Param27	None	None	Param41	None	Param42	1	0
Camera	Param28	Param29	Param30	None	None	None	None	Param43	Param44	None	None	0	0
FieldFlattener	Param29	Param30	Param31	Param32	None	None	None	Param45	Param46	None	None	1	0
CCD	END	Param33	Param34	Param35	None	None	None	Param47	Param48	None	None	1	0

Figure 3.13: Spread sheet description of the instrument

Chapter 4

Matching model with the Instrument

4.1 Introduction

Once the model is constructed, the next step is to adjust the parameters in the model to match the built instrument as described in the introduction to Chapter 3. The parameters that need to be adjusted cover various aspects of a working instrument, the measured dimensions of the manufactured optics, glass details, and the environment conditions. The optimization procedure adjusts the parameters in the model to match the calibration data taken with the instrument. We had an advantage of developing the model, while the hardware subsystems of the instrument were underway. This gave a good understanding of the built optics and opto-mechanics of the instrument.

Fig. 4.1 shows a flowchart of the entire steps involved in the case of a model based technique. The core of process is the physical model, which has an accurate mathematical formalism to represent the real instrument and a set of parameters which could change during observations and environmental conditions.

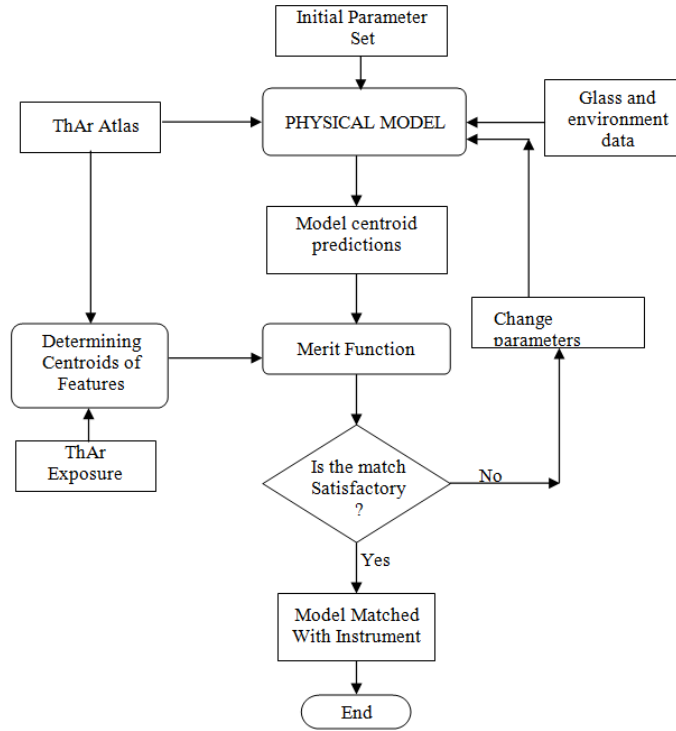


Figure 4.1: Flowchart of the model based technique (Bristow 2008).

An initial model corresponds to mapping of predefined slit position on to a final position on the CCD, for a set of accurate Thorium Argon Atlas wavelengths and a set of parameters that will be optimised. The ThAr calibration exposures that are used for the wavelength calibration of the science data will be used to match the initial model. The centroid positions of a set of good ThAr features will be measured and matched with the predicted position of the model. A merit function (generally root mean square error) is constructed to minimize the difference between the model predictions and the measured centroid values the ThAr features from the calibration frame. The model parameters will be changed until a minimum value of the merit function is reached, that determines the final parameters for which the calibration match the model. To change the input model parameter in an iterative fashion, we use a global optimizer, that will also help the merit function not to get stuck in a local minima.

In this chapter all the modules in the flow chart other than the physical

model will be discussed. We will discuss the choice of model parameters that is used for minimizing the merit function, the ThAr atlas, and decision on accurate wavelength features. We also discuss the measurement of centroid of the features in the image, environmental data, optimization routine, glass refractive indices.

4.2 Choice of model parameters for optimization

As discussed in Chapter 3, various physical parameters, which are distances between the components, tilts associated with various surfaces, decenters in the positions, form the parameter set for the model. The initial instrument model has parameters that are same as the values from the design file. A total of 45 parameters were considered in HESP model: Slit x, y and z-tilts, slit x & y decentres, slit to collimator distance, x and y tilts, Collimator to Echelle distance, Echelle x, y and z-tilts, Echelle grating constant, Collimator to slit mirror distance, Fold mirror x and y-tilt, x and y decentres for prism1, fold mirror to prism distance, prism 1 y-tilt, prism 2 decentre, prism 1 to prism 2 distance, camera x and y decentre, prism 2 to camera distance, y-tilts before and after prism2, prism1 and 2 x-tilt, camera to filed flattener distance, Filed flattener and CCD x and y decentre, x, y and z tilts of field flattener and CCD, field flattener to CCD distance, CCD x and y decentres, CCD x, y and z tilts.

Once the instrument is built, these values may vary slightly from the instrument design parameters, so it is necessary to establish the true values. This may also be the case after a major maintenance intervention, upgrade to the instrument or even an earthquake, resulting in a physical change in the instrument. Some of these crucial parameters are chosen as parameters for optimization using the calibration images, in order to match the model

with the instrument. Out of the 45 total parameters of the spectrograph 25 are used in optimization. The effect of various parameters at the detector plane for different wavelength is studied using patterns of vector maps showing the difference between the design and perturbed mapping of the spectral positions. Fig. 4.2 shows some examples of vector maps showing the differences in position of selected spectral line features when various parameters are perturbed a little. Blue Points represents the spectral features across the detector location as per the design (nominal position) and the arrow of vectors indicate drift in the features with change in parameters.

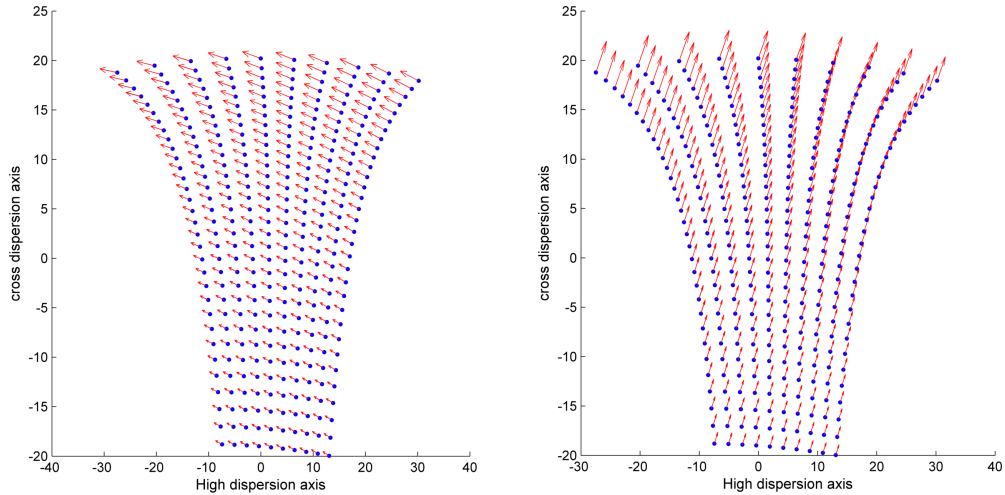


Figure 4.2: Shift in spectrum for different parameter values. Two different parameter subsets were changed a little from the nominal. The blue points show the scatter of selected wavelengths across the spectrum. Red arrows indicate the shift in these positions from the nominal when the parameter subsets are changed.

Though the final shifts are a combined effect of all the parameters, by selecting subsets of parameters, and studying the residuals, gives a better understanding of the choice parameters for optimization. For example, though the major shifts in the high dispersion and cross dispersion directions can be attributed to Echelle and fold mirror angles, the second and higher order shifts cannot be attributed to the same. An example is shown in Fig. 4.3.

A ThAr spectrum is obtained from the aligned instrument and only few of the basic parameters like the Echelle x-tilt, fold mirror y-tilt, slit decentre, collimator and prism tilts are optimized. Fig.4.3 shows the vector plots for

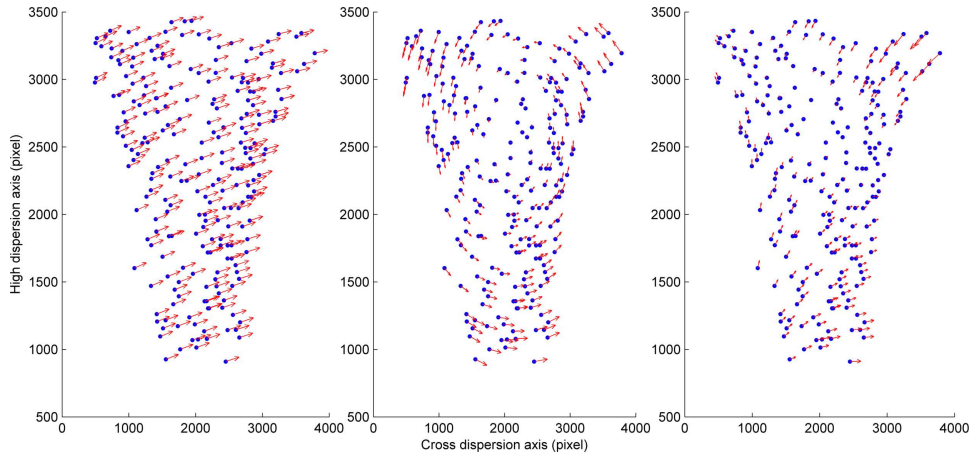


Figure 4.3: Left: Vector plot of difference of feature position from instrument and model predictions. Centre & Right: Vector plots of difference of feature positions from instrument and optimized model predictions (model optimized for two different subsets of parameters). The residual patterns are an indication of missing parameters used for optimization. The pattern itself is an indication of what parameters may be missing.

residuals before and after optimization with selected parameters. There is a possibility of some parameters compensating for others causing degenerate states. While these will be hard to resolve, they can be minimized by understanding the instrument alignment and its components manufacturing procedures. The measurements of the manufactured and aligned optical and mechanical components can correct for maximum differences, and an understanding of the operation of the instrument and the conditions in which it operates can dictate the bounds on the parameters for optimizing and hence minimising the number degeneracy states.

4.3 Wave length features Selection and centroid determination of features

The centroids of several selected features from the ThAr will be used to optimize the parameters of model. It is important to know the accurately the wavelengths of these selected ThAr features and apart from accurate measurement of the centroids of features itself. Measurement of ThAr emission line wavelengths with very high precision and internal consistency were published

by Palmer & Engleman [37] using the 1-m Fourier Transform Spectrometer (FTS) of the National Solar Observatory at Kitt Peak using a commercial thorium-neon hollow cathode lamp [5]. Since then they are measured many times, of which the notable are - by Lovis & Pepe [28] using the High-Accuracy Radial-Velocity Planet Searcher (HARPS) [39], in the near infrared (NIR) through 5500 nm (1800 cm^{-1}) at a lamp current of 320 mA by Engleman et al. [18] using the McMath 1-m FTS, the NIR spectrum measured with the National Institute of Standards and Technology (NIST) 2-m FTS [36] from 691 nm to 5804 nm with a hollow cathode lamp running at 20 mA by Kerber et al. [24]. Also since 1983, a number of thorium lines have been measured with high accuracy by laser spectroscopy [16, 17, 45]. Most recently Redman et al.[42] have re-measured more than 1600 Th lines in NUV to NIR.

Atomic emission lines are caused by electron transitions from upper to lower energy levels. The accuracy of the wavelengths depends on the accurate values of the individual energy levels. Based on these energy levels, wavelengths of all possible transitions are calculated, which called the Ritz wavelengths. These Ritz wavelengths are compared with the observed wavelengths and an optimized list of wavelengths are compiled. For few electron atoms the calculated energy levels are more accurate than many electron system. The compilations discussed above is a combination of theory and experiment values. In [37], many energy levels of Th I and Th II are determined. Redman et al. [42] have re-optimized the energy levels of neutral ThI, Th II and Th III and calculated a list of 19874 Ritz wavelengths between 250nm to 5500 nm using previously published work mentioned above and their own measurements from 2-m FTS at NIST.

It can be noticed that all these studies have given emphasis is on Th lines, the reason is that Ar lines are highly susceptible to pressure shifts and the electrical current used for operating the lamp. The lines shift of Ar due to environmental conditions is of the order of several tens of m/s [28], so we will avoid using them for our purpose. Most ThAr lines have blended nearby

lines, even at $R \sim 150000$. This linelist [42] cannot be used directly as it is used in FTS which has $R > 120000$, while HESP operates at $R \sim 30000$ and 60000 .

The Ritz wavelengths in vacuum are used in the linelist compiled by Redman et al. (2014). Since HESP does not operate in vacuum, the wavelengths have to be calculated for the environmental conditions in the spectrograph enclosure. Wavelength in air is calculated by

$$\lambda_{air} = \frac{\lambda_{vac}}{n} \quad (4.1)$$

where n is the refractive index of air. Ciddor equation is used for calculating refractive index of air. We use the calculation followed by NIST. Inputs to the equation are: vacuum wavelength, pressure (p) in Pascal, temperature (t) in Celsius, CO_2 concentration, humidity as mole fraction.

Calculation:

Definition of constants:

$$\begin{aligned} w_0 &= 295.235 & k_0 &= 238.0185 & a_0 &= 1.58123 \times 10^{-6} \\ w_1 &= 2.6422 & k_1 &= 5792105 & a_1 &= -2.9331 \times 10^{-8} \\ w_2 &= -0.03238 & k_2 &= 57.362 & a_2 &= 1.1043 \times 10^{-10} \\ w_3 &= 0.004028 & k_3 &= 167917 & & \end{aligned} \quad (4.2)$$

$$\begin{aligned} b_0 &= 5.707 \times 10^{-6} & c_0 &= 1.9898 \times 10^{-4} & d &= 1.83 \times 10^{-11} \\ b_1 &= -2.051 \times 10^{-8} & c_1 &= -2.376 \times 10^{-6} & e &= -0.765 \times 10^{-8} \end{aligned} \quad (4.3)$$

$$\begin{aligned}
 p_{R1} &= 101325 \\
 T_{R1} &= 288.15 \\
 Z_a &= 0.9995922115 \\
 \rho_{vs} &= 0.00985938 \\
 R &= 8.314472 \\
 M_v &= 0.018015
 \end{aligned} \tag{4.4}$$

If $s = 1/\lambda^2$, λ being wavelength in vacuum,

$$\begin{aligned}
 r_{as} &= 10^{-8} \left(\frac{k_1}{k_0 - S} + \frac{k_3}{k_2 - S} \right) \\
 r_{vs} &= 1.022 \times 10^{-8} [w_0 + w_1S + w_2S^2 + w_3S^3]
 \end{aligned} \tag{4.5}$$

If x_{CO_2} is CO_2 concentration in $\mu\text{mol/mol}$,

$$\begin{aligned}
 M_a &= 0.0289635 + 1.2011 \times 10^{-8}(x_{co2} - 450) \\
 r_{axs} &= r_{as} [1 + 5.34 \times 10^{-7}(x_{co2} - 450)] \\
 T &= t + 273.15 \\
 Z_m &= 1 - \frac{p}{T} [a_0 + a_1t + a_2t^2 + (b_0 + b_1t)\chi_v^2] + \left(\frac{p}{T}\right)^2 (d + e\chi_v^2)
 \end{aligned} \tag{4.6}$$

where, Mole fraction,

$$\chi_v = \frac{RH}{100} \times f(p, t) \times \frac{p_{sv}(t)}{p} \tag{4.7}$$

Where RH is relative humidity in percent (between 0 to 100) and saturation vapour pressure,

$$p_{sv} = 10^6(2C/X)^4 \tag{4.8}$$

$$\begin{aligned}
 K_1 &= 1.16705214528 \times 10^3 \\
 K_2 &= -7.24213167032 \times 10^5 \\
 K_3 &= -1.70738469401 \times 10^1 \\
 K_4 &= 1.20208247025 \times 10^4 \\
 K_5 &= -3.23255503223 \times 10^6 \\
 K_6 &= 1.49151086135 \times 10^1 \\
 K_7 &= -4.82326573616 \times 10^3 \\
 K_8 &= 4.05113405421 \times 10^5 \\
 K_9 &= -2.38555575678 \times 10^{-1} \\
 K_{10} &= 6.50175348448 \times 10^2 \\
 \Omega &= T + \frac{K_9}{T - K_{10}} \\
 A &= \Omega^2 + K_1\Omega + K_2 \\
 B &= K_3\Omega^2 + K_4\Omega + K_5 \\
 C &= K_6\Omega^2 + K_7\Omega + K_8 \\
 X &= -B + \sqrt{B^2 - 4AC}
 \end{aligned} \tag{4.9}$$

And,

$$\begin{aligned}
 \rho_{axs} &= \frac{p_{R1}M_a}{Z_aRT_{R1}} \\
 \rho_v &= \frac{\chi_v p M_v}{Z_m RT} \\
 \rho_a &= \frac{(1 - \chi_v)p M_a}{Z_m RT} \\
 n &= 1 + \frac{\rho_a}{\rho_{axs}} r_{axs} + \frac{\rho_v}{\rho_{vs}} r_{vs}
 \end{aligned} \tag{4.10}$$

n is the refractive index of air at given environmental conditions. Using n and the equation 4.1 wavelength in air can be calculated for a given vacuum wavelength.

To find the centroid of a particular feature, the feature is identified in the 2D spectrum. A subsection of the image that is 3 times the FWHM of

the feature is extracted around the feature. Background from the subsection is subtracted and two 1D images are extracted by summing the subsection along two axes. A Gaussian function is fitted to the extracted 1D data and the centres of the two functions give the centroid of the feature. In order to take into account the continuum, following Gaussian functional form is used:

$$i(x) = Ie^{-\frac{(x-a)^2}{2\sigma^2}} + bx + c \quad (4.11)$$

where $bx + c$ takes care of the counts and slope in the continuum.

In some cases when multiple features are present in the subsection, sum of multiple Gaussians is fitted to the 1D data which otherwise may cause a shift in the centroid of the feature of interest. However, for the model predictions, the lines which are isolated with no blends are chosen for optimization. Since, some of the blended lines are separated by less than the FWHM that will naturally limit the accuracy of optimization. Error in fitting a single Gaussian of a blended feature will shift the centroid of the actual value towards the blended feature. This shift is dependent on the separation and the intensity ratio of the lines. Numerical simulations were performed to study the effect of separation and line strength ratio on the shift, and are shown in Fig. 4.4.

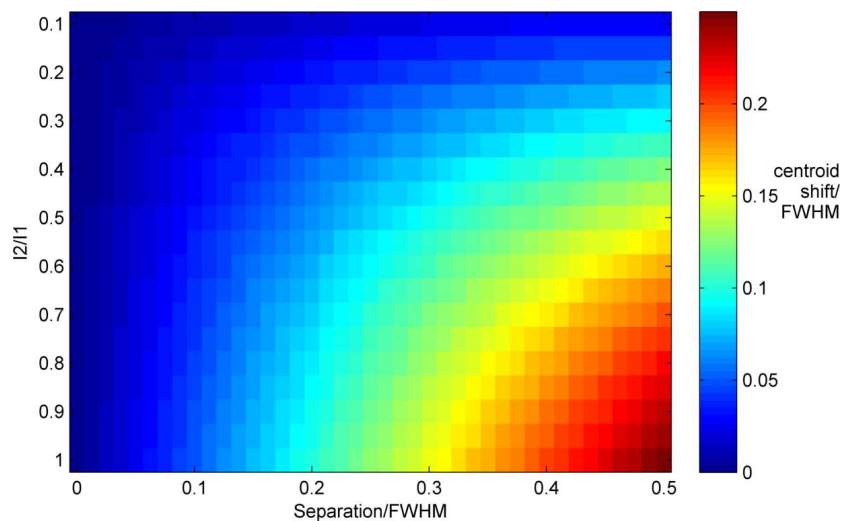


Figure 4.4: Numerical simulation results showing the shift in Centroid fitted for blends for different separations and intensity ratios

The plot shows the shift in centroid as fraction of FWHM in colour code for separation as fraction of FWHM and ratio of intensities. Also strong lines (not saturated) that can provide accurate centroid with small uncertainties were chosen.

4.4 Optimisation routine

The merit function which is the root mean square of difference between model predictions and instrument has multiple local minimum and may not have smooth functional form makes it difficult to calculate derivatives that are needed for regular optimization routines. Therefore simulated annealing optimization was employed for the purpose. Simulated annealing is a global optimizer that uses random search technique developed in 1983 [27] for highly non-linear problems. A key feature of simulated annealing is that it provides means to move away from local optimum by allowing ways to escape them probabilistically. Its ease of implementation and hill-climbing moves to escape local minima made it popular over past few decades.

Simulated annealing (SA) is named after its analogy with the process of physical annealing with solids where crystalline solid is heated and then cooled very slowly until it attains its minimum lattice energy state. Starting with an initial guess of the solution, SA algorithms generate a new point randomly at each iteration. The extent of area around the current position, in which a possible new point will be selected is based on a probability distribution with a scale proportional to temperature. First a random direction vector in the parameter space is generated and is then multiplied by step size dependent on temperature, which can be either same in all directions or different in different axes. Initially when the temperature is high, the possible new point can be from a larger area in the parameter space allowing a global optimum. With time, the temperature is scaled down, the search area gets smaller and smaller converging onto the minimum point.

For every new point, the objective function, f , is calculated and is compared with the current point's objective function. If the new point gives a smaller function value, the new point is accepted always. If the function is greater than current point function, it may be accepted with a certain probability. By accepting the points that increases the value of the objective function helps avoiding to get trapped in local minimum. The most frequently used acceptance function is the metropolis function. The probability of accepting a new candidate w' as the current solution w is

$$p(\textit{acceptance}) = \begin{cases} e^{-(f(w')-f(w))/t_k}, & f(w') - f(w) > 0 \\ 1, & f(w') - f(w) \leq 0 \end{cases} \quad (4.12)$$

For every temperature, t_k , this procedure is repeated for a predefined number of times or till the objective function reaches the stopping criteria. t_k is the temperature parameter of the annealing procedure at the outer loop k^{th} iteration such that

$$t_k > 0, \quad \lim_{k \rightarrow \infty} t_k = 0 \quad (4.13)$$

Since the annealing schedule defines the degree of uphill movement permitted during the search, it is critical to the algorithm performance. The basic idea of the schedule is that ascent steps should be accepted with low probability when the current point is in the vicinity of global optimum. For the annealing schedule following needs to be specified,

Initial temperature, T_0 should be hot enough to allow a move to almost any neighbourhood state. If this is not done then the ending solution will be the same (or very close) to the starting solution. Alternatively, we will simply implement a hill climbing algorithm. If the temperature starts at too high value then the search can move to any neighbour and thus transform the search (at least in the early stages) into a random search.

Final temperature, T_f ideally zero. However, this can make the algorithm run for a lot longer. It is not necessary to let the temperature reach zero, the stopping criteria can either be a suitably low temperature or when the system is “frozen” at the current temperature (i.e. no better or worse moves are being accepted).

A length for the Markov chains (number of iterations per temperature, t_k)

A rule for decrementing the temperature, simplest and frequently used being

$$t_{k+1} = \alpha t_k.$$

Following steps presents the complete algorithm:

- Set all the initial parameters, Initial guess, w , starting temperature t_0 , number of iterations per temperature, M , stopping criteria, temperature scale α .
- Repeat till Stopping condition meets.
- For $j = 1$ to M , generate new point, w'
- Check if $f(w') - f(w)$ is less than zero
- If it is less than zero, $w = w'$
- If not, generate a random number $0 < r < 1$, if $p = e^{-(f(w')-f(w))/t_k} > r$, then, $w = w'$.
- Next j
- $t_{k+1} = \alpha t_k$
- Check for stopping condition.

4.5 Glass Refractive indices

Optical glasses are classified by their chemical components. In HESP, prism and the camera optics consist of various glasses from OHARA and SCHOTT. BSL7Y was used for the cross disperser prisms, and S-FPL51Y, BAL15Y, S-FSL5Y, BSL7Y, N-BAK2, F_SILICA are used for camera optics. Optical properties of relevance for any glass are – refractive index, dispersion formula, and effect of temperature on refractive index.

Any glass manufacturer’s catalogues provide all the required information. Since, we do not have the facilities to carry out these measurements; we had to rely on the methods and results from the manufacturer. According to the information from the vendor [1, 2] refractive index of glass is measured using either v-block refractometer which gives an accuracy of about +3E-5 or with precision spectrometers that can measure indices at an accuracy level of 4E-6. Refractive index homogeneity is measured using interferometers with accuracy of around 10nm wavefront peak to valley. In general manufacturers provide refractive index values for some wavelengths. In order to calculate the refractive index at any wavelength, dispersion formula is defined. There are many formulas that fit the dispersion but the most generally used is the Sellmeier formula,

$$n^2 - 1 = \frac{A_1\lambda^2}{\lambda^2 - B_1} + \frac{A_2\lambda^2}{\lambda^2 - B_2} + \frac{A_3\lambda^2}{\lambda^2 - B_3} \quad (4.14)$$

where A_1, A_2, A_3, B_1, B_2 and B_3 are the constants that can be found by least square fitting using the refractive indices of standard wavelengths measured from several melt samples and λ is wavelength in micrometers. The formula is valid only in the spectral range defined. Using Eqn. 4.14, the refractive index of any wavelength can be found to an accuracy of about +5E-6.

Refractive index is affected by change in temperature; The temperature coefficient of refractive index is used to take care of this. But a single number

will not be enough given the non-linear variation of the indices with temperature. Schott Glass Technologies Inc. has developed a model for calculating the change in refractive index with temperature described as following:

Manufacturers determine the temperature coefficient of refractive index dn/dt by measuring the refractive index from -40 to 80 °C at different wave lengths. From these the absolute refractive index can be calculated by

$$\left(\frac{dn}{dt}\right)_{absolute} = \left(\frac{dn}{dt}\right)_{relative} + n \frac{dn_{air}}{dt} \quad (4.15)$$

The temperature coefficients of absolute refractive indices at any temperature and wavelength can be calculated using

$$\frac{dn_{abs}(\lambda, T)}{dT} = \frac{n^2(\lambda, T_0) - 1}{2n(\lambda, T_0)} \left(D_0 + 2D_1\Delta T + 3D_2\Delta T^2 + \frac{E_0 + 2E_1\Delta T}{\lambda^2 - \lambda_{TK}^2} \right) \quad (4.16)$$

where,

T_0 Reference temperature specified for the glass

T Temperature in °C

ΔT Temperature difference with respect to T_0

λ Wavelength in vacuum

$D_0, D_1, D_2, E_0, E_1, \lambda_{TK}$ are constants depending on glass type

Using the measured dn/dt data, the constants in Eqn.4.16 is derived. The constants in this formula are given in the data sheets. These values are meant to be approximate guiding numbers and manufacturers can provide measurements on individual melts on request.

Following steps are used in the calculation of refractive index of a glass using the above equations at a given wavelength and temperature.

- Wavelengths in the air are calculated given the environmental data using Eqn.4.1 – 4.10

- Absolute refractive index of air at temperature T_s and pressure P_s is calculated using

$$\begin{aligned} n_{air} &= 1 + \frac{(n_{ref} - 1)P}{1 + (T - 15)(3.4785 \times 10^{-3})} \\ n_{ref} &= 1 + \left[6432.8 + \frac{2949810\lambda^2}{146\lambda^2 - 1} + \frac{25540\lambda^2}{41\lambda^2 - 1} \right] \times 10^{-8} \end{aligned} \quad (4.17)$$

where λ is wavelength at the system temperature and pressure.

- If T_{ref} and P_{ref} are the reference temperatures of the glass specified in the glass catalogues, $n_{air}(T_s, P_s)$ and $n_{air}(T_{ref}, P_{ref})$ are calculated using Eqn.4.17.
- Relative wavelength is calculated as shown below,

$$\lambda_{rel} = \lambda \frac{n_{air}(T_s, P_s)}{n_{air}(T_{ref}, P_{ref})} \quad (4.18)$$

- Using the dispersion Eqn.4.14, we calculate relative index at reference temperature and pressure, $n_{rel}(T_{ref}, P_{ref})$ at λ_{rel} , and absolute refractive index

$$n_{abs}(T_0, P_0) = n_{rel}(T_0, P_0) \times n_{air}(T_0, P_0) \quad (4.19)$$

- Refractive index at the system temperature and pressure can be calculated from,

$$n_{abs}(T_s, P_s) = n_{abs}(T_0, P_0) + \Delta n_{abs} \quad (4.20)$$

where, Δn_{abs} is calculated using Eqn.4.16 with

$$\begin{aligned} n &= n_{rel}(T_{ref}, P_{ref}), \\ \Delta T &= T_s - T_{ref}, \\ \lambda &= \lambda_{rel} \end{aligned} \quad (4.21)$$

- Finally,

$$n_{rel}(T_s, P_s) = \frac{n_{abs}(T_s, P_s)}{n_{air}(T_s, P_s)} \quad (4.22)$$

In order to match model with the instrument, it is important to get the refractive index data correct. Since the glass blanks were purchased much before this work was initiated, we did not request the glass manufacturers for the coefficients and data of the melt. The refractive indices and dispersion will vary slightly from melt to melt, as these are highly dependent on annealing factors. Ohara melt data contained the refractive indices nC, nd, nF, ng which are at the spectral lines of wavelengths 656.27 nm, 589.29 nm, 486.13 nm, 435.835 nm respectively, Schott melt data report contains nd, ne, ν_d , ν_e , nF – nC, nd – nC, nF – nd, nF – ne, ng – nF, nF' – nC', nF' – ne where ne, nC', nF' are indices for wavelengths 546.07 nm, 643.85 nm, 479.99nm respectively. ν_d , ν_e are the Abbe numbers quantifying dispersion given by,

$$\begin{aligned} \nu_d &= \frac{nd - 1}{nF - nC} \\ \nu_e &= \frac{ne - 1}{nF' - nC'} \end{aligned} \quad (4.23)$$

Using these numbers from the melt data, the coefficients of the dispersion formula are adjusted. If the complete data of the melt was obtained from the manufacturer a more accurate dispersion formula is possible. In order to understand the implications of difference in coefficients from actual values, some simulations were performed. Two components that use this information are the prisms and the camera optics.

Prism is responsible for the cross dispersion of the different orders. A difference in the dispersion formula will cause a difference in the order spacing and to very small extent order tilts. Since we are using only four or six indices available to adjust the dispersion solution, two different optimizations were tried,

1. A_1 , A_2 , A_3 were optimized to fit to the data

2. B_1, B_2, B_3 were optimized to fit to the data

to induce difference in dispersion formula. A difference in the profile of the dispersion formulae is obvious between the two cases. Fig.4.5 shows the difference in the profiles for one of the glasses from the other which is of the order 10^{-5} .

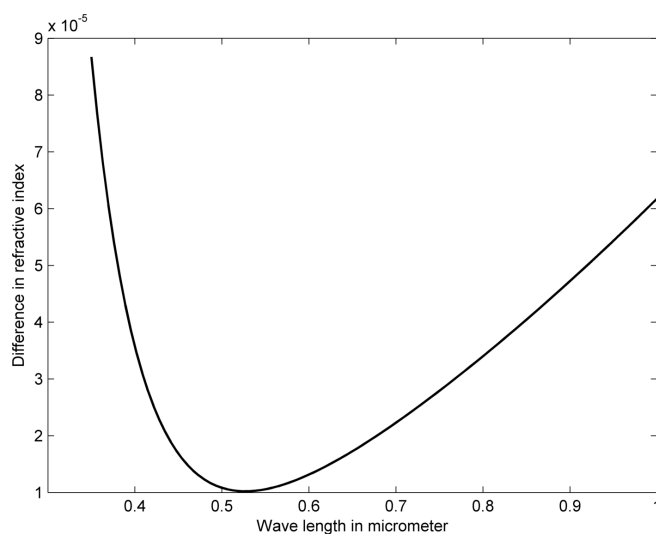


Figure 4.5: Difference in the refractive index for two optimizations described in text

Fig. 4.6 4.6 shows the shift in the spectrum due to this difference in the prism glass dispersion in HESP spectrograph, assuming the values used for the glasses in the camera optics is accurate. It will be difficult to isolate this effect from all the rest of the parameters in the model. Also during optimization, this effect may be compensated by other parameters. Hence, the best choice will be to get the most precision melt data from the glass manufacturers or make measurements in any other facility.

Fig. 4.7 shows pattern in the changes in spectrum with a little alteration of the dispersion coefficients in camera optics. With the discrepancies from measurements and fitting errors kept within possible limits, the spectrum shifts were well within one pixel. In the Fig. 4.7 it can be seen that for various differences introduced, the pattern introduced is similar with varying magnitudes.

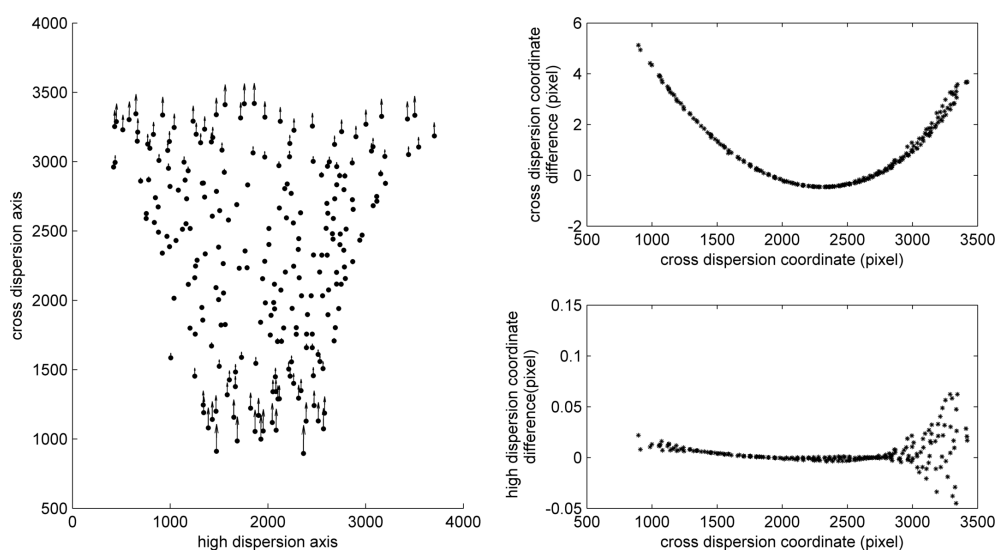


Figure 4.6: Depiction of shift in spectrum from calculated positions due to mismatch in prism glass refractive indices data. Left: Vector plot showing the pattern in shift, Right: Shift in cross and high dispersion coordinates with respect to cross dispersion coordinate of the wavelengths positions on the CCD

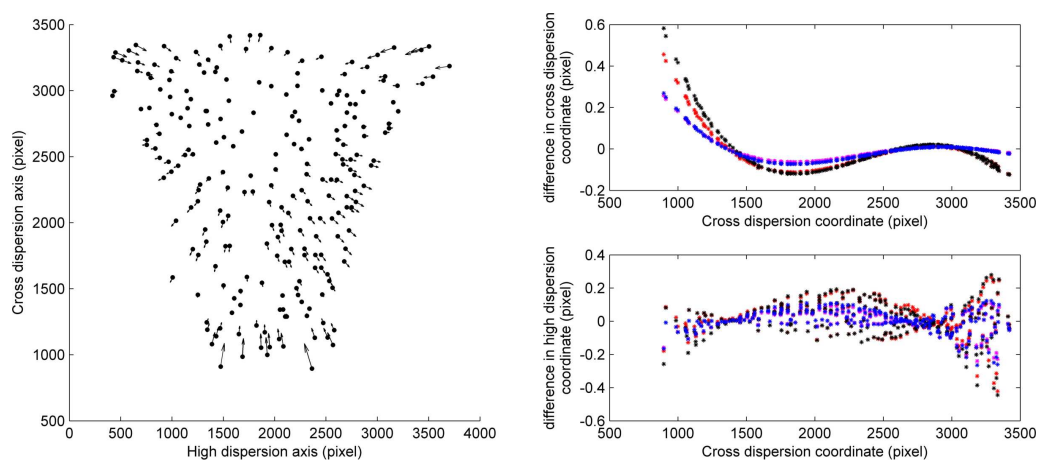


Figure 4.7: Depiction of shift in spectrum from calculated positions due to mismatch in camera glasses refractive indices data. Left: Vector plot showing the pattern in shift, Right: Shift in cross and high dispersion coordinates with respect to cross dispersion coordinate of the wavelengths positions on the CCD for multiple cases

When the spectrum is taken from the instrument, the difference between standard model of the design file and the instrument is a result of all the discrepancies in the system which is not easy to separate. Hence the differences will be treated as a polynomial correction. This will be discussed in the results chapter when the data from the instrument is handled.

In order to understand how the optimization is going to work with differ-

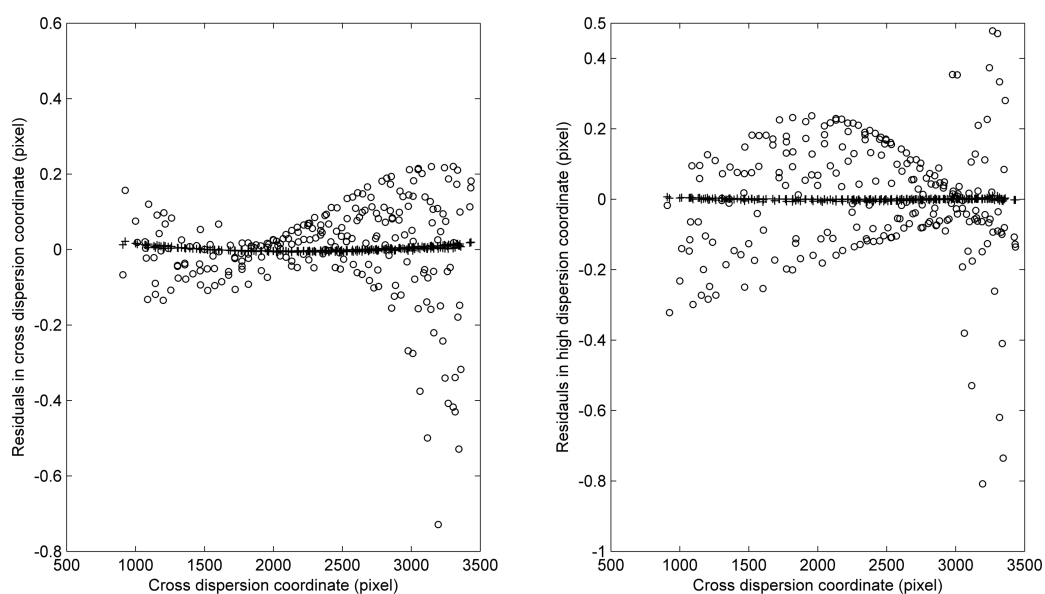


Figure 4.8: Residuals in the wave lengths positions on the CCD after optimization of the model for two cases. +: when the glass data of the model and instrument matched, o: glass data between model and instrument differ

ences due to mismatches in glass data used, a simulation was done. Multiple parameters of the glass data were changed randomly by a small amount and differences in the positions of the features were calculated. Using this changed glass data, a final optimization of the model was carried out. In Fig.4.8 the residuals for two cases was shown. + sign shows the residuals when the glass data of the model and instrument are same. O sign shows the residuals when the glass data had discrepancies in model and actual instrument. The residuals from the later case are not totally compensated by the parameters used for optimization. It is observed that the discrepancy due to glass data for the prism is compensated to some extent by other system parameters used in the optimization, while large residuals are still present showing the effects from the inaccurate camera optics glass dispersion data. Hence a discrepancy can be detected due to the inaccurate input data, however the actual contribution from each component giving raise to the differences cannot be worked out from this.

Chapter 5

Results

Performance of the model is evaluated by comparing the output with the standard commercial raytrace software like, Zemax. Raytrace is carried out for a list of reference wavelengths using the analytical model and the resultant centroid positions at the CCD plane are compared with the results from Zemax software. The plots in Fig.5.1 show the differences in the centroid position of the reference wavelengths in x and y coordinates between Zemax and model. We also show the effect of inclusion of various orders in aberration terms. As expected, the contribution from the third order term dominates. Including contributions of terms till the seventh order reduces the difference between the model and ZEMAX to an order of 10^{-5} mm.

After an initial alignment of instrument at the Kiwistar lab, several Thorium Argon spectra were taken and the following aspects of the model was tested using these ThAr spectra.

1. Accuracy of the model predictions.
2. Effect of noise in the model predictions
3. Reliability of the estimated parameters
4. Shift in spectrum

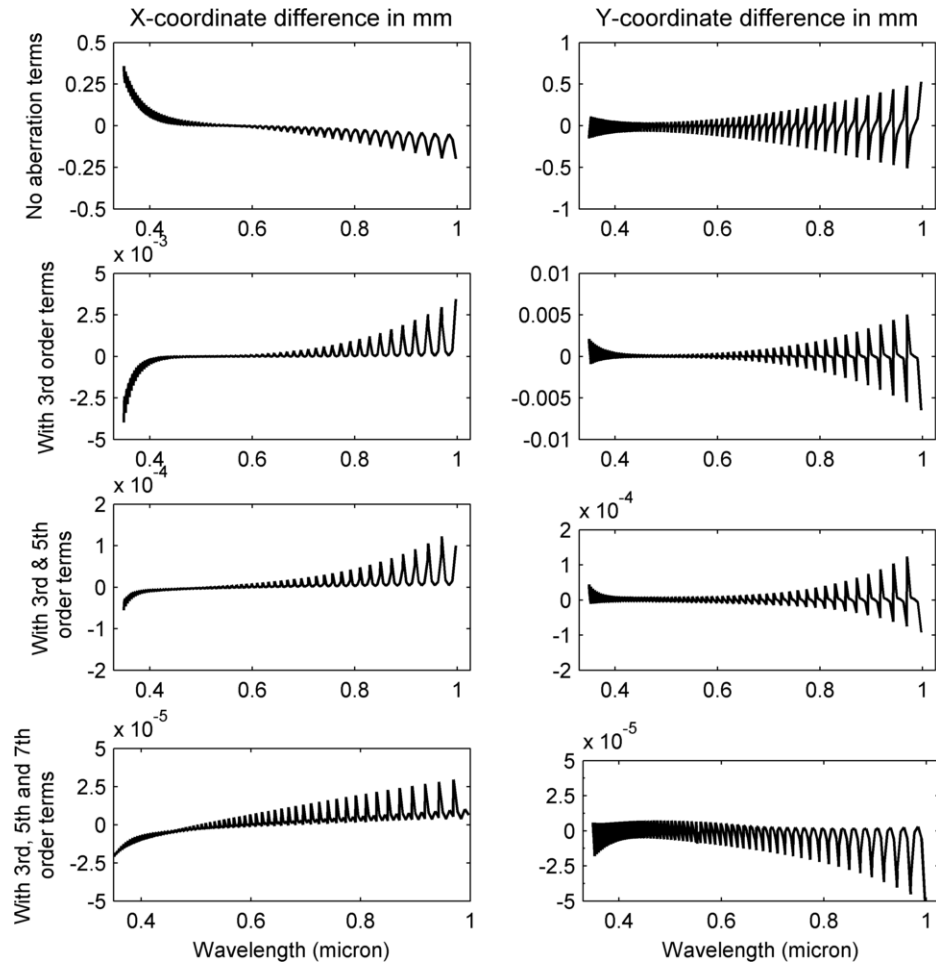


Figure 5.1: Plots showing the difference between Zemax trace and model for various aberration terms included. First column is the difference in x-coordinate, second column is the difference in y-coordinates. Each row of plots is difference in coordinates when various orders of aberration terms added as indicated in the far left of each row. X-axis of the plots is wavelength in microns, y-axis is the difference in the coordinates in mm

5. Accuracy of dual fiber in tracking the relative shifts.

5.1 Accuracy of the analytical model

5.1.1 Preliminary data and Optimization of the model

we start with validation of the accuracy in the prediction of the wavelength position. Several ThAr features distributed all over the CCD were chosen. The features that are selected are strong enough and isolated to get minimal measurement errors in the determination of the centroids as described in

chapter 4. Fig.5.2, shows the distribution of 92 features over the spectrum that were selected for measuring the centroids. ThAr spectrum from the instrument at the room temperature was used for this. Though the room was thermally controlled, the electronics and computers were placed in the same room. The passive inner enclosure was placed on the table. Left hand side panel in the Fig.5.2. shows the trace of the 64 orders and the 92 lines selected over plotted.

In order to understand the effect of different parameters, various subsets of the parameter were optimized, and differences in the predicted wavelength position to the measured values are compared. As discussed in Chapter 4, parameter set is updated studying these residual patterns. The right hand side panel of the Fig.5.2 shows the plot with difference between the measured line positions and the predicted positions from the optimized model for both high dispersion direction and cross dispersion direction with all relevant parameters included in the optimization set.

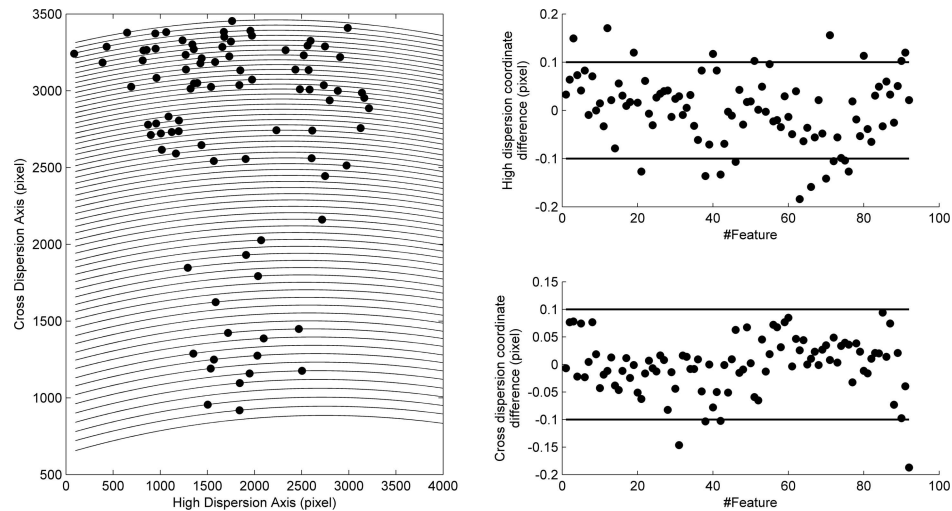


Figure 5.2: Scatter on the left shows the selected features' positions on CCD across different orders of ThAr spectrum from the instrument that are used for optimization. The plots in the upper right panel and the lower right panel are the differences in high dispersion and cross dispersion coordinates of measured positions and optimized model predicted positions for all the features used for optimization

In order to test for the accuracy of the optimized model, a new set of lines which are not already used for optimization are used. A new set of

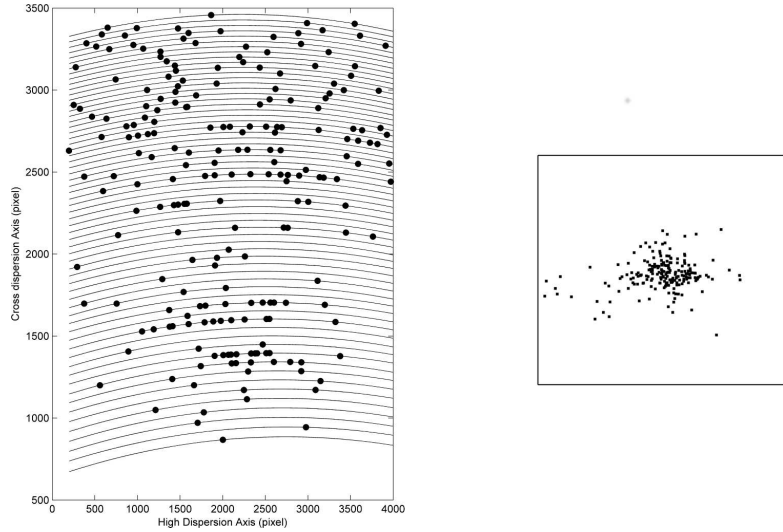


Figure 5.3: Left: Selected test features' positions across different orders used to test the accuracy of the optimized model. Right: Scatter of residuals for test features. The box represents one pixel

about 200 lines are selected shown in the Fig.5.3 left panel to check the accuracy of the optimized model. Fig.5.3 shows the residuals of the optimized model predictions and measured positions for these 200 lines. The size of box showing the scatter represents a pixel.

The scatter of the residuals is mostly concentrated at the centre. The points that are far from the centre are mostly due to issues with centroiding of the features- either due to multiple features in the subimage that are unaccounted for or a very low signal to noise ratio of the feature. The effect of unaccounted multiple features in the subsection of the image can be seen as the greater spread in the high dispersion direction (horizontal axis in Fig.5.3) than the cross dispersion direction.

The instrument was also tested in an environmental chamber with regulated temperature and pressure. The computers and relevant electronics were placed outside the chamber. An ambient temperature of 170C and 1.0159 KPa pressure is maintained in the chamber. Within the inner enclosure, the mean temperature was 16.79 0C. The above described accuracy test was repeated on the ThAr exposures taken in the chamber.

The same 92 features' centroids were determined from the new exposures

and the model was optimized. Figure shows residuals of 1000 test features used to test the accuracy. The features selected (Fig.5.2) for optimizing the model are not uniform and some of the regions of the spectra are not covered. A new subset of 300 lines to optimize the model was chosen as shown in the Fig.5.4 to see if the number of distribution of the features selected for optimization has any effect on the final optimized model.

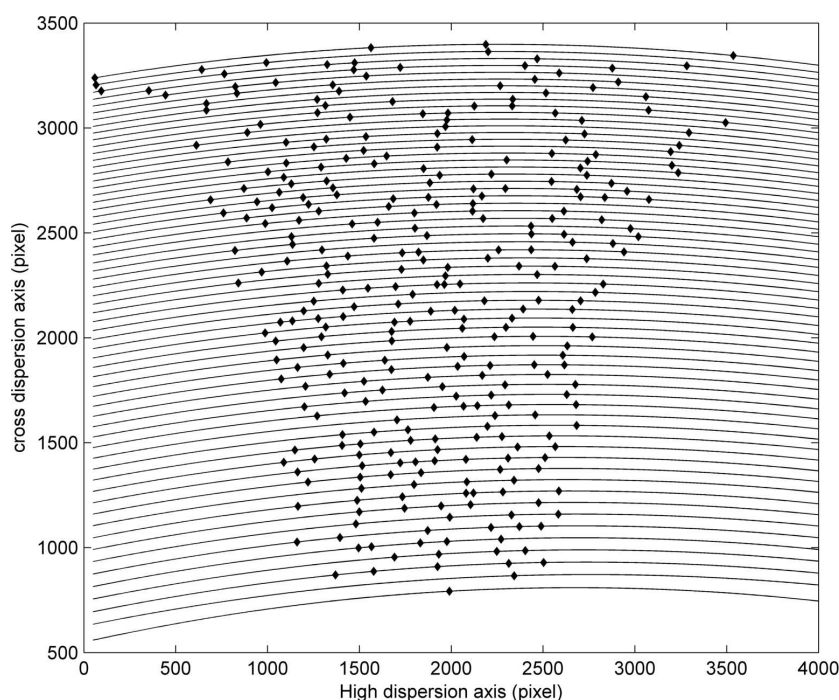


Figure 5.4: A new set of 300 lines selected for optimization to test the effect of number of features used for optimization on the accuracy of the optimized model

Panel on the right in Fig.5.5 shows the scatter of residuals of the 500 test features for the 300 features based optimization. The scatter on the left panel (which is based on the model derived from optimization using only 92 features) shows a larger scatter and lacks general symmetry. Table 6.1 compares the performance of optimizations using 92 ad 300 features. Root mean square of the residuals was calculated to compare between for the two plots.

RMS for 92 feature optimization: 0.1087

RMS for 300 feature optimization: 0.0602

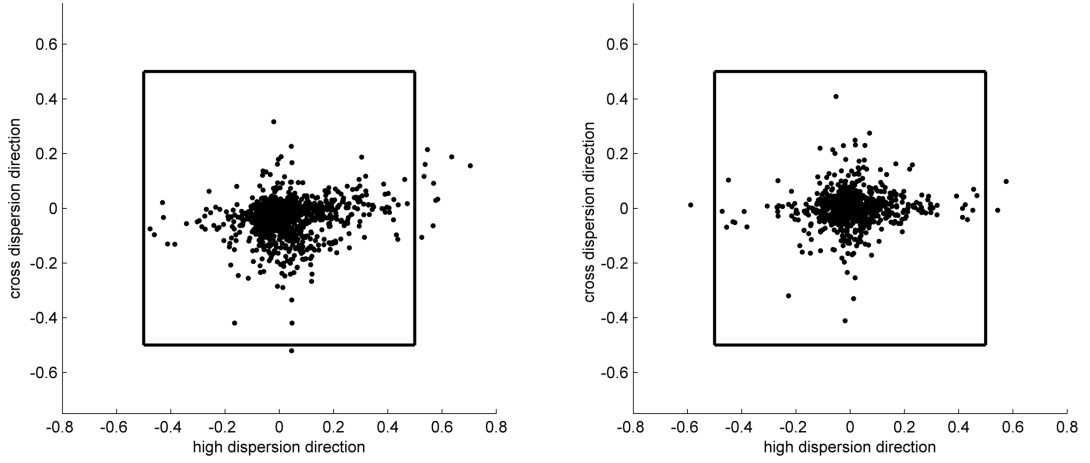


Figure 5.5: Scatter of test features' residuals in position for optimization using 92 features (left) and 300 features (right). Right panel shows a more symmetric scatter centred around (0,0)

This can be explained with the obvious reason that the parameters will be optimized in order to minimize the difference. When the features selected are concentrated in only a particular region, the optimization will terminate as long as the difference is minimized for that region of the spectrum. So features distributed all over the spectrum is desirable for optimization.

Table 5.1: Performance comparison for optimizations using 92 ad 300 features.

Number of features for optimisation	Axis	Mean of error (Accuracy in pixel)	Standard deviation of error (precision in pixel)
92	High	0.0377	0.1452
	Cross	-0.0355	0.0731
300	High	0.0126	0.1183
	Cross	0.0027	0.0585

5.1.2 Weighted RMS Merit Function

The merit function used so far has been the sum of squares of difference of the coordinates of the centroids of ThAr features from calibration frame and the predictions of the optimized model. This has equal weights for all the ThAr features, however different Thorium lines considered have different intensities.

In order to take into the intensity dependent centroid uncertainties, weighted root mean square error is used as the new merit function. The reciprocals of error in centroids are taken as the weights so that the features with less error are given more preference in the merit function. A set of wavelength features with good intensity levels are chosen and model is optimized. The table 1 in Appendix A gives wavelengths and the echehle order number of the features used for weighted RMS optimization. A total of 550 features were identified. Fig.5.6 shows the scatter of residuals of the same.

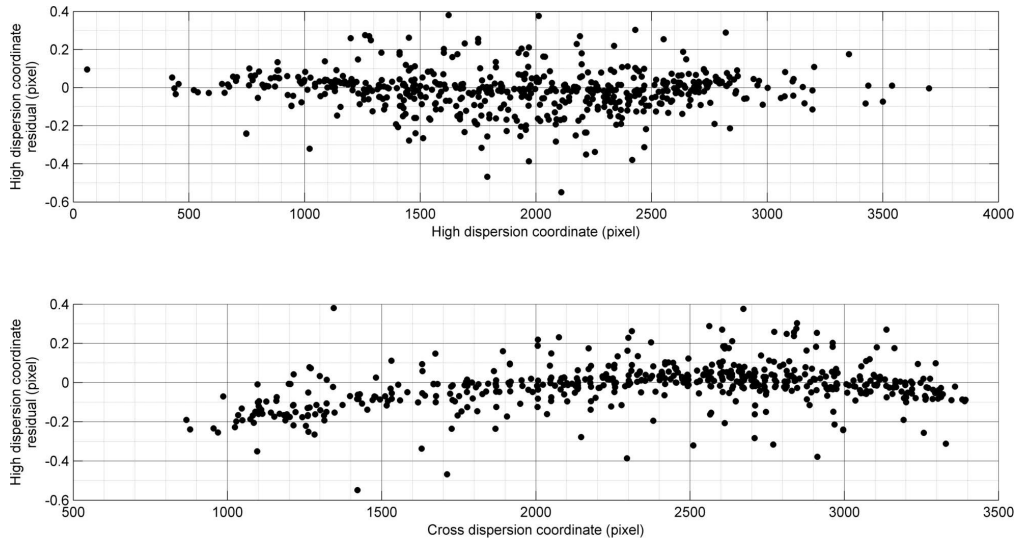


Figure 5.6: Residuals of the high dispersion axis coordinates of 550 features used for optimization with weighted mean square as the merit function. Top panel: Difference between measured and optimized model predicted high dispersion axis coordinates versus High dispersion coordinate of the respective feature, Bottom Panel: Difference between measured and optimized model predicted high dispersion axis coordinates versus Cross dispersion coordinate of the respective feature

In the residuals versus cross dispersion coordinate plots (Fig.5.7), the residuals are large at the far left end, which in agreement with the reduced intensity in the blue end of the spectrum. The number of lines selected in different orders is different. While some mid orders have huge number of usable lines, blue and red ends have few features. Fig.6.8 shows the histogram of number lines in different orders.

To understand if the number of features in different orders has any effect on optimization of the model, almost same number of features were selected

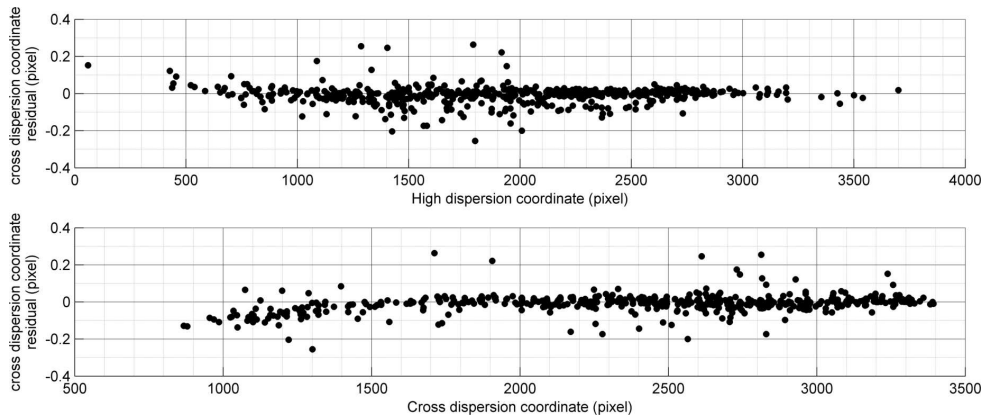


Figure 5.7: Residuals of the cross dispersion axis coordinates of 550 features used for optimization with weighted mean square as the merit function. Top panel: Difference between measured and optimized model predicted cross dispersion axis coordinates versus High dispersion coordinate of the respective feature, Bottom Panel: Difference between measured and optimized model predicted cross dispersion axis coordinates versus Cross dispersion coordinate of the respective feature

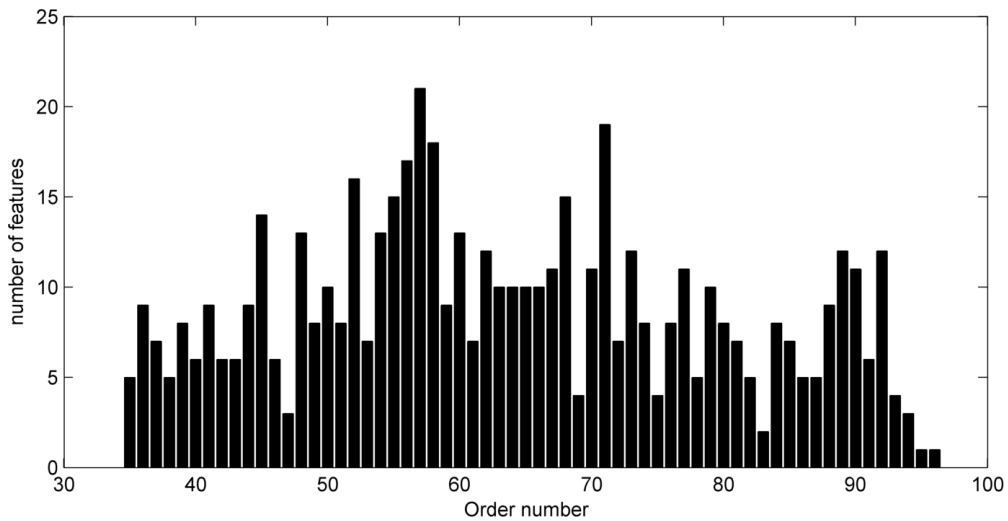


Figure 5.8: Histogram showing the number of features selected for optimization in different orders

in each order (four or less features per order) and model is optimized (Table 2 Appendix A). Fig.6.9 shows the residuals from this optimization using almost same number lines in all orders.

From the scatters it is obvious that the residuals pattern is not affected by choosing less number of lines per order as long as they cover the spectrum. In principle it is not necessary to select features in every order, but to optimize the model to a good accuracy including the non-linearities, it is good

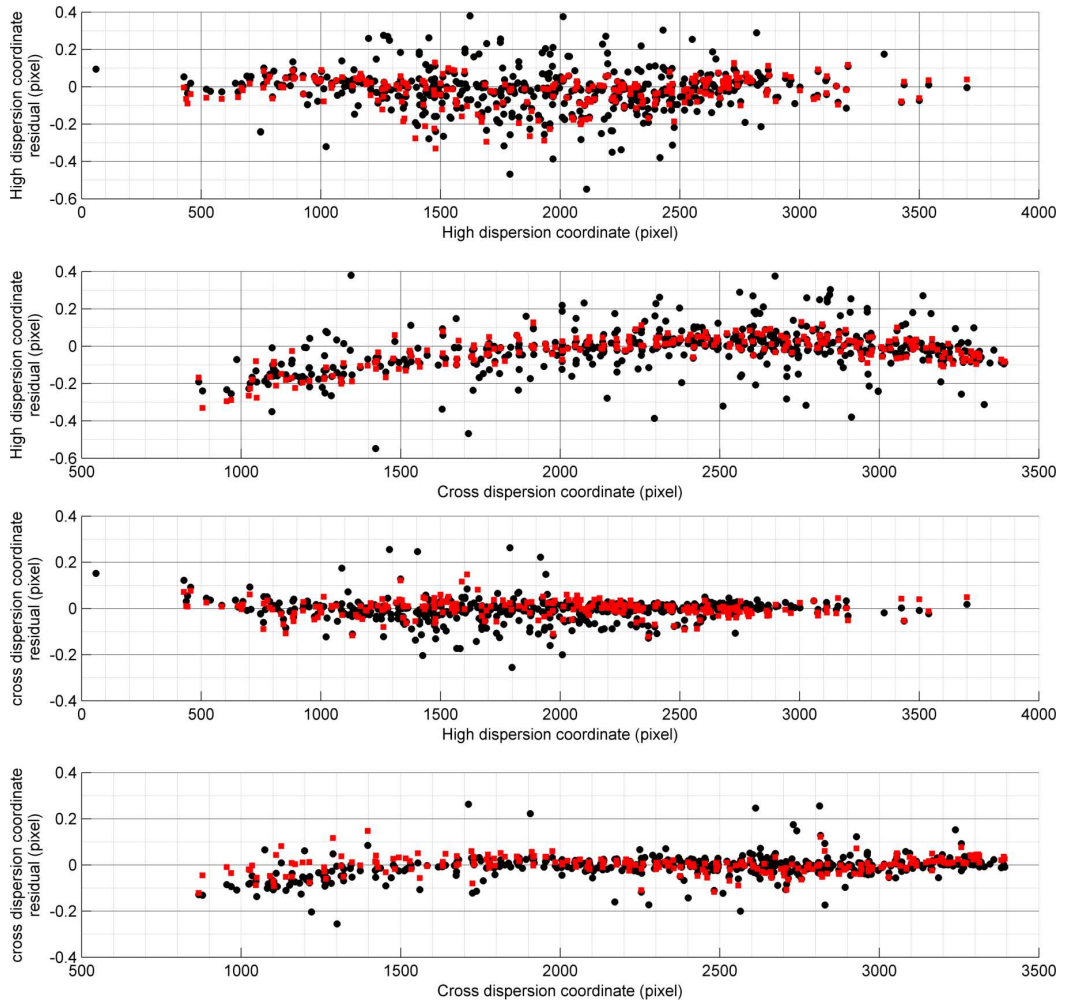


Figure 5.9: Black scatter points are same as Fig 5.6 and Fig 5.7. These scatters are over plotted with the respective residuals of the 233 features (a subset of the 550 features) after the model was optimized using the 233 features

to choose a uniform distribution of lines covering the edges and the center regions equally considering there are no discontinuities in the dispersion and distortions in the spectrum. 720 features which are not used for optimization were used to test the accuracy of the optimized model. Scatter of residuals (blue points) in the Fig.6.10 shows the performance of the optimized model. A low order 2D polynomial is fit to the residuals to take care of the patterns observed. Green scatter in Fig.6.10 shows the residuals after the polynomial fit. The box around the scatter depicts one pixel size. Table 5.2 shows the mean and standard deviation of test features' residuals.

Table 5.2: Mean and Standard deviation of test features' residuals

Axis	Residual mean value (pixel)	Residual standard deviation (pixel)
High	0.006915	0.1115
Cross	0.000249	0.0587

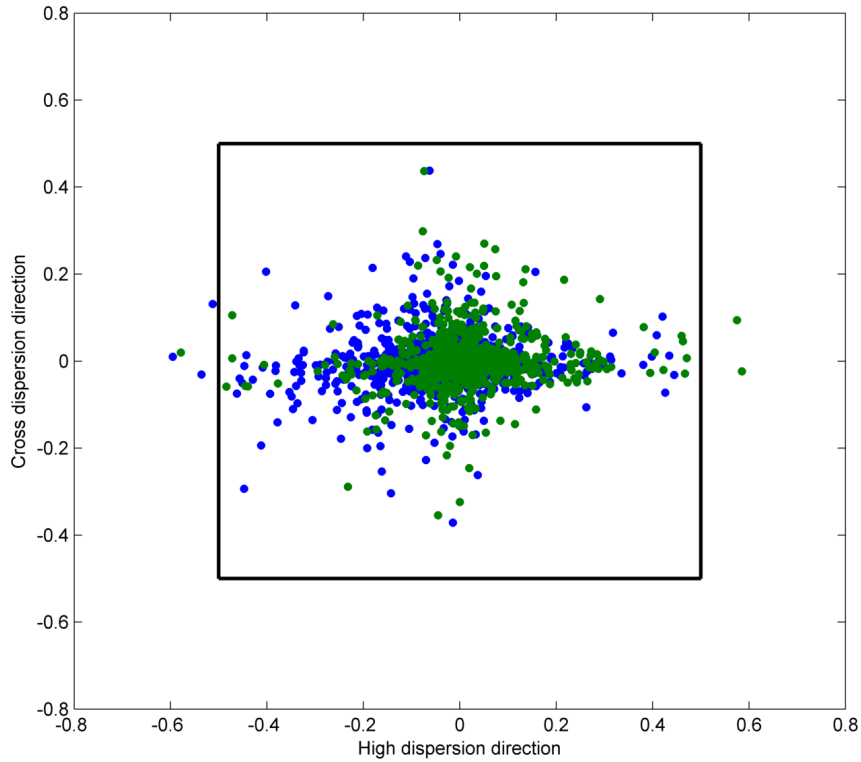


Figure 5.10: Scatter of 1000 test features' residuals in position for model optimized using 233 features and weighted mean square error as the merit function. Blue: Residuals before the polynomial fit to correct for the residual patterns seen in Fig.6.9, Green: Residuals after the 2D polynomial fit to correct the residual patterns seen in Fig.6.9

Outliers

The residual scatters in both Fig.5.5 and 6.10 have similar extreme outliers. It is important to understand the reason for the outliers since a realistic model, good S/N lines and very small uncertainties in the wavelengths should not cause such high discrepancy. More scatter can be observed in the high dispersion direction than the cross dispersion direction. The black lines shown in Fig.5.11 (High dispersion coordinate residuals for different test features)

depict the 0.05 pixel and 0.1 pixel bounds. From visual observation, most of the lines are concentrated between the 0.05 pixel bounds. About 80% of the residuals are between -0.1 pixel and 0.1 pixel, and 63% of lines residuals are between -0.05 and 0.05 pixel. An improper fit to the model is expected to show a trend in the residuals, hence the large residual and outliers could be due to issues in the centroid measurement of the Th features in the image, uncertainty in the wavelength of the feature considered for the model.

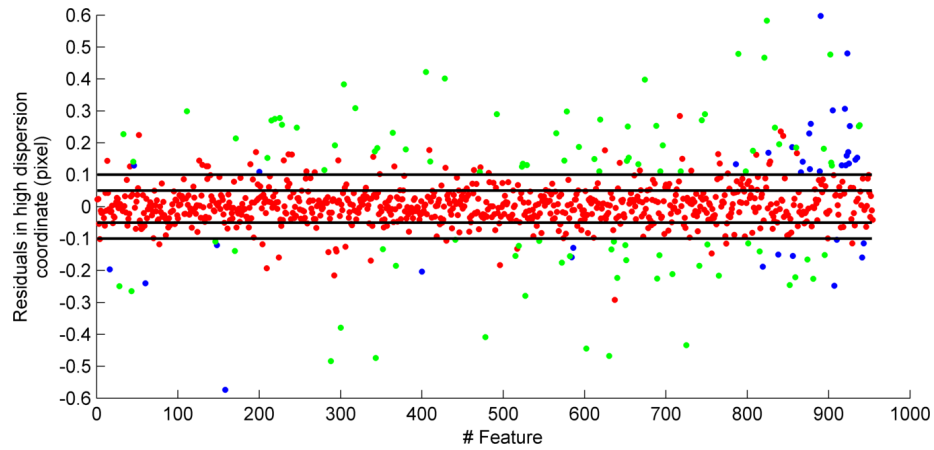


Figure 5.11: Difference in high dispersion coordinates of measured and optimized model predicted positions of the test features for different features used. The features in the left are in the red region and the blue region is to the right. The two black solid lines depicts the 0.1 and 0.05 limits

The uncertainties in the Ritz wavelengths calculated by Redman et al. (2014) can not account for the outliers of this magnitude. About 30% of the outliers (marked blue in the Figure 5.11) are very weak lines with high errors in the centroid positions. The right end of the scatter plot corresponds to the blue end of the spectrum whose efficiency is generally poor. This could be the reason for more scatter in this end. About 50% of the outliers have identified neighbours (Th or Ar) within less than one FWHM of the feature (Marked green in the Fig.6.11). When the blended features are identified as a single line and, the centroid is determined using a single Gaussian, then the measured centroid will be shifted towards the blended line (Ref Fig.4.4). This shift is dependent not only on the separation between the lines but also the relative intensities of the lines. Fig.4.4 shows result of numerical simulations of the

centroid shift observed when two gaussian features separated at a higher resolution, however identified as one feature for HESP resolution. The simulation shows effect of centroid shift for different relative intensities and separation of the two blended lines. The rest of about 30% outliers were analysed individually. It is observed that while most of these lines have blends which are lines not identified in the atlases used, some lines have intense gradient background which can cause centroid shift.

The FWHM values of the Gaussian fits and visual inspection were used to determine the possibility of a blend. The FWHM of the feature was compared to neighbouring features. Considerable discrepancies are concluded as presence of blends in the features. Mean and standard deviation of the residuals of the test features without these outliers improved to 0.000957 pixels and 0.04097 pixels respectively in high dispersion directions.

5.1.3 Dispersion Solutions

As the next step, the dispersion estimate by the model was compared with conventional reduction and dispersion solution estimate using IRAF package. Echelle reduction package in IRAF fits a 2D function to the ThAr dispersion relation. The two variables being the order and the high dispersion coordinate.

$$\lambda = f(x, o)/o \quad (5.1)$$

where o is the order number and x is the position coordinate. And,

$$f(x, o) = \sum_{n=0}^{opow} \sum_{m=0}^{xpow} C_{mn} P_{xm} P_{on} \quad (5.2)$$

Where $opow$ and $xpow$ are the maximum powers of x and o , and P_{xm} , P_{on} can be Chebyshev or Legendre polynomials with x and o variables respectively. The order of x and o are chosen such that the optimum root mean

square is achieved and yet the polynomial doesn't over fit the data. As it is not possible to do an inverse operation with the model, the positions of various wavelength features spaced uniformly in the spectrum are calculated from the optimized model. The grid calculated with uniform spacing is used for interpolations.

Fig.6.12 shows the dispersion of the residuals for the two solutions for the same set of features. Open circles indicate the residuals of the dispersion solution from polynomial fitting of IRAF, while the squares indicate the residuals from the model as described above. The root mean square error has reduced by 10 times. The intensity in the spectrum falls considerably in the blue end which is visible as spread in scatter.

5.2 Noise precision of model predictions

Different lines in the spectrum have different intensities and accordingly different uncertainties associated with the positions measured. To understand the effect of these uncertainties on model optimization and predictions, bootstrap Monte Carlo simulations were performed. The coordinates of the lines used for model optimization were subjected to random variations with poisson statistics of photon noise (as lines selected have negligible readout and bias noises compared to photon noise). These positions were used to optimize the model. Multiple runs of these variations and optimizations were done. For all the runs, the optimized model was used to predict test features' positions. Standard deviation of predicted features was measured.

Fig.6.13 shows the error in the measured positions and the error in predicted positions from the model. It is also observed that the error in model predictions is dependent on the intensity of lines used for optimization and the bounds used on the open parameters during optimization (given the possibility of multiple solutions from the optimization). A gradual change of uncertainties within the order and a variation within an order itself can be

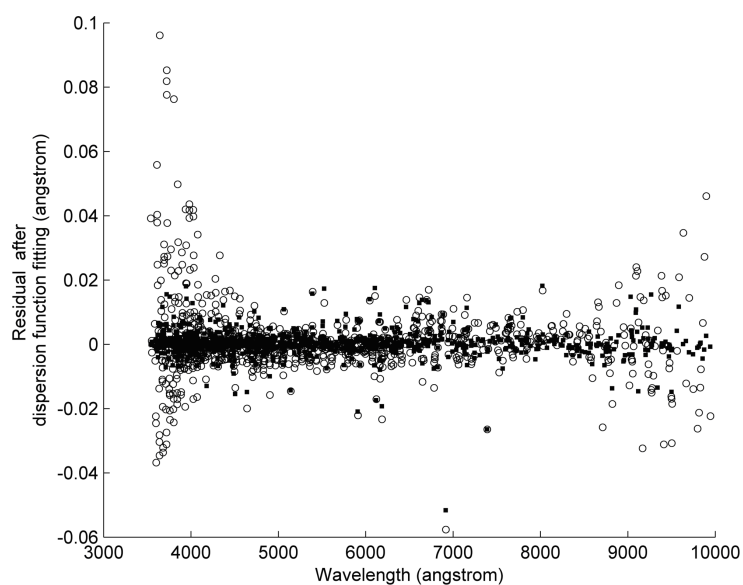


Figure 5.12: Residuals around the dispersion solutions in. Open circles are the residuals around an IRAF based polynomial, solid square points are residuals in the model based technique.

observed (Fig 5.13 bottom panel). These are the direct results of the instrument behaviour for changes in various parameters.

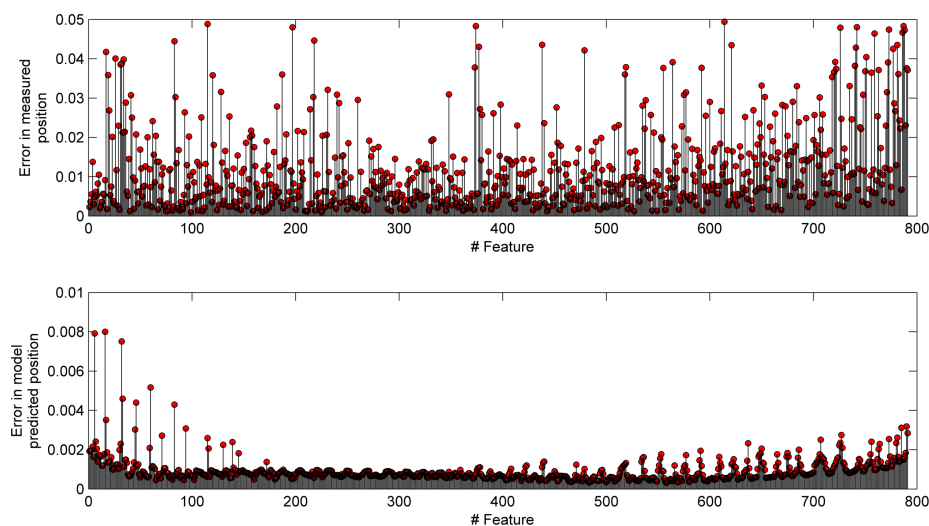


Figure 5.13: Top panel: Error in measured positions of selected features in pixel. Bottom panel: Uncertainties in the model predictions of the same features from the photon noise in the features selected for optimization. The patterns seen in the bottom panel are the result of the instrumental behaviour for changing parameters

5.3 Parameters

This subsection deals with the parameters that are optimized for constructing the model. As discussed in chapter 4, degeneracy states among the parameters are a problem. While it is hard to measure the parameters to the required accuracy, in the following we describe how the bounds for parameters are fixed. There are two steps in using the model: Initial set and optimization bounds for the open parameters 1. for system alignment, 2. during the operations. During alignment the parameters will vary to the maximum, while during regular operations they vary to a very small extent around the parameters achieved from the alignment. The alignment procedures will give an idea of how much a particular parameter can vary. For example, the opto-mechanics manufacturing tolerances can be accurate to 100micron level to the design specifications. Input optics forms the image of the fibres at the slit plate whose width and height are known, and the optics are aligned such that the images fall within the slit with proper clearance etc. Using mechanical jigs different subassemblies are placed on the optical table to a very high level of accuracy. It is also made sure that the optimized parameters never reach the bounds.

In order to understand the degenerate sets, optimization of the parameter set was carried out multiple times on same feature set. The so obtained optimized parameters were plot and observed. Fig.6.14 shows plots for few parameters. The parameters were in general varying around a mean value and the scatter around the mean value mostly dependent on the bound levels chosen for that particular parameter and other parameters that constitute the degenerate sets. Some parameters did not exhibit this behaviour as their bounds did not include the physical parameter value in the instrument. Bounds were readjusted for such parameters and re-optimized. For the later stages of optimization, the mean value of these optimized parameters is made the initial parameter set and the bounds are varied according to the devi-

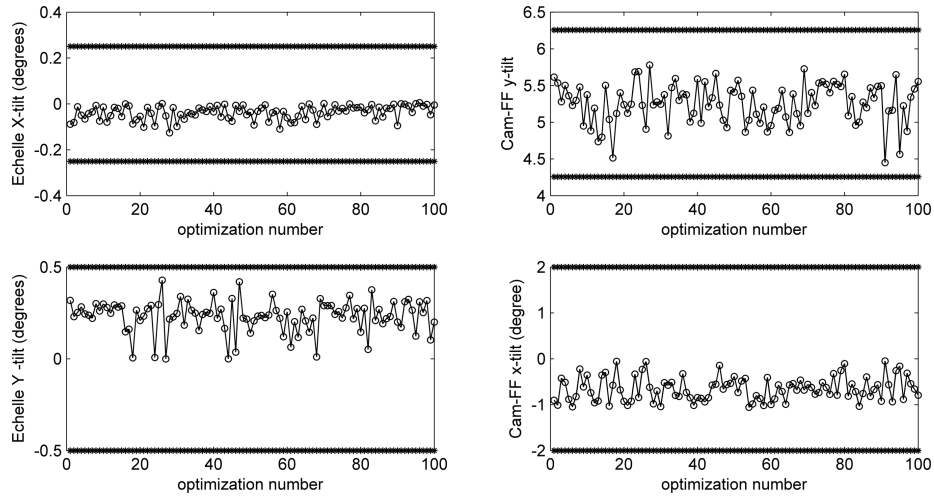


Figure 5.14: Plots show the variation in parameters (X & Y-tilts of Echelle grating, X & Y tilts of the Camera1 and Field flattener interface) over number of optimization runs on the same set of features. The bold lines in each plot shows the bounds used for respective parameters in the optimization. The degeneracy in the parameter set causes the variations over different runs. It can be observed that the parameters vary about a mean value which will form the initial parameter set during operations after the alignment.

ations. The values and bounds proved sufficient for photon noise precision tests as well.

Spectrum shift prediction

With the environment fluctuations and any vibrations at the instrument, the spectrum shifts on the CCD plane. For stellar radial velocity measurements, it is important to isolate the instrumental spectrum shifts from the stellar Doppler shifts. In order to determine the instrumental shifts, a simultaneous ThAr spectrum is recorded along with the star spectrum. The shifts in the ThAr will provide the information about the instrumental shifts. In this subsection we will understand the ability of the model to track these small shifts of the spectrum on the CCD. ThAr exposures were taken over a night to determine the instrument stability. ThAr lamp was powered ON and waited for two hours for it to stabilize. The environment are stabilised over this time period with no external disturbances, except for small natural temperature and pressure changes, which was recorded. The conventional correction relies on using the whole ThAr spectrum to determine the shift, which is a single

number over the entire spectrum or over an order. A spectrum is taken and cross correlated with a reference spectrum and the shift is calculated. Environmental effects may not necessarily cause a constant shift throughout the spectrum as they tend to have a nonlinear effect on various parameters of the instrument.

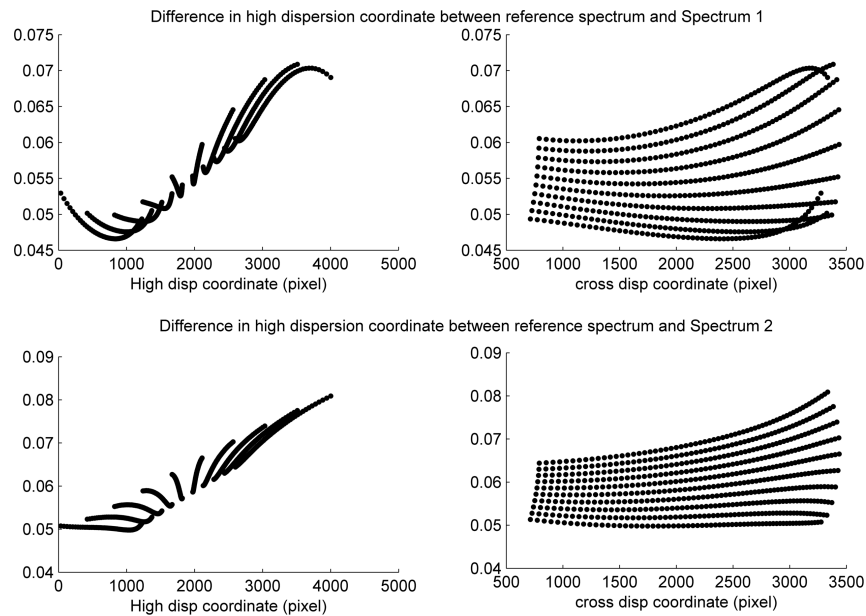


Figure 5.15: Spectrum shift predictions by model. Shift in the high dispersion direction for two different spectra with respect to a reference spectrum as predicted by the optimized model.

Model was optimized for different spectra taken at different times over night and the shift through model predictions was calculated. In Section 5.2 the noise precision of the model predictions was shown. In principle any shift greater than these precision values can be detected. Fig.6.15 shows the shifts observed across the spectrum for two different observations with respect to a reference image.

It is observed that this pattern varies from image to image slightly. In order to confirm that the effect is not due to the optimization of the parameters, multiple images were taken and few features from them were chosen and the centroids differences were observed. It is observed that the shift indeed follow the pattern within the errors as shown in Fig.6.16 as an example. The

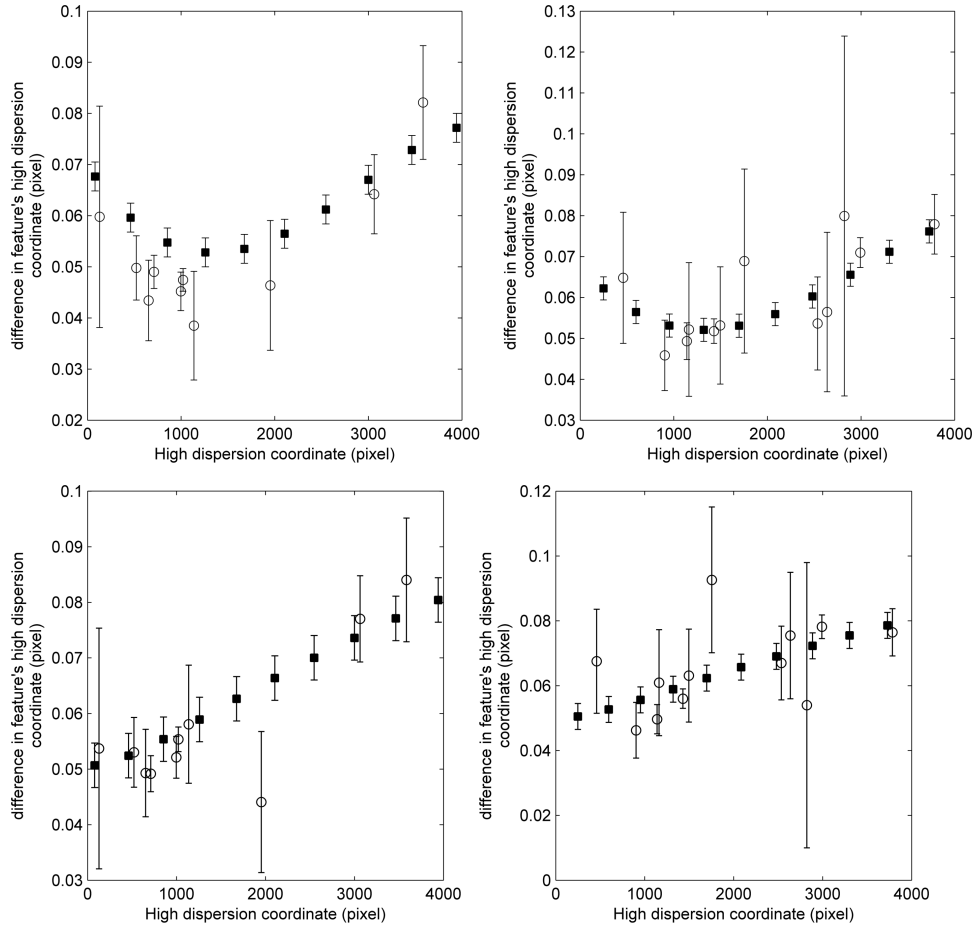


Figure 5.16: Shift in spectrum in two different orders (along columns) with respect to a reference spectrum for two different images (top) and (bottom). Solid Squares are the model predicted shifts and the open circle are the measurements from the instrument exposures. This shows a different shift patterns in the spectrum shifts in different cases and the performance of the models predictions for the same.

square marked error bar in the two plots (two different orders) show the difference in positions of equally spaced features in an order predicted by model, while the circled error bar shows measurements from spectra obtained from the instrument.

5.4 Double fiber

In the double fiber mode of operation, while one fiber is fed by star light the other is fed with the ThAr light. The purpose is to record the instrumental drift in the ThAr spectrum and use it for correction in the science object

spectrum. Two important issues in this operation are the difference in the high dispersion scale and the difference in shift between the two fibres. The slit length undergoes a curvature in the Echelle dispersion causing curved slit images on the CCD. Two fibres can be thought as a long slit, which causes an angle between the two fibres on the CCD dependent on the wavelength.

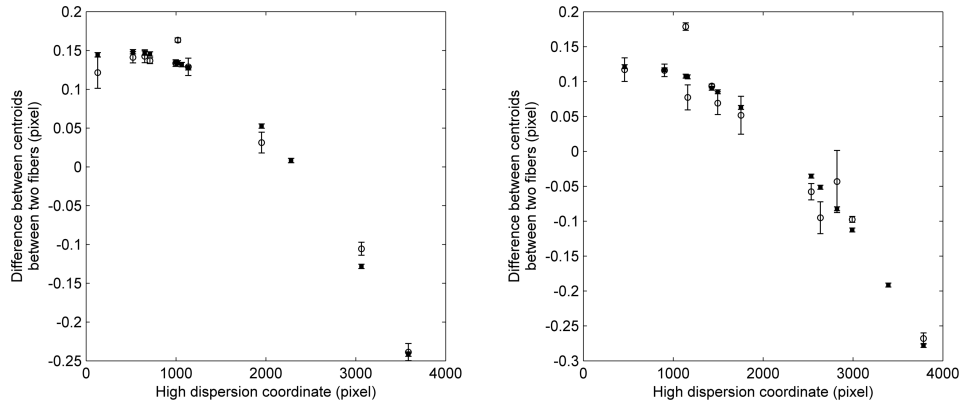


Figure 5.17: Difference in high dispersion coordinates of centroids of the two fiber images in two orders in a spectrum (left and right subplots). Solid squares represent the model predictions and the open circles are the error bars for the measurements from the CCD exposures. Model optimized using one fiber spectrum is able to track the second fiber spectrum.

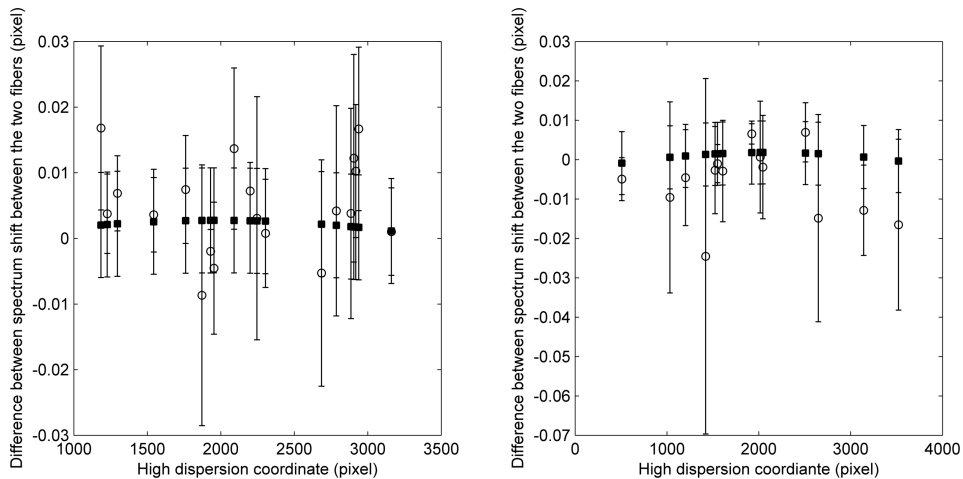


Figure 5.18: Error bars showing the difference in the spectrum shifts between the two fibres for two orders (left and right subplots). Solid squares represent model predictions and the open circles are the measurements from the CCD exposures.

To compensate for this the input slit optics were rotated a mean equal amount in the opposite direction. In order to determine the distance and angle between the two fiber images at the slit, the parameter set optimized

for one fiber is used and the decentre in x and y of the second fiber are left open and re-optimized for the second fiber features in the spectrum. The difference in high dispersion coordinates of the two fibres images at different parts of the spectrum were compared between the model predictions and features in CCD image. The angle determined by the model matched to extra angle given to the input optics. Also the difference in centroids of the same features in the two fibres was compared between the model predictions and measured from CCD images. Fig.6.17 shows an example of this difference for two different orders. It was observed that model is able to track the differences well over the entire spectrum.

In conventional data reduction and analysis, the shift in spectrum in the two fibres' channels was assumed same though there is a slight difference in the path traced by the light beam from the two. We tested the model if it can predict the difference in shift between two channels. In different orders, the difference in shift of spectrum between the two fibres was measured and compared with model predictions. Fig.6.18 shows the same for two different orders.

Chapter 6

Autoguider, Atmospheric dispersion corrector and Optical fibers for HESP

6.1 Introduction

The modelling effort in the current work is limited to the instrument setup that starts from the slit of the spectrograph to the CCD. A case of real observational setup, however will include telescope, atmospheric dispersion corrector (ADC) and additional optical path due the optical components that facilitate feeding the light into the slit of the spectrograph. Star light also passes through a variable turbulent atmosphere, which blurs and absorbs the light. In order to use the spectrograph model that was developed in this work to calibrate the real science data observed using a telescope, it is to be ensured that the fiber image at the slit, should be stable irrespective of changes in the atmosphere, telescope, fibers and optics that feeds the light to the spectrograph slit, due to changes in operational or environment condition. These changes will not be traceable based on a simultaneous reference calibra-

tion that is fed along with the stellar light to the slit as the calibration light doesn't pass through this extra path. In many spectrographs, the starlight is coupled from the telescope to the instrument using a narrow slit. However, the slit illumination varies during an observation because of the changes in seeing, focus, guiding errors or lack of atmospheric dispersion compensation. Optical fibers provide an excellent way to minimize these changes in the illumination of the spectrograph because of its natural ability to scramble light and produce a more uniform and constant output beam [49]. But the circular optical fibres are not perfect scramblers, as the light distribution at the output end retains some information of the distribution at the input end. In a real situation, tracking errors of the telescope and residuals of the atmospheric dispersion from the ADC correction together with the imperfect scrambling of the optical fibres can cause a change in the illumination of the fiber image at the slit.

As discussed in chapter 2, HESP is equipped with an autoguider to correct for tracking errors of the telescope and ADC prisms to correct for the atmospheric dispersion. In this chapter we will discuss the details of autoguider and the auto guiding algorithm and the performance of the ADC in lab setup to understand the implications of the manufactured optics. Simple lab tests were done to check for the scrambling performance of the fibres, which will be also presented in the subsections. As the instrument is not commissioned at the time this thesis was written, concrete numbers on the performance and scrambling effects at the final spectrograph were not possible. The laboratory performances are presented.

6.2 Autogider for HESP

The optical layout of the guider subsystem is presented in chapter 2. The pinhole mirror has two pinholes of diameter 250micron each, separate by 1.25mm. The star is centred on one of the pinholes and the other pinhole lets

in the sky light for background subtractions. The guider optics re-images a $100'' \times 100''$ area on the pinhole mirror onto a CCD. An Apogee Alta U47, broadband CCD which has 1024×1024 array of 13micron pixels is used for auto guiding. The image scale at the CCD plane is 66micron per arc second.

As the probability of finding a guide star is very low in a $100'' \times 100''$ field of view, it is decided to have a provision to guide on the science target itself. Once the object is centred on the pinhole, the spill-over annular outer wings of the seeing profile will be reflected towards the guider system which will be used for on-axis guiding of the star onto the pinhole, which is re-imaged on the fibers.

The pinhole size is optimized for the median seeing for a higher system efficiency. However, this will reduce the amount of spill-over light from the pinhole that is used for. Apogee Alta-U47 is with a high quantum efficiency is chosen and an accurate guiding scheme is adopted to be able to guide on a 13^{th} magnitude star at $1.3''$ seeing. The telescope beam that enters the pinhole has a focal ratio of $f/9.2$. This beam can not be coupled directly to a fiber, since several studies have shown that the multi mode optical fibres suffer focal ratio degradation. The output beam from the optical fiber is faster than the input. Fig.6.1 shows generally observed relation between the input and the output focal ratios of a fiber. An input focal ratio of $f/3.4$ - $f/3.6$ shows minimum focal ratio degradation. HESP has a relay optics that converts the input telescope $f/9.2$ beam into $f/3.6$ for feeding the optical fibres. A 100 micron fiber corresponds to 255micron diameter at the pinhole plate.

A realistic calculations for the input flux at the pinhole for various seeing conditions at the telescope was done, using the images from the telescope, using 1kx1k CCD imager and HFOSC (Hanle Faint Object Spectrograph Camera) instruments. The growth curve shown here are for the $1k \times 1k$ CCD imaging data, of the M67 field was taken during 28/12/2000. The details of the $1k \times 1k$ imager data,

1. Readout noise = 5.3 e-/pix

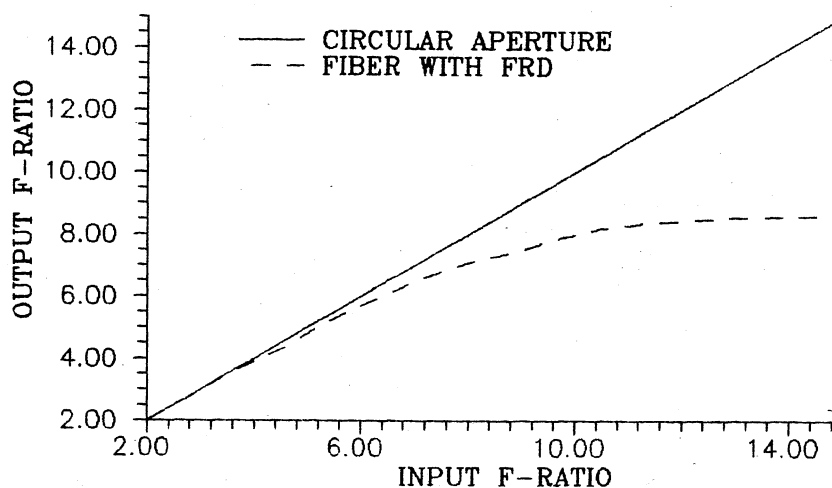


Figure 6.1: Focal ratio degradation of typical fiber is compared to the throughput of a circular aperture of the same diameter as the core of the fiber (Ramsey 1988)

2. CCD gain = 4.8 e-/ADU
3. Pixel size = 24 μ m
4. Exposure time = 10sec
5. Filter = V band

HFOSC data:

We have selected images of spectrophotometric standard stars from the HCT archive. The data covers several years with varying seeing conditions. The observations were made through U,B,V,R,I filters. The current analysis only uses the images through the V filter.

6.2.1 Aperture photometry

The analysis is based on aperture photometry within IDL and IRAF independently. The "PHOT" task within IRAF is used. The algorithms used in IDL are same as in DAOPHOT. The package includes the following errors for the instrumental magnitudes

- 1) Photon noise of the star counts

- 2) Photon noise for sky per pixel \times area
- 3) Sky variance (error in sky estimation)

We have added additional errors which were missing in the package

1. Readout noise
2. 0.1% flat field errors.

Circular aperture of various radius, 1 to 35 pixels are used to calculate the encircled energy and the growth curve. We used an annular ring of radius 35 to 45 pixels for sky estimation. Beyond 55 pixels we start to get contamination from a nearby object.

The radial profile is a simple fit based on the curfit package within IRAF, inside imexamine. The fit shows that a single Gaussian fits the core, however the wings do not match with the fit. A simple moffat profile (Fig.6.2) fits the wings reasonably well. But for accurate estimates, we used aperture photometry for the encircled energy calculation, within given radius of aperture.

A growth curve analysis for the bright stars in the centre of the CCD image was done. The magnitude difference in the successive photometric apertures is plotted against radius of the aperture in pixels. Fig.6.3 shows the growth curve, which start to flatten beyond a radius of 12 pixels. Around a radius of 15 pixels, even the effect of seeing is also gone.

Based on the prescription by Stetson (1990), we used a weighting between the error and the aperture correction to decide the 100% flux encircled radius. In Fig.6.4, we start to see that the errors becoming comparable to the aperture correction, around a radius of 12 pixels. The plot (Fig.6.5) shows the error in flux and in the magnitudes at different apertures. It shows that the error reaches a minimum value between 6-10 pixel radii. The zoomed version of the growth curve (Fig.6.4), shows that for a seeing value of 1.4", the aperture correction is less than the 2 error value at 12 pixel radius.

The analysis indicates that there is a good agreement with $1k \times 1k$ and

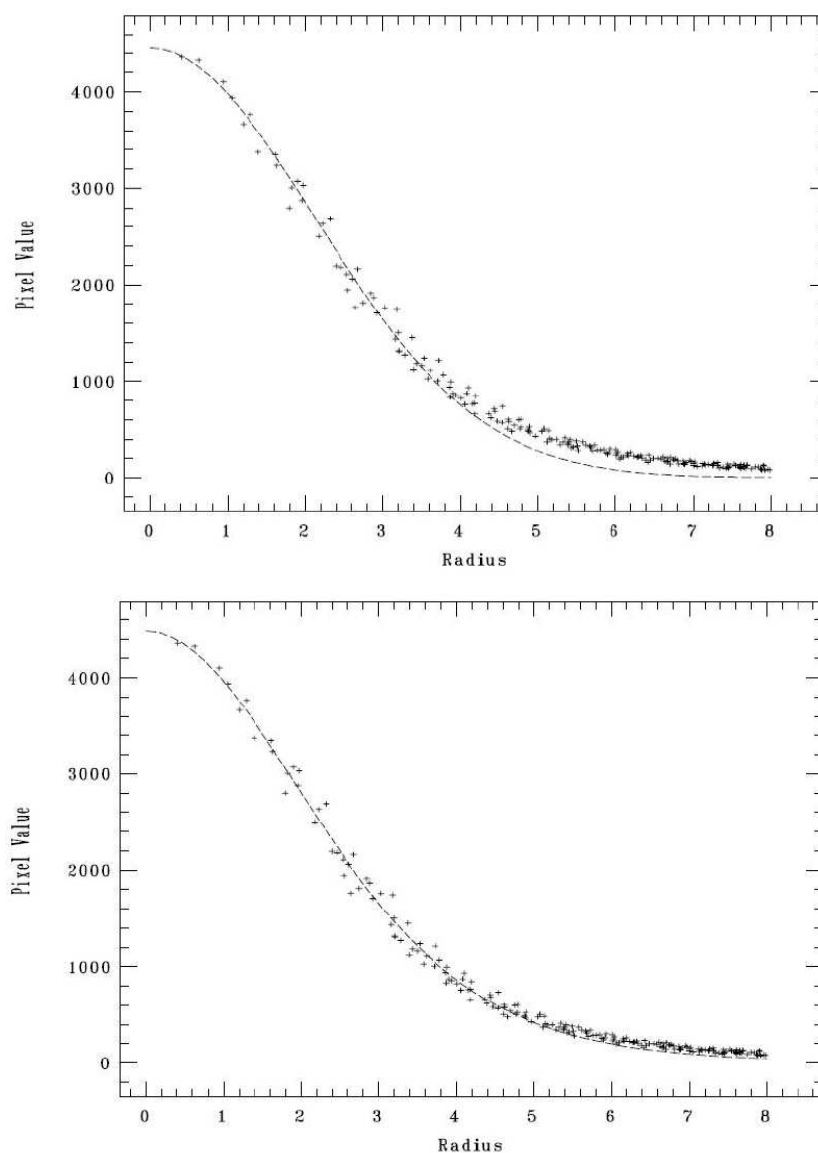


Figure 6.2: The radial profile of the image taken by $1k \times 1k$ system is shown. (top) A Gaussian profile fit is shown here. Clearly a single Gaussian profile does not fit the wings of the stellar profile (bottom) with a moffat profile fit

HFOSC data sets, also with two independent analyses of different datasets. Rough estimate of errors (mostly an underestimation), and aperture correction from growth curve analysis, we understand that,

1. The aperture correction flattens starting around 13 pixels
2. Even the effect of seeing is not seen beyond 15pixel ($4.14''$) radius.
3. A normalisation at a radius of $1.5FWHM$ of the PSF and at 15pixels gives similar encircled energy, for seeing values beyond $1.6''$.

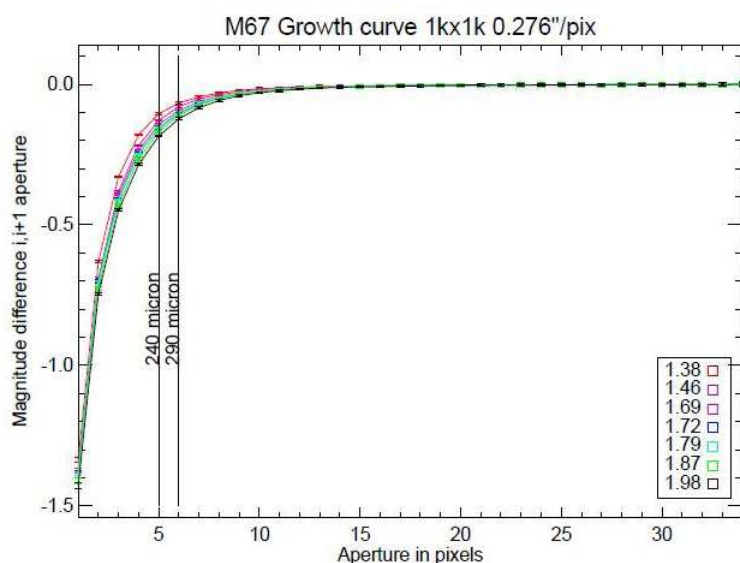


Figure 6.3: Growth curve for $1k \times 1k$ images. The x axis is the aperture radius and y axis is the difference in magnitude for the successive apertures. Different curves are for different seeing. Seeing values are between 1.38 to 1.98''

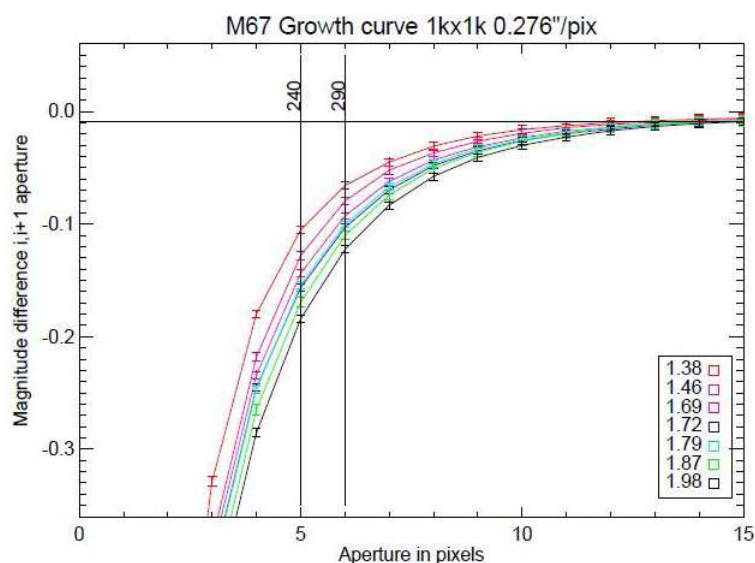


Figure 6.4: Zoomed version of Fig.6.2. Here we can clearly see that the error in the magnitudes becomes equal to aperture correction by around 11 pixels. The errors shown are 1σ values.

4. Normalisation at $1.5FWHM$ is a reasonable approximation for 100% flux, around the median seeing value of HCT.

The fraction of signal reflected towards the guider optics was measured using the aperture photometry on different images from $1k \times 1k$ camera for various seeing values to use in the simulation work for checking guiding

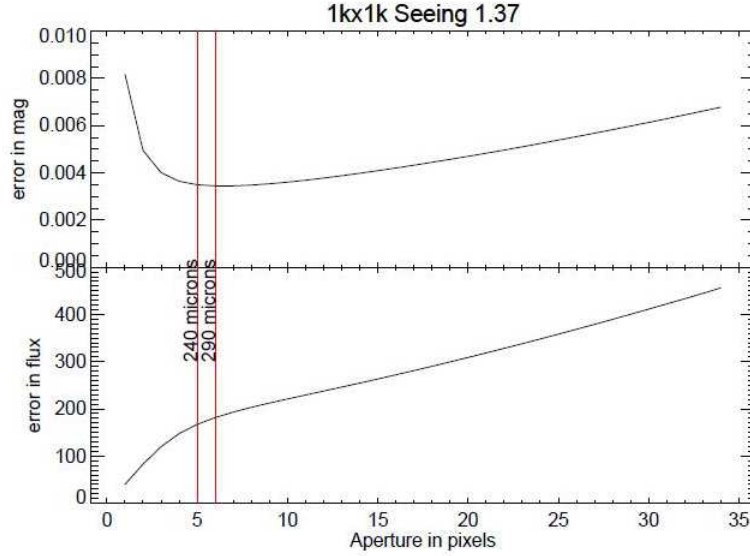


Figure 6.5: Errors in the instrumental magnitude and flux are plotted for one observation for a seeing of $1.38''$. The error is maximum close to the centre of the PSF and start to decrease as more flux from the star is added. However beyond 8 pixel radius the error again start to rise. The minimum value was

performance.

6.2.2 Simulations

Moffat function which closely fits the seeing profile is used to simulate the images at the focal plane of the telescope. Moffat profile is represented by

$$f(r) = I \left[1 + \left(\frac{r}{\alpha} \right)^2 \right]^{-\beta} \quad (6.1)$$

where r is the radial distance in the profile; α, β are constants. Moffat function is fit to the images at different seeing values obtained with the $1k \times 1k$ camera. The α, β values of these images are used to produce very fine grids of the seeing profiles at the pinhole mirror plane. An equivalent pinhole mask is introduced onto the fine grid to simulate the pinhole mirror. From the optics design file, point spread function (PSF) of the guider imaging optics is extracted. PSF and the pinhole mirror illumination were convolved along with the magnification of the optics and the image illumination on the guider system CCD plane is calculated (Fig.6.6).

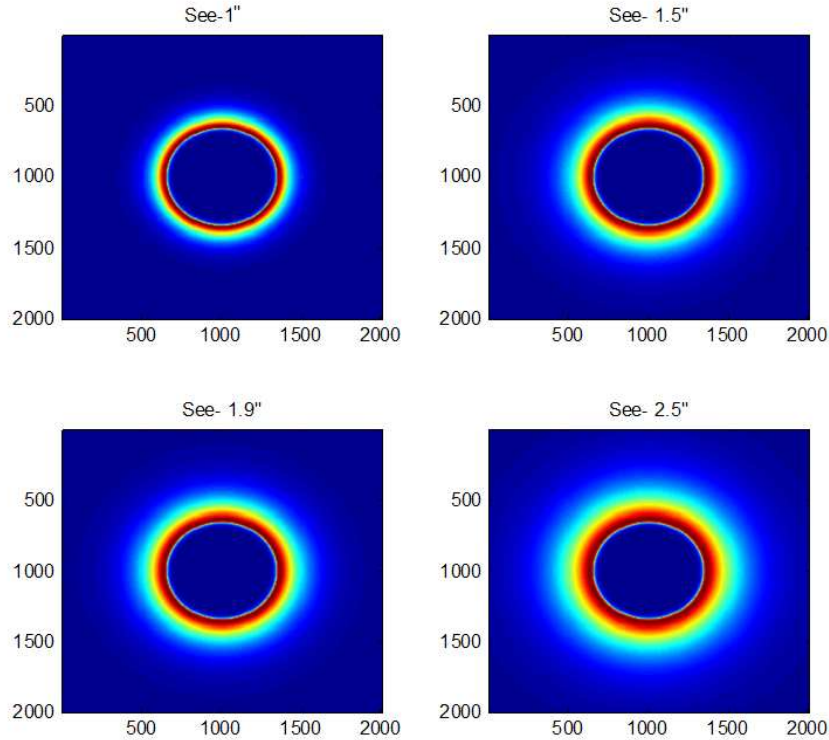


Figure 6.6: Simulated illuminations at the Apogee CCD plane of the guider system when a star is centred in the pinhole for different seeing values shown on the top of the panels. The colour indicates relative illumination in each panel

Similar images were simulated for different shifts of star in the pinhole. Fig.6.7 shows the shifted images for a 1.5" seeing. The intensities of these grids are normalised to the total intensity in the whole frame.

Given the magnitude of the star, its zenith angle and extinction coefficients at the site, exposure time, optics transmission and reflective efficiencies the total flux reaching the telescope focal plane is calculated. The fraction of flux spilling over the pinholes is calculated for given seeing using the aperture photometry described in 6.1.1. Using the transmission efficiencies of the optics from the pinhole mirror to the CCD, star flux on the CCD is determined and is multiplied with the total intensity normalised grid (Appendix B)

The flux is integrated into pixels to generate CCD images. Photon noise, sky background and CCD readout noise were added to the simulated CCD images. The simulated images were shifted for testing the centroiding algo-

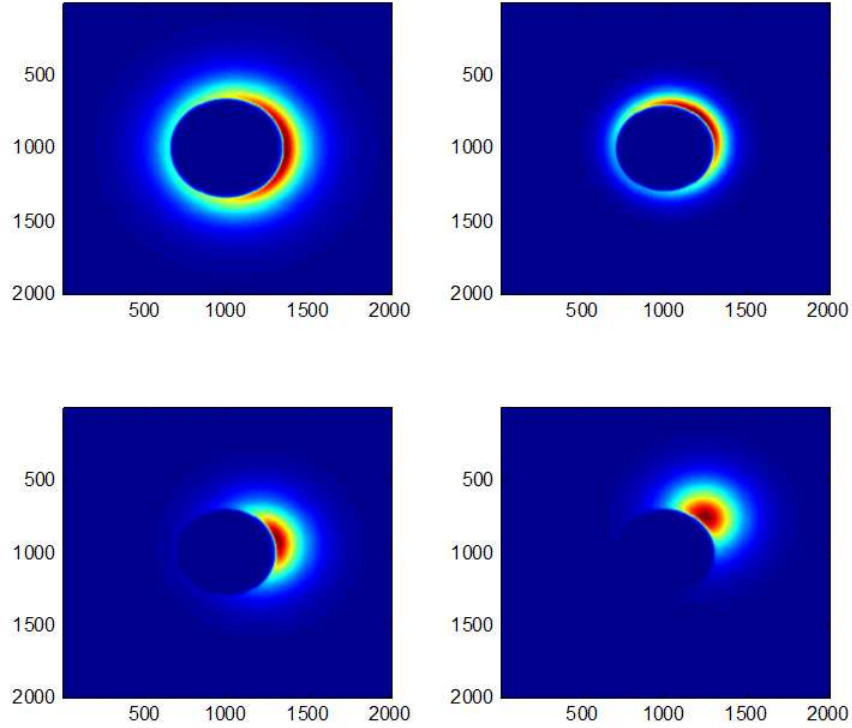


Figure 6.7: Simulated illuminations at the Apogee CCD plane of the guider system when a star is displaced in the pinhole for 1.5'' seeing. The colour indicates relative illumination in each panel

rithm. The performance of the algorithm was tested for the worst case of 1'' seeing, 12th magnitude star and 18th magnitude sky background. A 2D Gaussian function fit is used to determine the centroid. We tested procedure for 250 micron pinhole diameter. The algorithm also incorporates the fact that the telescope (HCT) has a good tracking system. The minimum correction possible with the telescope fine positioning drive is 0.2'', that corresponds to a pixel on the Apogee CCD. Regular centroiding refers to the weighted centre of gravity calculation of the image,

$$\begin{aligned}
 x_{cen} &= \frac{\sum_j \sum_i I_{ij} j}{\sum_j \sum_i I_{ij}} \\
 y_{cen} &= \frac{\sum_i \sum_j I_{ij} i}{\sum_j \sum_i I_{ij}}
 \end{aligned} \tag{6.2}$$

where, (x_{cen}, y_{cen}) is the centroid coordinate, I_{ij} is the intensity in the $(i, j)^{th}$

pixel in the 2D image. Pinhole centre position in all the frames simulated below: (23.79 23.77) pixel. (All units are in pixel unless specified). Also on the CCD frame one pixel corresponds to 0.2“.

6.2.2.1 Seeing - 1.1”: Exp.Time - 5sec

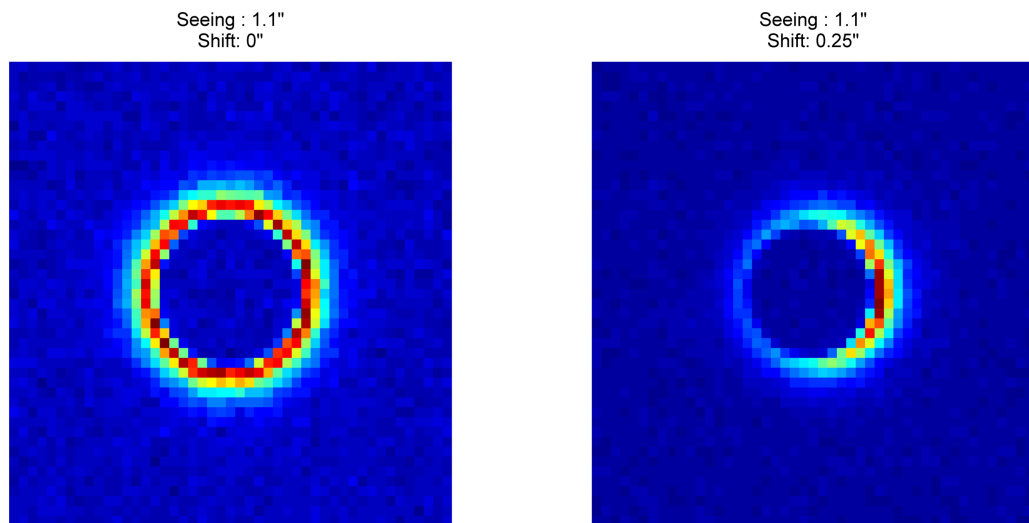


Figure 6.8: CCD images simulated for seeing=1.1” for star image left: centred in pinhole, right:displaced by 0.25”

Star image centred on pinhole: Fig.6.8 (Left panel)

Star centroid : (23.790623.7676)

Regular Centroiding : (23.904823.8927); with std. Deviation : (0.13970.1204)

2D Gauss Fit : (23.769723.7593); with std. Deviation : (0.02380.0224)

Shift in the star position by 0.25”: Fig.6.8 (Right panel)

Star centroid : (25.022823.7443)

Regular Centroiding : (28.856123.7670); with error : (0.04510.0408)

2D Gauss Fit : (25.071523.7492); with error : (0.02410.0144)

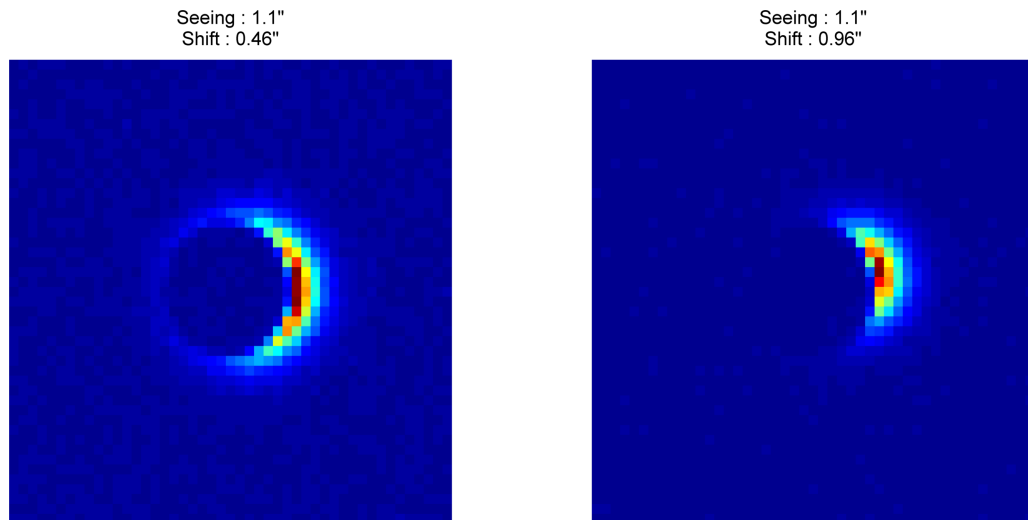


Figure 6.9: CCD images simulated for seeing=1.1" for star image leftt:displaced by 0.46", right:displaced by 0.96"

Shift in the star position by 0.4615": Fig.6.9 (Left panel)

Star centroid : (26.085023.7443)

Regular Centroiding : (30.367523.7531); with error : (0.01570.0276)

2D Gauss Fit : (25.943523.7486); with error : (0.02910.0119)

Shift in the star position by 0.9563": Fig.6.9 (Right panel)

Star centroid : (28.403022.4887)

Regular Centroiding : (31.339921.6982); with error : (0.00500.0080)

2D Gauss Fit : (28.139522.5078); with error : (0.04010.0076)

Shift in the star position by 0.4615": Fig.6.10 (Left panel)

Star centroid : (29.175622.4888)

Regular Centroiding : (31.676421.9112); with error : (0.00450.0068)

2D Gauss Fit : (28.892922.5101); with error : (0.03470.0059)

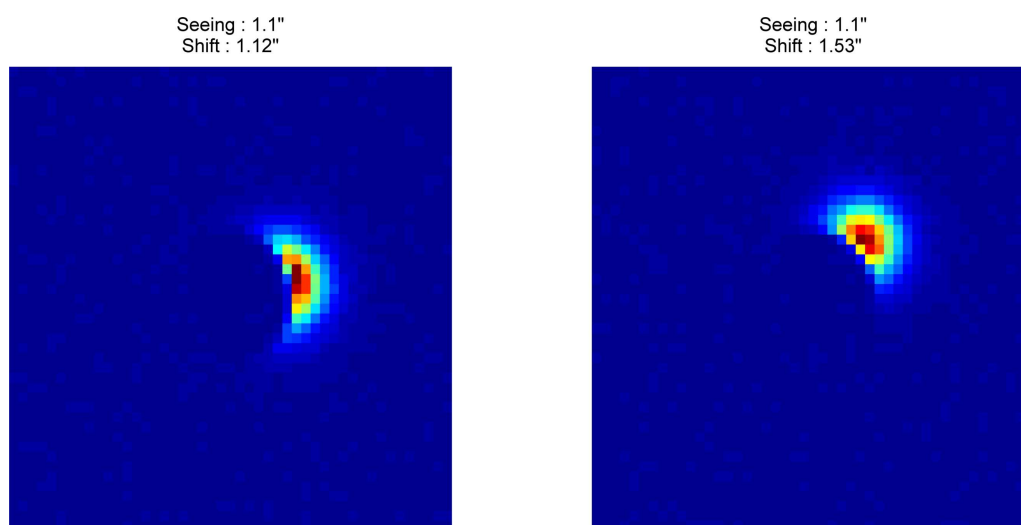


Figure 6.10: CCD images simulated for seeing=1.1'' for star image leftt:displaced by 1.12'', right:displaced by 1.53''

Shift in the star position by 0.9563'' : Fig.6.10 (Right panel)

Star centroid : (29.175718.3359)

Regular Centroiding : (30.144117.3758); with error : (0.00400.0038)

2D Gauss Fit : (29.118618.3856); with error : (0.00630.0065)

6.2.2.2 Seeing- 1.5'' : Exp.Time- 2sec

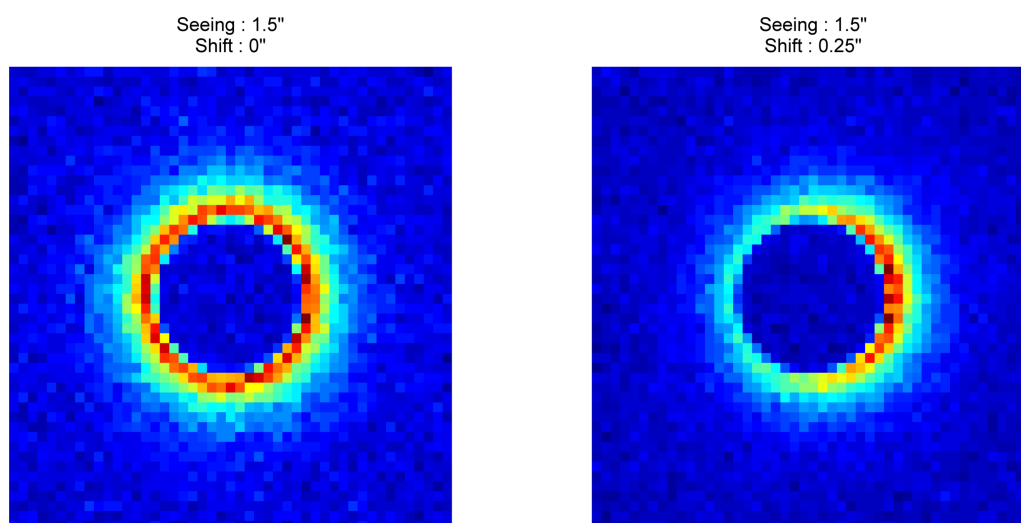


Figure 6.11: CCD images simulated for seeing=1.5'' for star image leftt:displaced by 0'', right:displaced by 0.25''

Star image centred on pinhole: Fig.6.11 (Left panel)

Star centroid : (23.790023.7670)

Regular Centroiding : (23.796923.7704); with error : (0.06830.0644)

2D Gauss Fit : (23.775523.7572); with error : (0.02870.0259)

Shift in the star position by 0.25": Fig.6.11 (Right panel)

Star centroid : (25.033323.7667)

Regular Centroiding : (27.198023.7707); with error : (0.04600.0484)

2D Gauss Fit : (25.364723.7592); with error : (0.02280.0217)

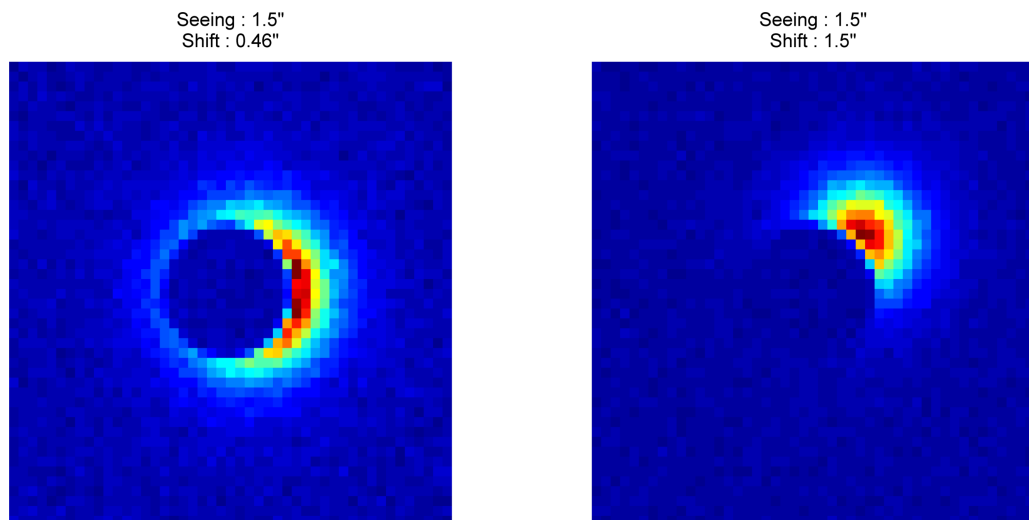


Figure 6.12: CCD images simulated for seeing=1.5" for star image left:displaced by 0.46", right:displaced by 1.5"

For shift 0.4615": Fig.6.12 (Left panel))

Star centroid : (26.252223.7434)

Regular Centroiding : (29.106323.7626); with error : (0.02560.0322)

2D Gauss Fit : (26.342023.7529); with error : (0.02010.0166)

For shift 1.5” : Fig.6.12 (right panel)

Star centroid : (29.111518.3988)

Regular Centroiding : (30.495917.0348); with error : (0.01650.0152)

2D Gauss Fit : (29.047518.4496); with error : (0.02130.0214)

From the simulations, it can be concluded that the spill-over light from the faintest magnitude star that will be observed with HESP can be guided with sufficient accuracy even at a best seeing, using a pinhole size of 250 micron and the Apogee CCD. Also it is to be noted that the flux calculated was only in the V-band. There are no colour filters included for the system and also the CCD is broadband coated which implies at the actual system more flux will be available which will also reduce the exposure time required to accumulate the flux leading to a faster guiding.

6.3 Atmospheric Dispersion Correctors

Atmosphere has a non-zero dispersion that introduces a wavelength dependent tilt to the wavefront. Zemax design that is developed for ADC, uses the model based on work by Seidelmann, Hohenkerk and Sinclair [22, 47]. The model uses six parameters: zenith angle, height from sea level, temperature, pressure, relative humidity and the latitude of the observatory. In Fig.6.13, we show the expected atmospheric dispersion observed at the HCT focal plane for selected wavelengths for the environmental conditions of Hanle.

The details ADC prisms used in HESP are described in the Chapter 2. The two prisms are counter rotated to correct for different zenith angles dispersion. As the ADCs are rotated to correct for dispersion for zenith angles from 00 to 700, the image gyrates on the focal plane shown in Fig.6.14 for various wavelengths. This is can be corrected by the HESP auto-guiding system. This is also one of the reasons for having a separate auto-guider system for

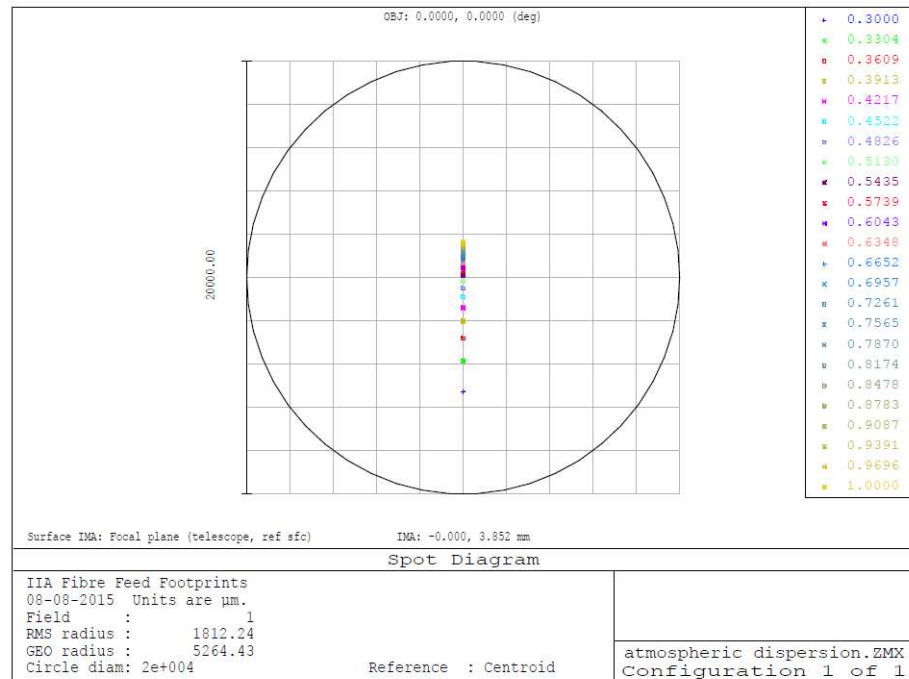


Figure 6.13: Zemax simulation of effect of atmospheric dispersion at the telescope focal plane at a zenith angle of 70 degrees for various wavelengths colour coded

HESP in spite of the telescope autoguider, AUGUS. The wedge angles of the prisms have tight tolerances.

Once the ADCs are manufactured with such tight tolerances, they need to be tested for their performance. The test results of the Atmospheric Dispersion Corrector prisms for the Hanle Echelle Spectrograph manufactured at Kiwistar Optics are presented here.

Individual ADC prisms Test: Individual ADC prisms were tested for the wedge angles. Manufactured ADC prism is placed in its rotation mount and fixed on the optical table. The prism is placed at its zero position angle. Red laser (wavelength- 632.8nm) is passed through the prism such that it is perpendicular to the first face of the prism. The laser beams centre is marked at a distance of 5.27m with and without the prism in its path. The deviation of the laser beam is noted (see Table 6.1). The same procedure is repeated with green laser (543nm) and for ADC prism2.

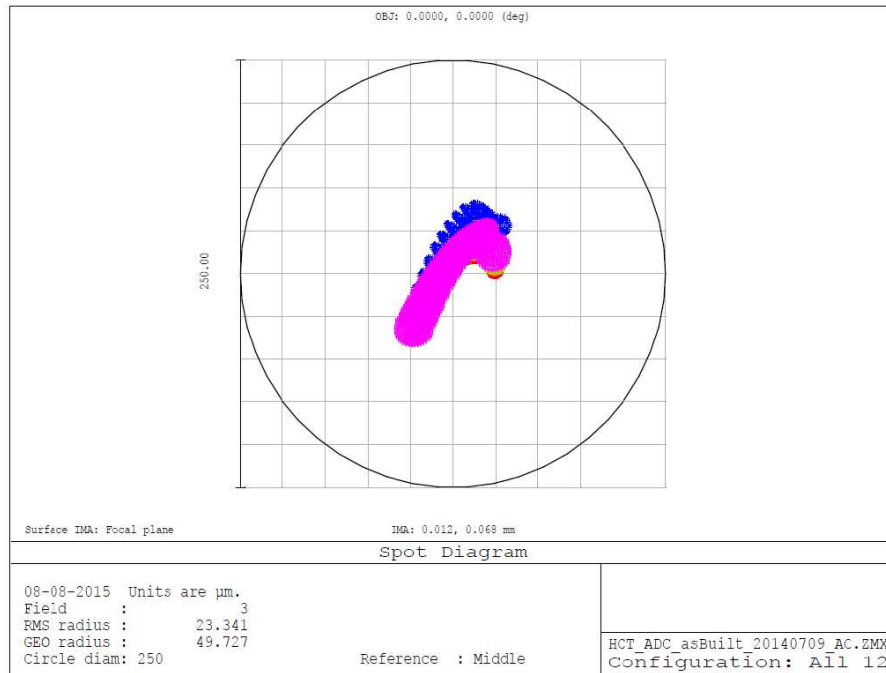


Figure 6.14: Gyration in the image at the telescope focal plane from the ADC rotation for different zenith angles. The circle around indicates the pinhole

Table 6.1: Expected and measured laser beam deviations.

	Green Laser		Red Laser	
	Expected	Measured	Expected	Measured
ADC 1	1.8mm	1.6mm	2.7mm	1.803mm
ADC 2	4.3mm	2.14mm	5.4mm	3.733mm

The physical measurements of wedge angles along with the measured deviations were used to model the ADC prisms in Zemax as manufactured. The observed angular displacement can be caused by a small angle of order of 0.05 degrees at the internal wedge of the prism in the perpendicular axis to the main wedge. This corresponds to a few tens of microns thickness difference over 25mm diameter of the prism. The so built model will be used for further analysis.

Combined ADC Prisms Test: The modelled prisms are used in the telescope system file to check for their performance which shows that for

various zenith angles (0-70) the prisms can correct for the atmospheric dispersion with typical residual dispersions at the focal plane of telescope given in Fig.6.15 for extreme wavelengths of 350nm and 1000nm. At the telescope focal plane, given the 250micron diameter pinhole, for a seeing of 1.5": the loss in flux due to the shift caused by residual dispersion of 14micron (0.156") is around 0.5%. (Moffat profile, with beta 3 - using HFOSC images)

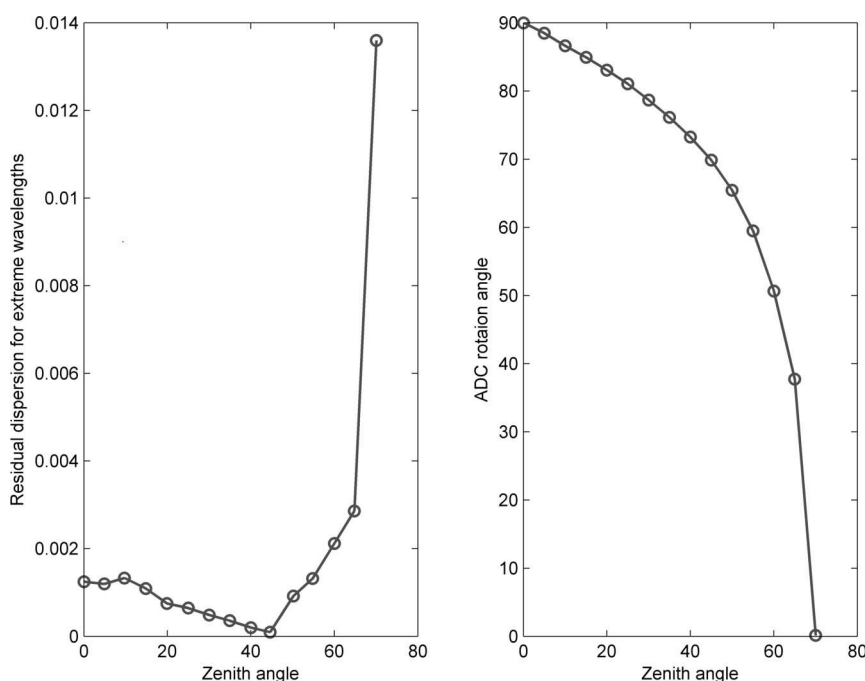


Figure 6.15: The expected residuals (left) in mm at the focal plane of the telescope for the extreme wavelengths after correcting for atmospheric dispersion using the manufactured ADCs. Right: The expected angle of rotation in degrees for the ADCs for different zenith angles

The expected residuals (left) in mm at the focal plane of the telescope for the extreme wavelengths after correcting for atmospheric dispersion using the manufactured ADCs. Right: The expected angle of rotation in degrees for the ADCs for different zenith angles.

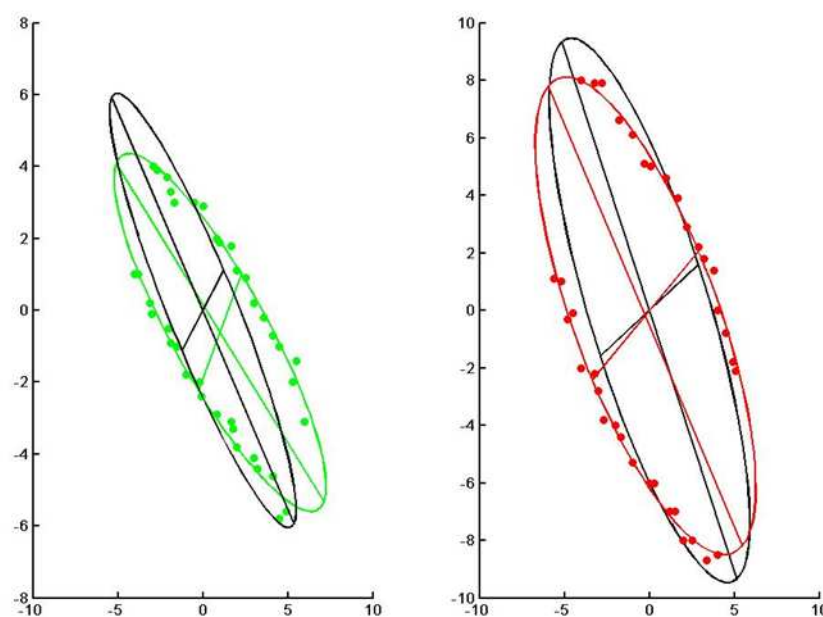


Figure 6.16: Ellipses traced from the beam deflections by rotating ADCs for two lasers (green and red). Black ellipses represent expected performance by the modelled ADCs described in text, while the coloured represents the measured deflections of the laser beam on a target at a distance 10.36m. Axes are the x and y distances in mm from the non-deflected beam position on the target obtained without ADCs in the path

6.4 Optical Fiber Scrambling

Light propagation mechanisms are well understood for an ideal fiber, the exact theory and relation between inherent fibre properties such as focal-ratio degradation (FRD) and image scrambling remain largely unknown (Lemke 2012). Circular optical fibres retain some of the input information. Movement of star image on the fiber input end changes the illumination at the output end of a circular fiber. Lab experiments were conducted in the New Zealand Measurement Standards Laboratory to check the scrambling capabilities of one of the 100 micron fiber used for HESP.

Fig.6.17 shows pictures of the lab setup. Quartz halogen lamp (not shown in the picture) passes through the monochromator and is collimated before folded twice using the mirrors to direct into the fibres (Fig.6.17(top)). An iris is used to limit the beam size to produce an F/3.6 beam. A beam splitter and

CCD arrangement is used as shown in the picture that enables to view the fiber end and the beam falling on it to use for centring the image on the fiber tip. While beam splitter allows part of light to pass, it reflects the rest of the light into a lens that focuses onto the CCD attached to the jig. The light that passes through is then focused onto the fiber end at focal ratio of 3.6 using the optics similar to the ones used in the Cassegrain unit. At the output end, shown in Fig.6.17(bottom), the fiber end which is fixed in a ferrule is held in a v-groove holder. The fiber end is re-imaged onto a CCD for measurements. At the input side the fiber was mounted in a translation stage using which the slit image on the fiber input end can be changed.

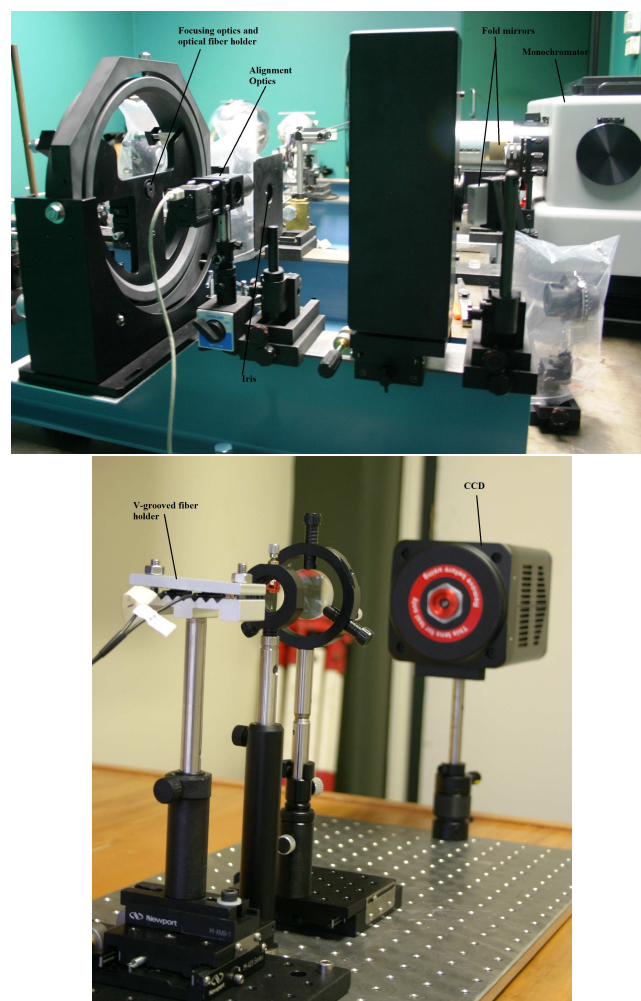


Figure 6.17: Experimental Setup for testing the image scrambling by optical fiber in the Measurement Standards Lab, Callaghan innovation (top) Lab setup used to feed the optical fiber (bottom) Re-imaging optics used to image the output end of the fiber

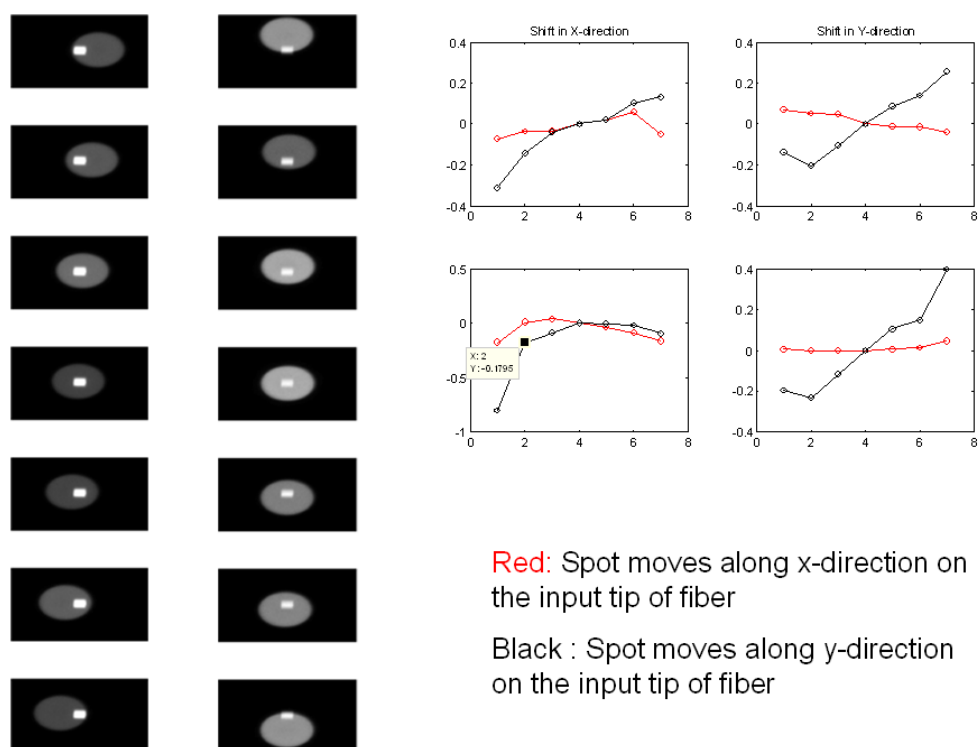


Figure 6.18: Left: Images showing the position of the slit image on the fiber input end for 14 different cases. First column shows the images when the slit image is traced in the x-direction, second column when the slit image is traced in the y-direction. Right: The shift in centroids with respect to the 4th image in each column of the images in left. First column are plots for centroid shift in x-direction and second column when the centroid shift in y-direction for two different sets of images taken. X-axis in each plot is the image number (left panel), y-axis is the relative shift measured in pixel. Red and black lines are explained in the image

Fig 6.18 shows the slit image and the fiber image on the alignment camera for various relative shifts between the two. The graphs on the right side in Fig 6.18 show the shift in the centroid at the output relative to the 4th image position shown in the left panel in pixel scale on the CCD used. Two sets of graphs are for two individual measurements. Similarly Fig 6.19 (right) shows the change in FWHMs with respect to the 4th image FWHM for the same cases as in Fig 6.18 (left). The left side images in Fig 6.19 are the illumination of the output end of the fiber for the different cases in Fig 6.18. A magnification factor is included in the results shown from the optics used to re-image the output fiber end. It is observed that with the movement of the slit image along the fiber end, the centroid at the output doesn't vary the

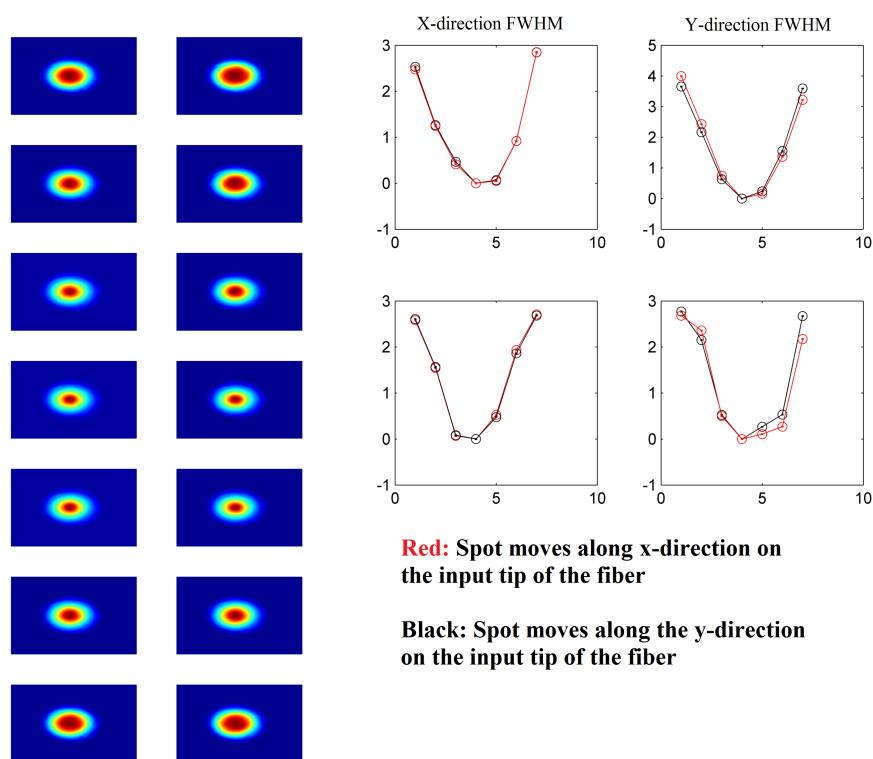


Figure 6.19: Left: Images of output illumination for the respective 14 different cases shown in Fig 6.18. First column shows the images when the slit image is traced in the x-direction, second column when the slit image is traced in the y-direction. Right: The difference in FWHM of each image with respect to the 4th image in each column of the images to the left. First column are plots for difference in x-direction FWHM and second column are difference in y-direction FWHM for two sets of images taken. X-axis in each plot is the image number (left panel), y-axis is the relative FWHM difference in pixel. Red and black lines are explained in the image

same way whether it is moved along the x-direction or y-direction. So it is not possible to generalise the centroid shift even if the image position on the input end can be estimated. Also in the spectrograph, the axis of interest is the high dispersion for precise radial velocities and so having demonstrated that the scrambling with the optical fibres is incomplete, the further work on this aspect is left for the spectrograph installation testing.

Chapter 7

Conclusion and Future Work

The main aim of the thesis work was to develop a physical model based calibration technique that can be used for precise radial velocities and chemical abundances. The work covers the theory and formulation in developing an accurate model for HESP, comparison with a commercial software and validating the model with calibration exposures taken in the lab. Even though the model was developed for HESP, the formulation was generalised to be adapted to any other high resolution spectrograph. The model traces chief rays from component to component rather than the surface to surface trace used by commercial softwares. Each component is defined by a set of parameters and functions. Realistic estimate of these parameters were obtained by matching the calibration frames from the actual instrument to the model predictions. Though there are problems with the degeneracy states in the parameters, it was observed that these states can be minimized with the proper knowledge of the manufactured components and the alignment tolerances. This work was inspired from the model based technique of the ESO group.

In the current work, we have developed an improved formulation techniques to mitigate aberration effects using component level corrections. Even with the component level corrections, we were able to obtain a good match between model prediction and the calibration. Building an accurate model is

important to understand the final behaviour of the instrument without any ambiguities, so the best possible/available values of built components were incorporated into the model parameters. Accurate values of glass catalogues, environmental parameters, and wavelength atlases were also included. We also identified methods to notice any discrepancies in the glass catalogues used in the model. While an accurate measurement of glass parameters is possible from the vendors, we have shown that an inaccurate glass data can not be a limitation to model the spectrograph.

In Chapter 5, we show the test results of the model with the ThAr calibration frames obtained during the instrument pre-shipment at the Kiwistar Optics labs. The starting model based on the design parameter matched well with that of the commercial ray trace software, Zemax at a level of few tens of nanometres. Various parameters in this model were changed to match with the calibration ThAr exposure to obtain an optimized final model. The ThAr features used for matching spread over the entire wavelength range of the spectrograph and had at least 1-4 features per each Echelle order. The optimized model was used to predict the line positions of several test features across the spectrum.. Except for few outliers the mean and standard deviation of the residuals from this test are 0.000957 pixel and 0.04pixel respectively, along the Echelle direction and even better in the cross dispersion direction. The dispersion solution of the model was compared with the 2D polynomial dispersion function from IRAF. The residual of the model fit was ten times better than the empirical fit using IRAF. The noisy data and varying efficiency of the instrument from red to blue region has minor effect on the model based dispersion solution, compared to the empirical fit.

Accurate wavelength solution covering the entire wavelength range is very important to be used as a reference for the long term stability of spectrographs like HESP that uses double fiber technique. The model based calibration technique works well in regimes where there are fewer calibration lines and an empirical calibration is less accurate. This is especially useful for the radial

velocity studies of M-dwarf, that has photospheric lines mainly in the red region and usable ThAr lines in this region is limited. M-dwarfs are interesting for the better detectability of earth like planets with current instruments. The model based technique has a large potential to study several systematic effects that can improve long term stability. Radial velocities up to 1m/s and a short-term stability of 20cm/s are already achieved from HARPS-like instruments operating from 400-670nm. There are several new initiatives towards precise velocities using NIR spectrographs. Model based calibration can be used to extend the accurate empirical calibration in the 400-670nm to the redder wavelengths and will help to compare the optical and NIR systems and place them in a similar reference standards.

Accurate wavelength calibration using model especially in blue and red regions of visible wavelength will help in accurate abundances. Since most of the heavy element which occur in the blue and the line features are broadened due to isotopic shifts and hyperfine structures. Most high resolution spectrographs also use image slicers for high throughput. These spectrographs also have typically 2-pixel sampling. During a 1D spectral extraction, the pixels along the slit length are added to achieve high S/N. The procedure assumes the added pixels have same wavelength. However any tilt along the spatial direction will have cross talk and the isotopic abundances derived from such extraction will be inaccurate. A model can give a complete 2D wavelength map of the detector that will help in accurate extraction, hence accurate abundances. In the red region of the optical there are several telluric absorption lines and sky emission lines. Accurate sky subtraction and telluric lines removal is needed to derive accurate abundances of some of the important stellar atomic lines, (e.g. HeI, Cl, NI, OI, KI and SI). Accurate removal of sky lines and telluric lines need good wavelength calibration.

It is also observed that for the mean average instrumental shift derived in a spectrum, shift across the spectrum. The model was able to predict these patterns. This sort of information can be useful in applying position/wavelength

dependent instrumental drift corrections and also extending the drift corrections to areas where the calibration lines are sparse and weak. For double fiber observations, model was able to track the difference in the centroids between the two fiber images across the spectrum. The model was optimized for only one fiber at a time, but yet it was able to track the centroid differences which is varying across the spectrum which is an indication that the optimized model can map the slit position onto the CCD plane. Using this, an efficient 1D extraction of the spectrum can be performed for varying slit image tilts.

We also explored, if the model is able to predict the difference in the instrumental shifts between the two fibres. The mean values of these differences matched with the mean values calculated from the model and also the difference in shifts between the fibres varied over the spectrum. The double fiber, simultaneous referencing method relies on the assumption that the reference calibration tracks any changes to the object spectrum. The difference between the object and the reference fiber is assumed to be a simple, mean instrument drift that can be added to the dispersion relation derived at the beginning of the night. In real case, the instrument drift is a function of position and wavelength. In the future instruments ,when we are not limited due to number of photons, the positional dependence of instrument drift will play an important role. Model based calibration can advantage of the entire wavelength coverage of the spectrograph, for precise radial velocities. Accurate wavelength shift between fibers also helps in accurate sky subtraction, especially beyond 600nm where there are sky emission lines due to O₂, H₂O. Sky fibers are used to remove the contribution due to these lines. In accurate determination of instrument drift between the two fibers, especially the wavelength dependency will result in inaccurate line strengths and chemical abundances. Sulphur is one such important element, which occurs in the crowded regions of telluric and skylines. Sulphur lines are very important, since it is one of the heavy alpha element that is not affected due to dust

depletion. Hence, Sulphur is a better indicator to study the planet frequency and metallicity correlation of the host stars, since sulphur probes the metallicity of primordial cloud. Similarly, the chemical abundances comparison of old metal poor stars and the high redshift inter-galactic medium are more meaningful for volatile elements like C,N,O and S , that are less affected by dust in the high redshift intergalactic medium. These lines occur in the red region from 700-1000nm, which is severely affected by sky and telluric lines.

Future Work

The optimization routine, simulated annealing, used in this work was a very basic implementation of the algorithm, there is scope for improvement of the algorithm in the future. The optimization did not consider any weights to the parameters, the merit function was a simple weighted mean of squares of errors minimization. Since we are dealing with physical parameters of a real existing instrument, the effect of various parameters on the output can be studied quite well. An improved merit function which takes into account the residuals that is a function of more parameters along with a appropriate weights and a customised annealing procedures for different parameters based on the knowledge of the instrument behaviour can give a greater control.

The next task is to incorporate the model into the data pipeline and apply it to calibrate the science data, either replacing or complementing the empirical wavelength calibration. Model will be also used for accurate extraction of the 1D spectra. Since, each calibration will give a set of physical parameters that defines the instrument, it is ideal to study any trending, that will help to improve the long-term stability of the instrument. Observing several standard sources as part of regular observations will help improve and validate the performance of the model. We propose on position based drift corrections for spectrographs that cover a wider wave length band, which will need a different approach of applying the corrections to the science data unlike the

present method where an equivalent RV corresponding to instrumental drift is measured and subtracted from the measured RV in the star spectrum. This will either require a method to change the x-axis scale of the extracted 1D spectrum using the shift predictions from the model or using the model to predict the wavelength dispersion in science spectra using the simultaneous reference spectrum.

There is a lot of scope for improvements and additional features in the modelling methodology used, e.g. ways to mitigate degenerate states and obtaining the exact parameters of the instrument, developing on the optimization routine, efficient 2D profile fits to the wavelength features for better centroid measurements [35].

Complementing the wavelengths prediction model with throughput and accurate detector models, 2D spectrograph exposures in realistic execution times can be simulated. Modelling optical fibres for the scrambling properties will be a great addition to the technique. Another area to explore is decoupling the instrumental drifts and guiding and incomplete scrambling of optical fiber induced drifts using few stable atmospheric absorptions line in the stellar spectra recorded. With the capability of model to predict position dependent instrumental drift, the shifts in few stable atmospheric lines can be used to separate instrumental and telescope guiding drifts.

Credits and Contributions

An instrument, especially similar to HESP, can not be developed by one individual. It is a team effort. In the current report, wherever contributions from others, especially from KiwiStar Optics on the design, setup, drawings are used, it is explicitly mentioned in the text. My contribution is the development and validation of the model based calibration technique for HESP and the work presented in chapter 6. The modelling work can not have happened without the instrument design and the built final instrument. The design and

fabrication of the instrument is by KiwiStar Optics, New Zealand.

List of Publications

1. *Modelling high resolution Echelle spectrographs for calibrations: Hanle Echelle spectrograph, a case study*, **Chanumolu, Anantha**, Jones, Damien, Thirupathi, Sivarani, 2015, *Experimental Astronomy*, **39**, 423 – 443.

Appendix A

Table 1: 550 Features' wavelengths and orders used for model optimization

Wave length (nm)	Order no.		
0.983611888500000	35	0.842353942400000	41
0.982914341900000	35	0.842031133000000	41
0.981538775300000	35	0.841903976700000	41
0.974913506200000	35	0.836102257000000	41
0.970322287200000	35	0.833273903300000	41
0.966734834000000	36	0.832314248000000	41
0.963528521000000	36	0.825466215000000	42
0.956386725000000	36	0.818916233500000	42
0.949979367800000	36	0.817203292000000	42
0.949810223200000	36	0.816197130000000	42
0.947747800700000	36	0.814537714200000	42
0.947327944900000	36	0.813164057400000	42
0.946979209000000	36	0.809584950500000	43
0.946362274600000	36	0.803240878800000	43
0.940166725500000	37	0.802440800000000	43
0.938584606000000	37	0.798116773300000	43
0.934326755000000	37	0.797478877000000	43
0.929211095000000	37	0.794391055000000	43
0.927881807600000	37	0.788845261400000	44
0.926874913100000	37	0.786813409000000	44
0.920648702800000	37	0.784969846600000	44
0.909732468700000	38	0.784394860000000	44
0.906644740000000	38	0.784245515000000	44
0.905073335000000	38	0.781992100100000	44
0.901906503000000	38	0.780050357000000	44
0.897010183700000	38	0.779107743000000	44
0.889542768000000	39	0.777408464000000	44
0.887126814000000	39	0.773107800900000	45
0.884361064000000	39	0.771239102200000	45
0.882284313000000	39	0.768742260000000	45
0.877798283000000	39	0.768023976000000	45
0.877521423000000	39	0.765593497000000	45
0.876064838000000	39	0.765442642200000	45
0.875043316200000	39	0.764948430600000	45
0.871162596000000	40	0.763241083000000	45
0.866786545600000	40	0.762927419600000	45
0.864181478000000	40	0.762780436000000	45
0.857547559200000	40	0.760991716200000	45
0.855729412500000	40	0.758788019800000	45
0.854213909800000	40	0.758788019800000	45
0.848068735100000	41	0.756982509000000	45
0.844883244600000	41	0.755139217000000	46
0.844780772400000	41	0.752757982000000	46
		0.748341458000000	46
		0.743098640200000	46
		0.742059305600000	46
		0.740429096700000	46
		0.734317394000000	47
		0.733030389500000	47
		0.728691039500000	47

0.722114076800000	48	0.659330490000000	52
0.722004340000000	48	0.659300019900000	52
0.721467738000000	48	0.659035926800000	52
0.720999275500000	48	0.658572430400000	52
0.720846902200000	48	0.657903116300000	52
0.720202962800000	48	0.653314610600000	53
0.717534957000000	48	0.651084863700000	53
0.716192072000000	48	0.650878486000000	53
0.715889588300000	48	0.649499144000000	53
0.715889588300000	48	0.649253054900000	53
0.715225534000000	48	0.646439895000000	53
0.715052933000000	48	0.645906689600000	53
0.712652450500000	48	0.641538722000000	54
0.706639940000000	49	0.641367134300000	54
0.706260061400000	49	0.640821688100000	54
0.706198804000000	49	0.638916126000000	54
0.704773998000000	49	0.637869341300000	54
0.703822334000000	49	0.637370511500000	54
0.702050294100000	49	0.637090005000000	54
0.699496563000000	49	0.635766802800000	54
0.699158294000000	49	0.635049276600000	54
0.694740600800000	50	0.634461322900000	54
0.694552578900000	50	0.633937252800000	54
0.691803672100000	50	0.632902723500000	54
0.691175573000000	50	0.632811616000000	54
0.688830812000000	50	0.631255542000000	55
0.687664963300000	50	0.629498280000000	55
0.687034596000000	50	0.629293133000000	55
0.686865804000000	50	0.628090350000000	55
0.683091982100000	50	0.627897468000000	55
0.682656071000000	50	0.627585200000000	55
0.679310936200000	51	0.626315068300000	55
0.679071388000000	51	0.626279596000000	55
0.678228438800000	51	0.625915445900000	55
0.678199641000000	51	0.624267989100000	55
0.675831764000000	51	0.623658004100000	55
0.672931538200000	51	0.622809215700000	55
0.672105435000000	51	0.622624913000000	55
0.671582341400000	51	0.620893736600000	55
0.668055049900000	52	0.620520876000000	55
0.667653978000000	52	0.619993755000000	56
0.666410811800000	52	0.619361848400000	56
0.666051605000000	52	0.618983727700000	56
0.664648557000000	52	0.618433235900000	56
0.664074526000000	52	0.618241515000000	56
0.661519962900000	52	0.618014104300000	56
0.661519962900000	52	0.617152931100000	56
0.660724073000000	52	0.616618534000000	56
0.659576027800000	52	0.616305840000000	56
0.659528396000000	52	0.615879167500000	56

0.615728443100000	56	0.583398734000000	59
0.615369538000000	56	0.581703419000000	59
0.612617565600000	56	0.580575038800000	59
0.611452957000000	56	0.580243792600000	59
0.610627221000000	56	0.579125040800000	59
0.610627221000000	56	0.577554745400000	60
0.610341406000000	56	0.576978079300000	60
0.608971578500000	57	0.576512728300000	60
0.608090570300000	57	0.575138077700000	60
0.608010410000000	57	0.575098296000000	60
0.607955547000000	57	0.575033545100000	60
0.607878818200000	57	0.574367644000000	60
0.607478504000000	57	0.574342146300000	60
0.607070088000000	57	0.572697664400000	60
0.605505687600000	57	0.572176951200000	60
0.605072585600000	57	0.572120917100000	60
0.604610643000000	57	0.570868669000000	60
0.604035254000000	57	0.570249928000000	60
0.603936927900000	57	0.565949551000000	61
0.603211483300000	57	0.565055882600000	61
0.602270305500000	57	0.564131166000000	61
0.601182490200000	57	0.561687835500000	61
0.600873581400000	57	0.561362600900000	61
0.600682810600000	57	0.561223871000000	61
0.600286534100000	57	0.560315827300000	61
0.599578886900000	57	0.558857770100000	62
0.599266639500000	57	0.558090761300000	62
0.599070362000000	57	0.557775306100000	62
0.597671989900000	58	0.557490121700000	62
0.597531941100000	58	0.556574656000000	62
0.594629428200000	58	0.556143526500000	62
0.594047049300000	58	0.555858886900000	62
0.594010216000000	58	0.554971682500000	62
0.593930850900000	58	0.554442959700000	62
0.593157728000000	58	0.554144928000000	62
0.592787398900000	58	0.554080028000000	62
0.592704527200000	58	0.551640494700000	62
0.592058468900000	58	0.550583108000000	63
0.591630972900000	58	0.550078300400000	63
0.591630972900000	58	0.549766385100000	63
0.591602461000000	58	0.549585706000000	63
0.591286768000000	58	0.549473017500000	63
0.591056283000000	58	0.549416941000000	63
0.590720710000000	58	0.546048457000000	63
0.589308365600000	58	0.545373390600000	63
0.588733272300000	58	0.544866756000000	63
0.586534355800000	59	0.543262144400000	63
0.585574322000000	59	0.541899174000000	64
0.585509711600000	59	0.540915690600000	64
0.585430321500000	59	0.540067550000000	64

0.540042314000000	64	0.504612615700000	68
0.539626057300000	64	0.504063552500000	68
0.539407201000000	64	0.503005798000000	68
0.537684723000000	64	0.502120619300000	69
0.537094016100000	64	0.500349240900000	69
0.536164060800000	64	0.498676326500000	69
0.534506744900000	64	0.498387750500000	69
0.532845751200000	65	0.494683880400000	70
0.531438247600000	65	0.494444365900000	70
0.531400682900000	65	0.494102080400000	70
0.530199806000000	65	0.493920777000000	70
0.529921709900000	65	0.493815321000000	70
0.529587022800000	65	0.492915592400000	70
0.528253832400000	65	0.492139045100000	70
0.527558644400000	65	0.492118931400000	70
0.526817597300000	65	0.491152855100000	70
0.525982380100000	65	0.490342316300000	70
0.524911532000000	66	0.489632180100000	70
0.524101061400000	66	0.488009557600000	71
0.523261585400000	66	0.487572576000000	71
0.522056300400000	66	0.487427784900000	71
0.521480081900000	66	0.487264976800000	71
0.521268132600000	66	0.486683653700000	71
0.520061158800000	66	0.486452256000000	71
0.520061158800000	66	0.486452256000000	71
0.519726051900000	66	0.486452256000000	71
0.517840297800000	66	0.486257453000000	71
0.516489668400000	67	0.485179461000000	71
0.516297733100000	67	0.484971698900000	71
0.516004116500000	67	0.484219529500000	71
0.515567882300000	67	0.483415302000000	71
0.515304696600000	67	0.483294768900000	71
0.514964579000000	67	0.483247122700000	71
0.514470018000000	67	0.482804916800000	71
0.514220580000000	67	0.482495436000000	71
0.513617656000000	67	0.482420253400000	71
0.512737857100000	67	0.482223160000000	71
0.511647002700000	67	0.481095829000000	72
0.509790521400000	68	0.480947754500000	72
0.506938666200000	68	0.479072563200000	72
0.506754802800000	68	0.478848619000000	72
0.506660463000000	68	0.477962980500000	72
0.506635740400000	68	0.477558620000000	72
0.506601398200000	68	0.476793326900000	72
0.506127166000000	68	0.474228451300000	73
0.505675685000000	68	0.474185515000000	73
0.505329720000000	68	0.474100201000000	73
0.505219248300000	68	0.473045111400000	73
0.505120412000000	68	0.472510501000000	73
0.504845076500000	68	0.472475959400000	73

0.472259738100000	73	0.434366486600000	79
0.471380000000000	73	0.433849667800000	79
0.470530601200000	73	0.432134127000000	80
0.469635195800000	73	0.431963025000000	80
0.469540506000000	73	0.431646786100000	80
0.468750612600000	73	0.431421103800000	80
0.467736440500000	74	0.431421103800000	80
0.467496915500000	74	0.430838757000000	80
0.467129150600000	74	0.430104882000000	80
0.466810484000000	74	0.428324614000000	80
0.466782219900000	74	0.427456002000000	81
0.466450806900000	74	0.425869457400000	81
0.464855220600000	74	0.425745174000000	81
0.463998378700000	74	0.425151104500000	81
0.459670819100000	75	0.425151104500000	81
0.459395286900000	75	0.423665610900000	81
0.458971181000000	75	0.422791582000000	81
0.457225325500000	75	0.421601557900000	82
0.455708970700000	76	0.421425391000000	82
0.455708970700000	76	0.421210924100000	82
0.454719012800000	76	0.421007623000000	82
0.454227211400000	76	0.417170874200000	82
0.453652624000000	76	0.416694043100000	83
0.453158944000000	76	0.414386920000000	83
0.452246172400000	76	0.411787508000000	84
0.451638452000000	76	0.411692010000000	84
0.449459422400000	77	0.411391477600000	84
0.448994016000000	77	0.410957910000000	84
0.448875445000000	77	0.410149840800000	84
0.448815610900000	77	0.409890367100000	84
0.448342677100000	77	0.409590267000000	84
0.448208631000000	77	0.408767399000000	84
0.447647715200000	77	0.407035041000000	85
0.446277990000000	77	0.406455446000000	85
0.445925278000000	77	0.406039920000000	85
0.445381526900000	77	0.405467251000000	85
0.444714917200000	77	0.404453697000000	85
0.441572609000000	78	0.403718803600000	85
0.441012104300000	78	0.403198125400000	85
0.440416376800000	78	0.402026473000000	86
0.440281747800000	78	0.401362925700000	86
0.439234406000000	78	0.401019059000000	86
0.438309124000000	79	0.400934321600000	86
0.437940698400000	79	0.399567879000000	86
0.437535290100000	79	0.396851453000000	87
0.437110364300000	79	0.395151311000000	87
0.436715697000000	79	0.395008141000000	87
0.435467225800000	79	0.394914774400000	87
0.435029465300000	79	0.393402449100000	87
0.434765848000000	79	0.392620467000000	88

0.392551208000000	88
0.392491048600000	88
0.391837876000000	88
0.391752659300000	88
0.391024602000000	88
0.390420788000000	88
0.390276719000000	88
0.390198334000000	88
0.388801728600000	89
0.388074355000000	89
0.387976111000000	89
0.387674453000000	89
0.387596010000000	89
0.387534184000000	89
0.387492023000000	89
0.387424553800000	89
0.387076015000000	89
0.386450095000000	89
0.385560377000000	89
0.385322757000000	89
0.384304979000000	90
0.384188973000000	90
0.383896368100000	90
0.383114710000000	90
0.382947076600000	90
0.382745455000000	90
0.382415235000000	90
0.382187656000000	90
0.381976903000000	90
0.381414969000000	90
0.381053564000000	90
0.380252235000000	91
0.379187135000000	91
0.378437079000000	91
0.377734362000000	91
0.377244204100000	91
0.377112687000000	91
0.375953502000000	92
0.375876208000000	92
0.375627924000000	92
0.375565991000000	92
0.375363530000000	92
0.375208786600000	92
0.375155973000000	92
0.374703521000000	92
0.374398732000000	92
0.374224653000000	92
0.373857493000000	92
0.372896276000000	92
0.372049252400000	93

0.370782171000000	93
0.370428350800000	93
0.370203129300000	93
0.367661398000000	94
0.366424587100000	94
0.365773542000000	94
0.361345757100000	95
0.359914642500000	96

Table 2: Final 233 features used for model Optimization

Wave length (nm)	Order no.		
0.983611888500000	35	0.733030389500000	47
0.982914341900000	35	0.728691039500000	47
0.981538775300000	35	0.722114076800000	48
0.974913506200000	35	0.720999275500000	48
0.966734834000000	36	0.720202962800000	48
0.949810223200000	36	0.712652450500000	48
0.947327944900000	36	0.706639940000000	49
0.946362274600000	36	0.706198804000000	49
0.940166725500000	37	0.703822334000000	49
0.938584606000000	37	0.699158294000000	49
0.927881807600000	37	0.694552578900000	50
0.920648702800000	37	0.687034596000000	50
0.906644740000000	38	0.683091982100000	50
0.905073335000000	38	0.682656071000000	50
0.901906503000000	38	0.679310936200000	51
0.897010183700000	38	0.679071388000000	51
0.889542768000000	39	0.678228438800000	51
0.884361064000000	39	0.671582341400000	51
0.877521423000000	39	0.668055049900000	52
0.875043316200000	39	0.659576027800000	52
0.871162596000000	40	0.659528396000000	52
0.864181478000000	40	0.657903116300000	52
0.857547559200000	40	0.653314610600000	53
0.854213909800000	40	0.651084863700000	53
0.844780772400000	41	0.649253054900000	53
0.842031133000000	41	0.645906689600000	53
0.836102257000000	41	0.641538722000000	54
0.832314248000000	41	0.638916126000000	54
0.825466215000000	42	0.635766802800000	54
0.817203292000000	42	0.632811616000000	54
0.814537714200000	42	0.631255542000000	55
0.813164057400000	42	0.627585200000000	55
0.809584950500000	43	0.623658004100000	55
0.798116773300000	43	0.622809215700000	55
0.797478877000000	43	0.619993755000000	56
0.794391055000000	43	0.618983727700000	56
0.788845261400000	44	0.618241515000000	56
0.786813409000000	44	0.610341406000000	56
0.784394860000000	44	0.608971578500000	57
0.777408464000000	44	0.607070088000000	57
0.773107800900000	45	0.603211483300000	57
0.771239102200000	45	0.599070362000000	57
0.763241083000000	45	0.597671989900000	58
0.756982509000000	45	0.594629428200000	58
0.755139217000000	46	0.592058468900000	58
0.748341458000000	46	0.588733272300000	58
0.743098640200000	46	0.586534355800000	59
0.740429096700000	46	0.585430321500000	59
0.734317394000000	47	0.581703419000000	59
		0.579125040800000	59

0.576978079300000	60	0.478848619000000	72
0.575098296000000	60	0.476793326900000	72
0.572697664400000	60	0.474100201000000	73
0.570868669000000	60	0.472510501000000	73
0.565949551000000	61	0.470530601200000	73
0.561687835500000	61	0.468750612600000	73
0.561362600900000	61	0.467496915500000	74
0.560315827300000	61	0.467129150600000	74
0.558857770100000	62	0.466810484000000	74
0.558090761300000	62	0.463998378700000	74
0.555858886900000	62	0.459670819100000	75
0.551640494700000	62	0.459395286900000	75
0.550583108000000	63	0.457225325500000	75
0.549766385100000	63	0.455708970700000	76
0.549473017500000	63	0.455708970700000	76
0.543262144400000	63	0.454227211400000	76
0.541899174000000	64	0.453652624000000	76
0.540915690600000	64	0.449459422400000	77
0.539626057300000	64	0.448815610900000	77
0.534506744900000	64	0.447647715200000	77
0.532845751200000	65	0.445381526900000	77
0.530199806000000	65	0.441572609000000	78
0.528253832400000	65	0.440416376800000	78
0.525982380100000	65	0.440281747800000	78
0.524911532000000	66	0.439234406000000	78
0.523261585400000	66	0.438309124000000	79
0.521268132600000	66	0.437110364300000	79
0.519726051900000	66	0.436715697000000	79
0.516489668400000	67	0.433849667800000	79
0.516297733100000	67	0.432134127000000	80
0.516004116500000	67	0.431963025000000	80
0.511647002700000	67	0.431646786100000	80
0.509790521400000	68	0.430838757000000	80
0.506660463000000	68	0.427456002000000	81
0.505120412000000	68	0.425869457400000	81
0.504063552500000	68	0.425745174000000	81
0.502120619300000	69	0.423665610900000	81
0.500349240900000	69	0.421601557900000	82
0.498676326500000	69	0.421425391000000	82
0.498387750500000	69	0.417170874200000	82
0.494683880400000	70	0.416694043100000	83
0.494102080400000	70	0.414386920000000	83
0.492915592400000	70	0.411787508000000	84
0.489632180100000	70	0.410957910000000	84
0.488009557600000	71	0.409890367100000	84
0.486452256000000	71	0.408767399000000	84
0.485179461000000	71	0.407035041000000	85
0.482495436000000	71	0.406039920000000	85
0.481095829000000	72	0.404453697000000	85
0.480947754500000	72	0.403198125400000	85

0.402026473000000	86
0.401362925700000	86
0.400934321600000	86
0.399567879000000	86
0.396851453000000	87
0.395151311000000	87
0.392551208000000	88
0.391837876000000	88
0.391752659300000	88
0.390420788000000	88
0.388074355000000	89
0.387534184000000	89
0.387492023000000	89
0.385322757000000	89
0.384188973000000	90
0.382415235000000	90
0.381414969000000	90
0.381053564000000	90
0.380252235000000	91
0.378437079000000	91
0.377734362000000	91
0.377112687000000	91
0.375953502000000	92
0.375627924000000	92
0.374703521000000	92
0.372896276000000	92
0.372049252400000	93
0.370782171000000	93
0.370428350800000	93
0.370203129300000	93
0.366424587100000	94
0.365773542000000	94
0.361345757100000	95
0.359914642500000	96

Appendix B

Calculations for star flux reaching the Apogee CCD in the Acquisition and guiding unit:

- z = zenith angle of the star
- $extinct$ = Extinction factor at Hanle Site
- Air mass can be calculated to a good approximation till 70 degrees zenith using,

$$Airmass = \sec z [1 - 0.0012(\sec^2 z - 1)]$$

- Number of photons in V-band reaching above earth's atmospheres,

$$phot_o = 855264/cm^2/sec$$

- Given the magnitude of the observed object outside the atmosphere, m_0 , magnitude of the observed object at the surface of the earth, m is calculated by

$$m = m_0 + Airmass \times extinct$$

- Incoming photon rate for the object reaching the telescope,

$$phot_{obj} = \frac{phot_o}{10^{m/2.5}} \text{ cm}^{-2}/sec$$

- If the efficiency of telescope optics, mirrors, CCD efficiencies put together if eff , photons reaching and recorded at the CCD are

$$phot_{obj_{CCD}} = eff \times phot_{obj} \text{ cm}^{-2}/sec$$

- For small displacement of the star in the pinhole mirror, the $1k \times 1k$ camera images from HCT are used to calculate fraction of flux reflected off at the pinhole mirror using aperture photometry described in section 6.1.1. For a given seeing if the fraction of flux reflected off is f

$$phot_{obj_{CCD}} = f \times phot_{obj_{CCD}} \text{ cm}^{-2}/sec$$

If the displacement is considerable, that is the measurement of flux enclosed in an aperture equal to the pinhole size starts getting influenced by noise, analytical integration of Moffat profile is used to estimate the flux spilling beyond the pinhole.

- If A is the effective area of the telescope primary and for integration time T sec, and the final flux reaching Apogee CCD is

$$phot_{obj_{CCD}} = A \times T \times phot_{obj_{CCD}} \text{ photons}$$

Bibliography

- [1] <http://www.oharacorp.com/rims1.html>.
- [2] http://www.schott.com/advanced_optics/english/download/schott-optical-glass-pocket-catalog-europe-october-2011-eng.pdf.
- [3] A. Baranne, D. Queloz, M. Mayor, G. Adrianzyk, G. Knispel, D. Kohler, D. Lacroix, J.-P. Meunier, G. Rimbaud, and A. Vin. Elodie: A spectrograph for accurate radial velocity measurements. *Astron. Astrophys. Suppl.*, 119:373–390, October 1996.
- [4] M. Born and E. Wolf. *Principles of Optics*. October 1999.
- [5] J. W. Brault. Rapid-scan high-resolution Fourier spectrometer for the visible. *Journal of the Optical Society of America (1917-1983)*, 66:1081, 1976.
- [6] P. Bristow, F. Kerber, and M. R. Rosa. Advanced 2D spectroscopic predicted data. In *Society of Photo-Optical Instrumentation Engineers (SPIE) Conference Series*, volume 7017 of *Society of Photo-Optical Instrumentation Engineers (SPIE) Conference Series*, page 1, July 2008.
- [7] P. Bristow, F. Kerber, M. R. Rosa, J. F. Pirard, R. Siebenmorgen, and H.-U. Käufl. Model based wavelength calibration for CRIRES. In *Society of Photo-Optical Instrumentation Engineers (SPIE) Conference Series*

- ries, volume 6270 of *Society of Photo-Optical Instrumentation Engineers (SPIE) Conference Series*, page 1, June 2006.
- [8] P. Bristow, F. Kerber, M. R. Rosa, J. Vernet, P. Goldoni, P. Spanò, and A. Modigliani. X-shooter physical model. In *Society of Photo-Optical Instrumentation Engineers (SPIE) Conference Series*, volume 7014 of *Society of Photo-Optical Instrumentation Engineers (SPIE) Conference Series*, page 3, July 2008.
- [9] H. A. Buchdahl. Optical aberration coefficients. II. The tertiary intrinsic coefficients. *Journal of the Optical Society of America (1917-1983)*, 48:563, August 1958.
- [10] H.A. Buchdahl. Optical aberration coefficients. London: Oxford University Press, XX, 336 p. (1954)., 1954.
- [11] H.A. Buchdahl. *Optical aberration coefficients*. Dover Publications, 1968.
- [12] B. Campbell and G. A. H. Walker. Precision radial velocities with an absorption cell. *Pub. Astron. Soc. Pac.*, 91:540–545, August 1979.
- [13] B. Chazelas. Study of Optical Fiber Scrambling to Improve Radial Velocity Measurements: Simulations and Experiments. In *Astronomy of Exoplanets with Precise Radial Velocities*, page 31, August 2010.
- [14] A. Comte. *Cours de philosophie positive*. Number v. 1 in Cours de philosophie positive. Borrani et Droz, 1852.
- [15] F. D. Cruickshank and G. A. Hills. Use of optical aberration coefficients in optical design. *Journal of the Optical Society of America (1917-1983)*, 50:379, April 1960.
- [16] W DeGraffenreid, Sarah C Campbell, and Craig J Sansonetti. Reference lines in the optogalvanic spectra of uranium and thorium in the wavelength range 422 to 462 nm. *JOSA B*, 29(7):1580–1583, 2012.

- [17] W DeGraffenreid and Craig J Sansonetti. Reference lines in the optogalvanic spectra of uranium and thorium over the wavelength range 694–755 nm. *JOSA B*, 19(7):1711–1715, 2002.
- [18] Rolf Engleman Jr, Kenneth H Hinkle, and Lloyd Wallace. The near-infrared spectrum of a th/ar hollow cathode lamp. *Journal of Quantitative Spectroscopy and Radiative Transfer*, 78(1):1–30, 2003.
- [19] R. Griffin and R. Griffin. Accurate wavelengths of stellar and telluric absorption lines near lambda 7000 angstroms. *Mon. Not. Roy. Astron. Soc.*, 162:255, 1973.
- [20] H. Gross. *Handbook of Optical Systems: Aberration theory and correction of optical systems*. Gross/Optical Systems V1-V6 special prices until 6V ST published. Wiley-VCH, 2007.
- [21] George R. Harrison. The production of diffraction gratings: Ii. the design of echelle gratings and spectrographs. *J. Opt. Soc. Am.*, 39(7):522–527, Jul 1949.
- [22] C. Y. Hohenkerk and A. T. Sinclair. Royal Greenwich Observatory Science and Engineering Research Council, 1985.
- [23] T. R. Hunter and L. W. Ramsey. Scrambling properties of optical fibers and the performance of a double scrambler. *Pub. Astron. Soc. Pac.*, 104:1244–1251, December 1992.
- [24] F. Kerber, P. Bristow, and M. R. Rosa. Calibration and modeling support for instruments at ESO. In *Society of Photo-Optical Instrumentation Engineers (SPIE) Conference Series*, volume 7014 of *Society of Photo-Optical Instrumentation Engineers (SPIE) Conference Series*, page 6, July 2008.
- [25] F. Kerber, G. Nave, C. J. Sansonetti, P. Bristow, and M. R. Rosa. The Spectrum of Th-Ar Hollow Cathode Lamps in the 900-4500 nm Region:

- Establishing Wavelength Standards for the Calibration of VLT Spectrographs. In C. Sterken, editor, *The Future of Photometric, Spectrophotometric and Polarimetric Standardization*, volume 364 of *Astronomical Society of the Pacific Conference Series*, page 461, April 2007.
- [26] Florian Kerber, Paul Bristow, and Michael R Rosa. Stis calibration enhancement (stis-ce): Dispersion solutions based on a physical instrument model. In *The 2005 HST Calibration Workshop: Hubble After the Transition to Two-Gyro Mode*, volume 1, page 309, 2006.
- [27] Scott Kirkpatrick, C Daniel Gelatt, Mario P Vecchi, et al. Optimization by simulated annealing. *science*, 220(4598):671–680, 1983.
- [28] C. Lovis and F. Pepe. A new list of thorium and argon spectral lines in the visible. *Astron. Astrophys.*, 468:1115–1121, June 2007.
- [29] C. Lovis, F. Pepe, F. Bouchy, G. Lo Curto, M. Mayor, L. Pasquini, D. Queloz, G. Rupprecht, S. Udry, and S. Zucker. The exoplanet hunter HARPS: unequalled accuracy and perspectives toward 1 cm s^{-1} precision. In *Society of Photo-Optical Instrumentation Engineers (SPIE) Conference Series*, volume 6269 of *Society of Photo-Optical Instrumentation Engineers (SPIE) Conference Series*, page 0, June 2006.
- [30] S. Mahadevan and J. Ge. The Use of Absorption Cells as a Wavelength Reference for Precision Radial Velocity Measurements in the Near-Infrared. *Astrophys. J.*, 692:1590–1596, February 2009.
- [31] G. W. Marcy and R. P. Butler. Planets Orbiting Solar-Type Stars. In *American Astronomical Society Meeting Abstracts*, volume 28 of *Bulletin of the American Astronomical Society*, page 1314, December 1996.
- [32] M. Mayor and D. Queloz. A Jupiter-mass companion to a solar-type star. *Nature*, 378:355–359, November 1995.

- [33] D. Mégevand, F. M. Zerbi, A. Cabral, P. Di Marcantonio, M. Amate, F. Pepe, S. Cristiani, R. Rebolo, N. C. Santos, H. Dekker, M. Abreu, M. Affolter, G. Avila, V. Baldini, P. Bristow, C. Broeg, P. Carvas, R. Cirami, J. Coelho, M. Comari, P. Conconi, I. Coretti, G. Cupani, V. D’Odorico, V. De Caprio, B. Delabre, P. Figueira, M. Fleury, A. Fragoso, L. Genolet, R. Gomes, J. Gonzalez Hernandez, I. Hughes, O. Iwert, F. Kerber, M. Landoni, J. Lima, J.-L. Lizon, C. Lovis, C. Maire, M. Mannelta, C. Martins, A. Moitinho, P. Molaro, M. Monteiro, J. L. Rasilla, M. Riva, S. Santana Tschudi, P. Santin, D. Sosnowska, S. Sousa, P. Spanò, F. Tenegi, G. Toso, E. Vanzella, M. Viel, and M. R. Zapatero Osorio. ESPRESSO: the ultimate rocky exoplanets hunter for the VLT. In *Society of Photo-Optical Instrumentation Engineers (SPIE) Conference Series*, volume 8446 of *Society of Photo-Optical Instrumentation Engineers (SPIE) Conference Series*, page 1, September 2012.
- [34] C. J. Mitchell. Generalized ray-tracing for diffraction gratings of arbitrary form. *Journal of Optics*, 12:301–308, September 1981.
- [35] A Modigliani and MR Rosa. Evaluation of methods to locate emission lines from calibration lamps in 2d spectroscopic data. In *Astronomical Data Analysis Software and Systems (ADASS) XIII*, volume 314, page 808, 2004.
- [36] G Nave, CJ Sansonetti, and U Griesmann. Fourier transform spectroscopy: Methods and applications (1997 osa technical digest series). 1997.
- [37] B. A. Palmer and R. Engleman. *Atlas of the Thorium spectrum*. 1983.
- [38] L. Pasquini, S. Cristiani, R. García López, M. Haehnelt, M. Mayor, J. Liske, A. Manescau, G. Avila, H. Dekker, O. Iwert, B. Delabre, G. Lo Curto, V. D’Odorico, P. Molaro, M. Viel, E. Vanzella, P. Bonifacio, P. Di Marcantonio, P. Santin, M. Comari, R. Cirami, I. Coretti, F. M.

- Zerbi, P. Spanò, M. Riva, R. Rebolo, G. Israelian, A. Herrero, M. R. Zapatero Osorio, F. Tenegi, B. Carswell, G. Becker, S. Udry, F. Pepe, C. Lovis, D. Naef, M. Dessauges, and D. Mégevand. Codex. In *Society of Photo-Optical Instrumentation Engineers (SPIE) Conference Series*, volume 7735 of *Society of Photo-Optical Instrumentation Engineers (SPIE) Conference Series*, page 2, July 2010.
- [39] F. Pepe, M. Mayor, B. Delabre, D. Kohler, D. Lacroix, D. Queloz, S. Udry, W. Benz, J.-L. Bertaux, and J.-P. Sivan. HARPS: a new high-resolution spectrograph for the search of extrasolar planets. In M. Iye and A. F. Moorwood, editors, *Optical and IR Telescope Instrumentation and Detectors*, volume 4008 of *Society of Photo-Optical Instrumentation Engineers (SPIE) Conference Series*, pages 582–592, August 2000.
- [40] G. Raskin, H. van Winckel, H. Hensberge, A. Jorissen, H. Lehmann, C. Waelkens, G. Avila, J.-P. de Cuyper, P. Degroote, R. Dubosson, L. Dumortier, Y. Frémat, U. Laux, B. Michaud, J. Morren, J. Perez Padilla, W. Pessemier, S. Prins, K. Smolders, S. van Eck, and J. Winkler. HERMES: a high-resolution fibre-fed spectrograph for the Mercator telescope. *Astron. Astrophys.*, 526:A69, February 2011.
- [41] Lord Rayleigh. On the dynamical theory of gratings. *Proceedings of the Royal Society of London A: Mathematical, Physical and Engineering Sciences*, 79(532):399–416, 1907.
- [42] Stephen L Redman, Gillian Nave, and Craig J Sansonetti. The spectrum of thorium from 250 nm to 5500 nm: Ritz wavelengths and optimized energy levels. *The Astrophysical Journal Supplement Series*, 211(1):4, 2014.
- [43] M. Rosa. Predictive calibration using instrument models. *Space Telescope European Coordinating Facility Newsletter*, 24:14, March 1997.

- [44] MR Rosa, A Alexov, P Bristow, and F Kerber. Fos post-operational archive and stis calibration enhancement. In *HST Calibration Workshop: Hubble after the Installation of the ACS and the NICMOS Cooling System*, volume 1, page 161, 2003.
- [45] Craig J Sansonetti and KH Weber. Reference lines for dye-laser wave-number calibration in the optogalvanic spectra of uranium and thorium. *JOSA B*, 1(3):361–365, 1984.
- [46] D. J. Schroeder. *Astronomical Optics*. 1987.
- [47] P. K. Seidelmann. *Refraction - Numerical Integration*. University Science Books, Mill Valley, 1992.
- [48] Paolo SpanÅ², Bernard Delabre, Hans Dekker, and Gerardo Avila. New design approaches for a very high resolution spectrograph for the combined focus of the vlt. volume 7014, pages 70140M–70140M–9, 2008.
- [49] Julien FP Spronck, Debra A Fischer, Zachary A Kaplan, Christian Schwab, and Andrew Szymkowiak. Fiber scrambling for high-resolution spectrographs. i. lick observatory. *Publications of the Astronomical Society of the Pacific*, 125(927):511–521, 2013.
- [50] O. Struve. Proposal for a project of high-precision stellar radial velocity work. *The Observatory*, 72:199–200, October 1952.
- [51] F. Wildi, F. Pepe, B. Chazelas, G. Lo Curto, and C. Lovis. A Fabry-Perot calibrator of the HARPS radial velocity spectrograph: performance report. In *Society of Photo-Optical Instrumentation Engineers (SPIE) Conference Series*, volume 7735 of *Society of Photo-Optical Instrumentation Engineers (SPIE) Conference Series*, page 4, July 2010.
- [52] T. Wilken, G. L. Curto, R. A. Probst, T. Steinmetz, A. Manescau, L. Pasquini, J. I. González Hernández, R. Rebolo, T. W. Hänsch,

T. Udem, and R. Holzwarth. A spectrograph for exoplanet observations calibrated at the centimetre-per-second level. *Nature*, 485:611–614, May 2012.